

Advanced gamma-ray spectrometry for environmental radioactivity monitoring

by

Gerti Xhixha

Submitted to

The University of Ferrara

(Faculty of Mathematics, Physics and Natural Sciences)

for the degree of

PhD in Physics

March 2012

Ferrara, Italy: 29, March 2012

Table of content

Chapter 1	22
Introduction to environmental radioactivity: from cosmos to man-made	22
1.1 Cosmic radiation and cosmic-ray produced radionuclides	22
1.2 Primordial radionuclides	24
1.2.1 Potassium, uranium and thorium.....	26
1.2.2 Radioactive decay series	31
1.3 Man-made radionuclides	34
Chapter 2	39
Laboratory γ-ray spectrometry: a fully automated low-background high-resolution γ-ray spectrometer	39
2.1 MCA_Rad system: set-up design and automation	39
2.1.1 Features of HPGe detectors.....	39
2.1.2 Shielding design and evaluation.....	41
2.1.3 Automation: hardware and software developments	45
2.2 MCA_Rad system calibration	47
2.2.1 Energy calibration	47
2.2.2 Efficiency calibration with uncertainty budget	48
2.3 Case of study: bedrock radioelement mapping of Tuscany Region, Italy	60
2.3.1 Representative sampling and sample preparation strategy for bedrock radioelement mapping.....	66
2.3.2 Summary of the results: bedrock radioelement mapping.....	68
2.4 Appendix A: calculation of simplified coincidence summing correction factor for ^{152}Eu	75
Chapter 3	80
In-situ γ-ray spectrometry: an alternative method on calibration and spectrum analysis	80
3.1 In-situ gamma-ray spectrometry using portable NaI(Tl) scintillation detectors	80
3.1.1 ZnNaI system set-up and calibration procedure	80
3.1.2 An alternative approach for calibration and spectrum analysis	85
3.2 Extensive in-situ gamma-ray spectrometry measurements	93

3.2.1 Brief geological settings: Ombrone Valley (Tuscany Region)	93
3.2.2 In-situ measurements: summary of the results	95
3.3 Study of correlation between in-situ and laboratory measurements	98
Chapter 4	105
Airborne γ-ray spectrometry: a geostatistical interpolation method based on geological constrain for radioelement mapping	105
4.1 A self-made airborne gamma-ray spectrometer	105
4.1.1 AGRS system: set-up	105
4.1.2 Calibration and radiometric data processing	107
4.2 The first airborne gamma-ray spectrometry survey in Italy: case of study Elba island	112
4.2.1 Brief geological setting	112
4.2.2 Airborne survey: summary of the results	115
4.3 Radioelement mapping using geostatistical methods	118
Chapter 5	134
Conclusions	134
References	138

List of figures and tables

Chapter 1

Figure 1.1: simplified schematic representation of a hadronic shower originated by a high-energy proton.

Figure 1.2: potassium decay modes.

Figure 1.3: uranium decay chain.

Fig. 1.4: thorium decay chain.

Figure 1.5: secular equilibrium buildup of a very short-lived daughter (^{222}Rn of half-life 3.824 d) from a long-lived parent (^{226}Ra of half-life 1600 y). The activity (arbitrary unit) of the parent remains constant, while the activity of the daughter reaches secular equilibrium (more than 99%) just after seven half-lives.

Figure 1.6: transient equilibrium of the decay of ^{234}U (of half-life 2.45×10^5 y) to ^{230}Th (of half-life 7.54×10^4 y). The activity ratio daughter/parent approaches the constant value 1.48.

Figure 1.7: no equilibrium: the growth and decay of ^{90}Rb (of half-life 158 s) from ^{90}Kr (of half-life 33.33 s). If ^{90}Kr is not continuously produced it will vanish more quickly producing ^{90}Rb which on turn will vanish quickly respective ^{90}Sr having a much longer half-life and reaching secular equilibrium with its daughter ^{90}Y .

Figure 1.8: the global distribution of the locations of all nuclear tests and other detonations worldwide. Atmospheric tests are in blue, underground tests in red. Successively larger symbols indicate yields from 0 to 150 kt, from 150 kt to 1 mt, and over 1 mt. Data taken from: <http://www.johnstonsarchive.net/>.

Figure 1.9: distribution of 440 nuclear power plants operating around the world.

Figure 1.10: European map 1 : 11 250 000 of ^{137}Cs deposition following Chernoby NPP accident. Data taken from: <http://rem.jrc.ec.europa.eu/>.

Table 1.1: confrontation of some models used for the estimation of cosmic radiation dose based on digital terrain model.

Table 1.2: heads of decay chain segments in uranium decay chain and the respective grow-up times.

Table 1.3: heads of decay chain segments in thorium decay chain and the respective grow-up times.

Table 1.4: dose conversion coefficients for external gamma radiation coming from natural radionuclides present in soil.

Table 1.5: principal radionuclides released (volatile elements) in Chernobyl accident compared to those assumed from Fukushima Dai-ichi accident.

Chapter 2

Figure 2.1a: schematic design of the MCA_Rad system. 1) The main lead shielding construction (20 cm x 25 cm x 20 cm). 2) The core copper shielding (10 cm x 15 cm x 10 cm). 3) The rear lead shielding construction. 4) HPGe semiconductor detectors. 5) The mechanical sample changer.

Figure 2.1b: view of MCA_Rad system.

Figure 2.2: the total attenuation coefficients of a standard graded shielding composition showing the migration of X-rays toward low energy range. Data taken from National Institute of Standards and Technologies (NIST) (<http://www.nist.gov>) XCOM 3.1 Photon Cross Sections Database.

Figure 2.3: MCA_Rad system background spectra (live time 100h) without (red) and with (green) shielding showing a reduction of two order of magnitudes.

Figure 2.4: the VEE graphical algorithm which drive the MCA_Rad system.

Figure 2.5: energy calibration function for the MCA_Rad system.

Figure 2.6: standard spectra of ^{152}Eu , ^{56}Co and background normalized for one hour.

Figure 2.7: simplified decay scheme showing the effect of summing in and out.

Figure 2.8: empirical calculation of P/T ratio curve (red) and experimental check by measuring single and double gamma ray emitting points sources like ^{137}Cs , ^{60}Co , ^{40}K and ^{22}Na . The related total efficiency curve (green).

Figure 2.9: absolute efficiency curve for the MCA_Rad system obtained by fitting the corrected values for coincidence summing with **equation 2.16**. Apparent efficiencies of ^{152}Eu (blue triangles) and ^{56}Co (green squares) are also presented.

Figure 2.10: measurement configuration of the experimental measurement done for the calculation of geometrical correction factor.

Figure 2.11: curve reconstructing the geometrical correction factor obtained by fitting photopeaks of ^{56}Co and ^{57}Co with a third order polynomial (**Eq. 2.19**).

Figure 2.12: average mass attenuation coefficient deduced from weighting different rock forming minerals (calcite (CaCO_3); quartz (SiO_2); dolomite ($\text{CaMg}(\text{CO}_3)_2$); feldspar albite ($\text{NaAlSi}_3\text{O}_8$); feldspar anorthite ($\text{CaAl}_2\text{Si}_2\text{O}_8$); feldspar orthoclase (KAlSi_3O_8); anhydrite (CaSO_4); gypsum ($\text{CaSO}_4 \cdot 2\text{H}_2\text{O}$); muscovite ($\text{KAl}_2(\text{Si}_3\text{O}_{10}(\text{OH},\text{F})_2$); rutile (TiO_2); bauxite gibbsite ($\text{Al}(\text{OH})_3$).

Figure 2.13: the geological map of Tuscany at scale 1:250,000.

Figure 2.14: (a) aligned homogeneous grid, (b) unaligned homogeneous grid, and (c) random sampling strategies.

Figure 2.15: the spatial distribution of 882 samples (blue triangle soil and red circle rocks samples) collected over the territory of Tuscany Region for the realization of potential natural radioactivity concentration of bedrocks.

Figure 2.16: the potential annual effective dose equivalent weighted for the Tuscany Region area and calculated based on the characterisation of geological formational domains.

Figure 2.17: distribution of total activity (Bq/kg) in principal geological formations characterized with more than 10 samples. The box plot encloses 50% of the values while the whiskers include other 45% of them. The data exceeding this limits are the outliers and extremes.

Figure 2.18: the distribution of potassium, uranium, thorium and the relative total activity concentration for 882 sample.

Figure 2.19: the potential total activity concentration of bedrocks in Tuscany Region realized through the utilization of 882 sample.

Figure A-1: simplified decay scheme for ^{152}Eu for gamma energies.

Table 2.1: the features of the two detectors used in the project design of MCA_Rad system.

Table 2.2: characterization of MCA_Rad system background (Bckg. without shielding and Bckg. with shielding) expressed in count per hour (cph) for the most intense energetic lines and the corresponding detection limit LD in counts (**Eq. 2.1**) for 95% confidence interval (CI) and minimum detectable activity (MDA) in Bq/kg (**Eq. 2.2**).

Table 2.3: apparent efficiency and corrected efficiencies for coincidence summing according to **equation 2.15**.

Table 2.4: activity concentrations calculated for the main energetic lines used to study the ^{238}U and ^{232}Th decay chains and for ^{40}K and the respective statistical uncertainty. An evaluation of efficiency calibration method uncertainty budgeted is described in details below.

Table 2.5: uncertainty budgeted evaluation for efficiency calibration method.

Table 2.6: typical statistical uncertainty for activity concentration ranges for 1h of acquisition time. The evaluation was done for 609 keV (^{214}Bi), 583 keV (^{208}Tl) considering secular equilibrium and 1460 keV (^{40}K).

Table 2.7: radioactivity characterization for 42 geological formation domains by MCA_Rad system for 1h acquisition time (1σ is the standard deviation) with (*) is reported the median value.

Table A-1: tables of coincidence summing coefficients calculated and compared with bibliographic values.

Chapter 3

Figure 3.1: configuration of ZnNaI_1.0L system set-up in a backpack.

Figure 3.2: worldwide calibration facilities (pad): data source **IAEA 2010**.

Figure 3.3: example of a natural calibration site (GC1 see table 3.3).

Figure 3.4: spectra acquired in-situ (black dashed line) compared with the fit (full red line) obtained by the FSA with NNLS constrain (described later). The ^{137}Cs contribution is shown alone (green dotted line) to underline the need to include this element in the analysis.

Figure 3.5: the spectra acquired in CA1 site in (red full line). The fit obtained using the concentrations measured with the MCA_Rad system is also reported (black dashed line).

Figure 3.6: the sensitive spectra of ^{137}Cs , obtained using the standard FSA method. The green line is placed to show the zero count level.

Figure 3.7: the sensitive spectra of ^{238}U , obtained using the standard FSA method. The region where there are negative counts is emphasized in the box.

Figure 3.8: the sensitive spectra obtained through the FSA method with NNLS constrain.

Figure 3.9: the geological map 1:50,000 of Ombrone basin showing the distribution of in-situ gamma-ray spectrometry measurement points. The detailed legend is available from data source: <http://www.geotecnologie.unisi.it/>.

Figure 3.10: the digital terrain model of position of Ombrone basin and the 80 sites investigated in the area.

Figure 3.11: the distributions specific activity concentration and external gamma absorbed dose rates for 80 in-situ measurements.

Figure 3.12: the tripod (static) and human back (dynamic) modalities of in-situ measurements.

Figure 3.13: the absorbed dose in detector due to ^{137}Cs in the 80 sites, determined with the new FSA with NNLS constrain (red circles) and with the standard FSA method (black triangles). The new algorithm avoids the negative counting and it reduces at the same time the uncertainties.

Figure 3.14: the potassium concentration measured with MCA_Rad system (HPGe) and with ZnNaI system (using FSA with NNLS method) are plotted together. The average of five soil samples with relative uncertainty is plotted for the MCA_Rad analysis. No errors are associated with the ZnNaI data. The linear correlation line associated with the Ω value is shown (full line) with 1σ error (dashed line).

Figure 3.15: the uranium concentration measured with MCA_Rad system (HPGe) and with ZnNaI system (using FSA with NNLS method) are plotted together. The average of five soil samples with relative uncertainty is plotted for the MCA_Rad analysis. No errors are associated with the ZnNaI data. The linear correlation line associated with the Ω value is shown (full line) with 1σ error (dashed line).

Figure 3.16: the thorium concentration measured with MCA_Rad system (HPGe) and with ZnNaI system (using FSA with NNLS method) are plotted together. The average of five soil samples with relative uncertainty is plotted for the MCA_Rad analysis. No errors are associated with the ZnNaI data. The linear correlation line associated with the Ω value is shown (full line) with 1σ error (dashed line).

Table 3.1: typical concentrations of constructed pads used to calibrate in-situ gamma-ray spectrometers (IAEA 1990).

Table 3.2: half-thickness ($\Delta x = \log(2) / \mu_t$, where μ_t (m^{-1}) is the linear mass attenuation coefficient) of the most intense gamma-energies of in-situ measurement importance.

Table 3.3: the average of the distribution of natural radioisotopes concentration. The errors correspond to one standard deviation.

Table 3.4: typical energy windows used to estimate the activity concentration for in-situ measurements (IAEA 2003).

Table 3.5: example of sensitivity matrix calculated for 7.64 cm x 7.64 cm NaI(Tl) detector using standard calibration pads.

Table 3.6: example of sensitivity matrix calculated for 7.64 cm x 7.64 cm NaI(Tl) detector using natural calibration pads.

Table 3.7: the correction factors applied to in-situ measurement at different measurement geometries (1m height tripod and holding on back bag at about 1m height).

Table 3.8: the Ω coefficients averaged for all the data samples. For the WAM results the χ^2 is not shown due to absence of a fitting procedure.

Chapter 4

Figure 4.1: schematic design of AGRS_16.0L composed by four scintillation NaI(Tl) detectors of dimensions 10 cm x 10 cm x 40 cm each and one scintillation NaI(Tl) detectors of dimension 10 cm x 10 cm x 10 cm.

Figure 4.2: final configuration of AGRS_16.0L system.

Figure 4.3: schematic design of hardware/software and output for AGRS_16.0L system.

Figure 4.4: example of a natural calibration site (GC1 see table 3.3).

Figure 4.5: Sensitivity spectra obtained using FSA with NNLS constrain method for the AGRS_16.0L system.: potassium sensitivity spectra (up-left), uranium sensitivity spectra (up-right), thorium sensitivity spectra (down-left) and cesium sensitivity spectra (down-right).

Figure 4.6: geological map of Elba Island (taken from the new Geological Map of Tuscany region realized at 1:10,000 scale, see CGT, 2011): the western sector is mainly characterized by intrusive igneous rocks (magenta), the central and eastern

parts of the island are characterized by a wide lithological variation (green, purple and pink), while the southeastern outcrop almost exclusively consists of metamorphic rocks (Mt. Calamita). For the official legend of all the geological formations see <http://www.geologiatoscana.unisi.it>. Coordinate system is UTM WGS84 Zone 32 North.

Figure 4.7: Elba tectonic vertical sketch from western to eastern coastline. This scheme shows TC structural pile, and toponyms are roughly located in the corresponding tectonics units where they lay: PU - Porto Azzurro Unit, UO - Ortano Unit, AU - Acquadolce Unit, MU - Monticiano-Roccastrada Unit, TN - Tuscan Nappe, GU - Grassera Unit, OU - Ophiolitic Unit, EU - Palaeogene Flysch Unit, CU - Cretaceous Flysch Unit. Modified from **Bortolotti et al. (2001)**.

Figure 4.8: a) altitude profile recorded during flight, b) potassium abundances profile, c) uranium abundance profile and d) thorium abundance profile.

Figure 4.9: correlation matrix for group PPP variables: the lower panel shows the joint frequencies diagrams for each couple of variables and the robust locally weighted regression (**Cleveland, 1979**); cells on the matrix diagonal show the univariate distributions; the upper panel shows both correlation coefficient value for each bivariate distribution (blue low linear correlation, green small correlation, red high correlation), and the statistical significance testing scores for each correlation test.

Figure 4.10: omnidirectional linear coregionalization model for K (%) abundance and parametric geology: experimental semi-variograms (diagonal of the matrix) and cross semivariograms (lower left corner); variograms and cross-variograms model with same geostatistical range; numerical and graphical (histogram) indications of the number of pairs participating in the semi-variance calculation for each lag distance (green dots with labels); distance between two consecutive airborne gamma-ray measurements along one route (vertical dashed and dotted blue line).

Figure 4.11: estimation map of K (%) abundance and normalized estimation errors.

Figure 4.12: estimation map of equivalent uranium (eU) abundance in ppm and normalized estimation errors.

Figure 4.13: estimation map of equivalent thorium (eTh) abundance in ppm and normalized estimation errors.

Figure 4.14: a) frequency distributions of kriged maps of K abundances estimated by CCoK through three different reclassification of geological map of Elba Island; b) frequency distributions of Normalized Standard Deviations maps (the accuracy of CCoK estimations).

Figure 4.15: a) frequency distributions of differences between pairs of kriged maps of K abundances estimated by CCoK through three different reclassification of geological map of Elba Island; b) frequency distributions of differences between pairs of Normalized Standard Deviations maps.

Table 4.1: uncertainty sources associated to radiometric data measured using AGRS_16.0L system.

Table 4.2: experimental uncertainties for the measured radioelement concentrations.

Table 4.3: descriptive statistical parameters of airborne radiometric values.

Table 4.4: parameters of ESVs and X-ESVs, omnidirectional linear coregionalization models (parametric geology has not measure units), and cross-validation results of primary variables (expressed through the mean of standardized errors (MSE) and the variance of standardized errors (VSE)) for all groups of variables.

Table 4.5: Descriptive statistics of estimation maps of K abundances (CCoK estimation) and the respective estimation errors (NSD), and their map differences. Column G (± 0.1): percentage of two maps' pixels that differ each other less than $\pm 0.1\%$ of K abundance. Column H (± 1 & 2σ): percentage of two maps' pixels that differ each other between 1 and 2 standard deviation from the mean of the difference map, which is close to 1% of K abundance.

Abstract

I programmi di monitoraggio della radioattività ambientale iniziano nei tardi anni '50 del XX secolo a seguito della fallout radioattiva dai test delle armi nucleari nell'atmosfera che destano preoccupazione per gli effetti sulla salute. Successivamente, l'industrializzazione mondiale delle nuove fonti energetiche ha portato allo sviluppo di piani nazionali sulla produzione di elettricità sfruttando la tecnologia nucleare, e ha dato origine in questo contesto al sondaggio e all'estrazione mondiale dei minerali combustibili: il sondaggio dell'uranio ha ricevuto particolare attenzione nei tardi anni '40 in USA, Canada, nell'ex Unione Sovietica e anche in Australia nel 1951, secondo i rispettivi piani nazionali. Oggi ci sono circa 440 centrali nucleari per la generazione dell'energia con circa 70 ulteriori NPP in costruzione, che necessitano di programmi per la sicurezza e l'emergenza nucleare in un grande numero di Stati. Si pensi alla banca dati Radioactivity Environmental Monitoring (REM) e la European Radiological Data Exchange Platform (EURDEP). Inoltre molte applicazioni nell'ambito delle geoscienze sono legate alla misurazione della radioattività ambientale che vanno dalla mappatura geologica, all'esplorazione mineraria, alla costruzione di database geo chimici e a studi sul calore terrestre.

La spettroscopia gamma è una tecnica molto usata nell'ambito dei programmi sulla radioattività naturale. Lo scopo di questo lavoro è quello di investigare le potenzialità che tale tecnica può offrire nel monitoraggio della concentrazione della radioattività attraverso tre diversi interventi che hanno a che fare con misurazioni in laboratorio, in situ e airborne. Un metodo avanzato per l'utilizzo della spettroscopia gamma è realizzato migliorando le performance degli strumenti e realizzando e testando strumentazione specifica capace di risolvere problemi pratici che si presentano nel monitorare la radioattività. Per ognuno di questi metodi di spettroscopia gamma si affrontano anche i problemi di calibrazione, progettazione di piani di monitoraggio, analisi e processamento dati.

Nel primo capitolo si dà una descrizione generale dei radionuclidi comuni presenti nell'ambiente e che sono rilevanti per i programmi di monitoraggio. Vengono trattate tre categorie di radionuclidi ambientali classificati secondo la loro origine in cosmogenici, primordiali e antropogenici. I raggi cosmici producono continuamente radionuclidi, così come radiazione diretta, costituita principalmente da muoni ad alte energie. Radionuclidi cosmogenici sono originati dall'interazione di raggi cosmici con nuclei stabili presenti nell'atmosfera terrestre. Radionuclidi primordiali sono associati col fenomeno della nucleosintesi delle stelle e sono presenti nella crosta terrestre. Radionuclidi antropogenici presenti comunemente in ambiente naturale sono principalmente derivati dalla ricaduta radioattiva dei test di armamenti nucleari condotti nell'atmosfera e da applicazioni di tecnologie

nucleari, come le centrali nucleari per la generazione di energia e le attività legate al ciclo di combustibili nucleari. Un contributo rilevante, generalmente con implicazioni locali, viene dalle cosiddette “industrie non nuclear”, che sono responsabili dell’eccitamento di elementi radioattivi naturali che producono numerosi materiali naturali radioattivi (NORM/TENORM).

Nel secondo capitolo viene descritto un metodo per la soluzione del problema che nasce nel monitoraggio di situazioni in cui un alto numero di campioni deve essere misurato con rivelatori HPGe. In questi casi, i costi per la manodopera impiegata diventano rilevanti per il budget di laboratorio e talvolta ne limitano le capacità. ORTEC® e CANBERRA, ad esempio, producono spettrometri gamma supportati da ricambi automatici dei campioni che possono processare decine di campioni senza lacuna presenza umana. Tuttavia, un certo numero di miglioramenti può essere effettuato su tali sistemi, sia nel design di schermatura sia nell’efficienza di rivelazione.

Abbiamo sviluppato un sistema automatico di spettroscopia gamma usando due rivelatori HPGe che rappresenta una metodologia per implementare l’efficienza di rivelazione. Abbiamo scelto un approccio alternativo al design della schermatura e al sistema automatico di ricambio. L’uso dei due rivelatori HPGe permette di raggiungere una buona precisione statistica in poco tempo, il che contribuisce a ridurre drasticamente i costi e la manodopera impiegata. Una descrizione dettagliata della caratterizzazione dell’efficienza del picco energetico di tale strumento è trattato in questo capitolo. Infine, il sistema di spettroscopia gamma chiamato MCA_Rad è stato usato per caratterizzare la concentrazione di radioattività naturale dei suoli della regione Toscana. Più di 800 campioni sono stati misurati e sono qui associati con le mappe dei suoli e relative concentrazioni potenziali di radioattività nella regione Toscana.

Nel terzo capitolo è descritta l’applicazione degli spettrometri gamma portatili a scintillazione per programmi di monitoraggio in situ. Vengono affrontati i problemi di calibrazione e il metodo di analisi spettrale. La spettrometria gamma in situ con scintillatori a ioduro di sodio è un metodo sviluppato e consolidato per gli studi della radioattività. Generalmente, una serie di “pad” auto-costruite, calibrate, e prevalentemente arricchite con uno dei radioelementi sono state utilizzate per calibrare questo strumento portatile. Questo metodo è stato ulteriormente sviluppato, introducendo lo stripping, ovvero la window analysis descritta nelle linee guida IAEA come il metodo standard per l’esplorazione e la mappatura dei radioelementi naturali.

Abbiamo realizzato uno strumento portatile usando spettrometri gamma a scintillazione con un rivelatore a ioduro di sodio. Un metodo di calibrazione alternativa è stato usato invece per siti naturali

ben caratterizzati che mostrano una concentrazione prevalente di uno dei radioelementi. Questa procedura supportata da ulteriori sviluppi del metodo FSA (Full Spectrum Analysis) implementato con il metodo NNLS è stato applicato per la prima volta nella calibrazione e nell'analisi spettrale. Questo nuovo approccio permette di evitare artifici e risultati non fisici nell'analisi FSA in relazione al processo di minimizzazione di χ^2 . Ciò ha permesso di ridurre l'incertezza statistica diminuendo tempi e costi e permettendo di analizzare più radioisotopi, anche quelli non naturali. Infatti, come esempio delle potenzialità di questo metodo isotopi di ^{137}Cs sono stati analizzati. Infine, questo metodo è stato utilizzato acquisendo spettri gamma dall'Ombrone usando un rivelatore a ioduro di sodio (10.16 cm×10.16 cm) in 80 siti diversi del bacino toscano. I risultati del metodo FSA con NNLS sono stati comparati con le misurazioni di laboratorio usando i rivelatori HPGe sui campioni di suolo acquisiti.

Nel quarto capitolo è discussa l'autocostruzione di uno spettrometro gamma airborne, AGRS_16.0L. il metodo AGRS è largamente considerato come uno strumento essenziale per la mappatura della radioattività naturale sia per gli studi geoscientifici che per la risposta d'emergenza radioattiva su siti potenzialmente contaminati. Infatti, tecniche di AGRS sono state utilizzate in molti Paesi già dalla seconda metà del XX secolo, come in USA, Canada, Australia, Russia, Repubblica Ceca e Svizzera.

Abbiamo applicato il metodo di calibrazione nel capitolo precedente usando siti naturali ben caratterizzati e implementati per la prima volta nell'analisi dati radiometrica FSA con limiti NNLS. Questo metodo permette di diminuire l'incertezza statistica e di ridurre conseguentemente al minimo il tempo di acquisizione dati (che dipende anche dal sistema AGRS e dai parametri di volo), aumentando in questo modo la risoluzione spaziale. Infine, l'AGRS_16.0L è stato usato per la mappatura in volo dei radioelementi sull'isola d'Elba. E' ben noto che la radioattività naturale è strettamente connessa alla struttura geologica delle rocce e questa informazione è stata tenuta presente per l'analisi e la costruzione delle mappe. Un'approccio multivariat o all'analisi è stato considerato per l'interpolazione geostatistica dei dati radiometrici, che sono stati messi in relazione con la geologia attraverso l'interpolatore Collocated Cokriging (CCoK). Infine, sono state costruite le mappe dell'Isola d'Elba per le concentrazioni dei radioelementi potenziali di potassio, uranio e torio.

Keywords

Spettrometria gamma; Monitoraggio della radioattività ambientale; Calibrazione in efficienza di spettrometri gamma; Rivelatori a semiconduttore HPGe; Rivelatori a scintillatore NaI(Tl); Spettrometria gamma in-situ; Spettrometria gamma airborne; Full spectrum analysis; Mappe di distribuzione di U, Th e K; Monitoraggio di ^{137}Cs

Abstract

The environmental radioactivity monitoring programs start in the late 1950s of the 20th century following the global fallout from testing of nuclear weapons in the atmosphere, becoming a cause of concern regarding health effects. Later, the necessity of world industrialization for new energy sources led to develop national plans on electricity production from nuclear technology, initializing in this context world wide exploration for fuel minerals: uranium exploration gained a particular attention in late 1940's in USA, Canada and former USSR and in 1951 in Australia with respective national plans. Nowadays there are about 440 nuclear power plants for electricity generation with about 70 more NPP under construction giving rise to the nuclear emergency preparedness of a large number of states (like Radioactivity Environmental Monitoring (REM) data bank and European Radiological Data Exchange Platform (EURDEP). Furthermore, a lot of applications in the field of geosciences are related to the environmental radioactivity measurements going from geological mapping, mineral exploration, geochemical database construction to heat -flow studies.

Gamma-ray spectroscopy technique is widely used when dealing with environmental radioactivity monitoring programs. The purpose of this work is to investigate the potentialities that such a technique offers in monitoring radioactivity concentration through three different interventions in laboratory, in-situ and airborne measurements. An advanced handling of gamma-ray spectrometry method is realized by improving the performances of instruments and realizing and testing dedicated equipments able to deal with practical problems of radioactivity monitoring. For each of these gamma-ray spectrometry methods are faced also the problems of calibration, designing of monitoring plans and data analyzing and processing.

In the first chapter I give a general description for the common radionuclides present in the environment having a particular interest for monitoring programs. Three categories of environmental radionuclides classified according to their origin as cosmogenic, primordial and man-made are discussed. The cosmic rays continuously produce radionuclides and also direct radiation, principally high energetic muons. Cosmogenic radionuclides are originated from the interaction of cosmic rays with stable nuclides present in the Earth's atmosphere. Primordial radionuclides are associated with the phenomenon of nucleosynthesis of the stars and are present in the Earth's crust. Man-made radionuclides commonly present in natural environments are principally derived from radioactive fallout from atmospheric nuclear weapons testing and peaceful applications of nuclear technology like nuclear power plants for electricity generation and the associated nuclear fuel cycle facilities. A relevant contribution, generally with local implication comes from the so called non-nuclear industries

which are responsible for technological enhancement of natural radioelements producing huge amounts of naturally occurring radioactive materials (NORM/TENORM).

In the second chapter is described a homemade approach to the solution of the problem rising in monitoring situations in which a high number of samples is to be measured through gamma-ray spectrometry with HPGe detectors. Indeed, in such cases the costs sustaining the manpower involved in such programs becomes relevant to the laboratory budget and sometimes becomes a limitation of their capacities. Manufacturers like ORTEC[®] and CANBERRA produce gamma-ray spectrometers supported by special automatic sample changers which can process some tens of samples without any human attendance. However, more improvements can be done to such systems in shielding design and detection efficiency.

We developed a fully automated gamma-ray spectrometer system using two coupled HPGe detectors, which is a well known method used to increase the detection efficiency. An alternative approach on shielding design and sample changer automation was realized. The utilization of two coupled HPGe detectors permits to achieve good statistical accuracies in shorter time, which contributes in drastically reducing costs and man power involved. A detailed description of the characterization of absolute full-energy peak efficiency of such instrument is reported here. Finally, the gamma-ray spectrometry system, called MCA_Rad, was used to characterize the natural radioactivity concentration of bed-rocks in Tuscany Region, Italy. More than 800 samples are measured and reported here together with the potential radioactivity concentration map of bed rocks in Tuscany Region.

In the third chapter is described the application of portable scintillation gamma -ray spectrometers for in-situ monitoring programs focusing on the problems of calibration and spectrum analysis method. In-situ γ -ray spectrometry with sodium iodide scintillators is a well developed and consolidated method for radioactive survey. Conventionally, a series of self-constructed calibration pads prevalently enriched with one of the radioelements is used to calibrate this portable instrument. This method was further developed by introducing the stripping (or window analysis) described in International Atomic Energy Agency (IAEA) guidelines as a standard methods for natural radioelement exploration and mapping.

We realized a portable instrument using scintillation gamma-ray spectrometers with sodium iodide detector. An alternative calibration method using instead well-characterized natural sites, which show a prevalent concentration of one of the radioelements, is developed. This procedure supported by further development of the full spectrum analysis (FSA) method implemented in the non-negative

least square (NNLS) constrain was applied for the first time in the calibration and in the spectrum analysis. This new approach permits to avoid artifacts and non physical results in the FSA analysis related with the χ^2 minimization process. It also reduces the statistical uncertainty, by minimizing time and costs, and allows to easily analyze more radioisotopes other than the natural ones. Indeed, as an example of the potentialities of such a method ^{137}Cs isotopes has been implemented in the analysis. Finally, this method has been tested by acquiring gamma Ombrone -ray spectra using a 10.16 cm×10.16 cm sodium iodide detector in 80 different sites in the basin, in Tuscany. The results from the FSA method with NNLS constrain have been compared with the laboratory measurements by using HPGe detectors on soil samples collected.

In the forth chapter is discussed the self-construction of an airborne gamma-ray spectrometer, AGRS_16.0L. Airborne gamma-ray spectrometry (AGRS) method is widely considered as an important tool for mapping environmental radioactivity both for geosciences studies and for purposes of radiological emergency response in potentially contaminated sites. Indeed, they have been used in several countries since the second half of the twentieth century, like USA and Canada, Australia, Russia, Checzech Republic, and Switzerland.

We applied the calibration method described in the previous chapter using well -characterized natural sites and implemented for the first time in radiometric data analysis FSA analysis method with NNLS constrain. This method permits to decrease the statistical uncertainty and consequently reduce the minimum acquisition time (which depend also on AGRS system and on the flight parameters), by increasing in this way the spatial resolution. Finally, the AGRS_16.0L was used for radioelement mapping survey over Elba Island. It is well known that the natural radioactivity is strictly connected to the geological structure of the bedrocks and this information has been taken into account for the analysis and maps construction. A multivariate analysis approach was considered in the geostatistical interpolation of radiometric data, by putting them in relation with the geology through the Collocated Cokriging (CCoK) interpolator. Finally, the potential radioelement maps of potassium, uranium and thorium are constructed for Elba Island.

Keywords

Gamma-ray spectrometry; Environmental radioactivity monitoring; Gamma-ray spectrometry efficiency calibration; Semiconductor HPGe detector; Scintillation NaI(Tl) detector; In-situ gamma-ray spectrometry; Airborne gamma-ray spectrometry; Full spectrum analysis; Radiometric map of eU, eTh and K; ^{137}Cs monitoring

Acknowledgements

I would like to thank a number of people who have helped and encouraged during my period of PhD research at the University of Ferrara. Firstly, I would like to express my personal gratitude to my supervisors, Prof. Giovanni Fiorentini and PhD. Fabio Mantovani, which provided the support and opportunities to enable my personal experiences regarding gamma-ray spectrometry technique. I would also like to thank Prof. Carlos Rossi Alvarez, Prof. Luigi Carmignani, Gian Paolo Buso, Gian Piero Bezzon, Carlo Brogginini and Roberto Menegazzo for continuous support and critical assessments.

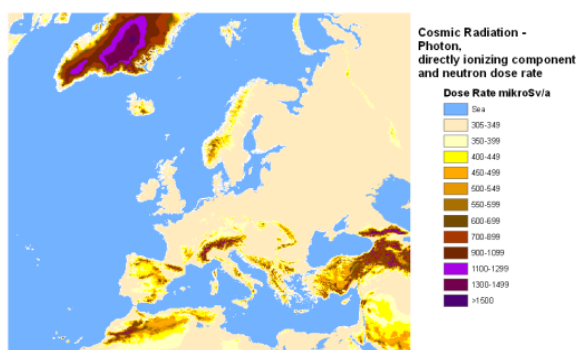
I would like to thank Prof. Bejo Duka who trusted my scientific capabilities and for the encouragement and support given to me during my studies at University of Tirana, Faculty of Natural Sciences. I would like also to thank Prof. Vath Tabaku, Prof. Spiro Grazhdani and Prof. Pandeli Marku for their support as researcher at Agricultural University of Tirana, Faculty of Forestry Science.

I would like to thank all friends and colleagues with which I worked, and especially Antonio Caciolli, Liliana Mou, Manjola Shyti, Silvia De Bianchi, Merita Kaçeli Xhixha, Tommaso Colonna, Ivan Callegari, Giovanni Massa, Enrico Guastaldi, Mauro Antongiovanni for their trust, support and encouragement.

Finally a special thank goes to my parents, Gëzim and Tatjana and to my wife and son, Merita and Leonel for supporting and believing me.

Chapter 1

Introduction to environmental radioactivity: from cosmos to man-made



Estimated cosmic radiation dose map. Data taken from <http://ec.europa.eu/dgs/jrc/index.cfm> including ionization and neutron components.

- 1.1 **Cosmic radiation and cosmic-ray produced radionuclides**
- 1.2 **Primordial radionuclides**
 - 1.2.1 *Potassium, uranium and thorium*
 - 1.2.2 *Radioactive decay series: secular equilibrium*
- 1.3 **Man-made radionuclides**

Chapter 1

Introduction to environmental radioactivity: from cosmos to man-made

1.1 Cosmic radiation and cosmic-ray produced radionuclides

Cosmic radiation was introduced at the environmental radiation budget by [Hess 1912a](#) and [1912b](#) which discovered it during balloon flights, where in an unexpected way he observed that the radiation intensity increases with increasing the distance from the source (the earth's surface constituted by rock and soil containing radionuclides). He explained this experiment introducing a radiation penetrating earth's atmosphere and originating from outside the earth called **cosmic radiation**.

The primary sources of cosmic radiation are the galaxies in outer space (galactic cosmic radiation) and secondary source is the Sun in our solar system (significant during maximum sun cycle activity). The galactic cosmic radiation coming at the upper atmosphere, is made up of about 98% baryons and 2% electrons ([Reitz 1993](#)). It consists mainly of protons (87% of the baryons) and to a lesser extent of helium ions (11%) and heavier ions (ranging from carbon to iron; 1%), with energies ranging from 10^2 MeV to more than 10^{14} MeV.

In fact, the result of the cosmic radiation is a continuous bombardment of Earth's magnetosphere by a nearly isotropic flux of charged particles having different energies. However, only a part of the cosmic radiation actually reaches the surface of the Earth. Furthermore, charged particles are deflected from the Earth's magnetic field component that is perpendicular to the direction of particle motion. This means that the cosmic radiation is deflected more at the equator than near the poles producing a

geomagnetic latitude effect for cosmic radiation. The absorbed dose rate is about 10% lower at the geomagnetic equator than at high latitudes. Primary cosmic radiation intensity remains fairly constant between 15°N and 15°S, while increases rapidly to approximately 50°N and 50°S, after which it remains essentially constant against to the poles.

As mentioned above, the interaction of high-energy particles with atoms and molecules in the atmosphere (mainly nitrogen and oxygen), are the dominant mechanism of interaction resulting in a cascade of interactions and reaction products like secondary protons, neutrons and charged/uncharged pions (Bartlett 2004) together with lower Z nuclei like ^3H , ^{14}C , $^7\text{Be}/^{10}\text{Be}$ etc. called also **cosmogenic radionuclides**. This radioisotopes are beta pure with exception of ^7Be which emits a characteristic gamma-ray of 477.6 keV with and intensity of 10.5 %, extensively studied as a tracer for atmospheric circulation phenomena and for it's diurnal variation. However, only ^3H and ^{14}C really contribute to any significant exposures to the worldwide population. The secondary protons and neutrons generate more nucleons initializing the so called hadronic shower (Fig. 1.1).

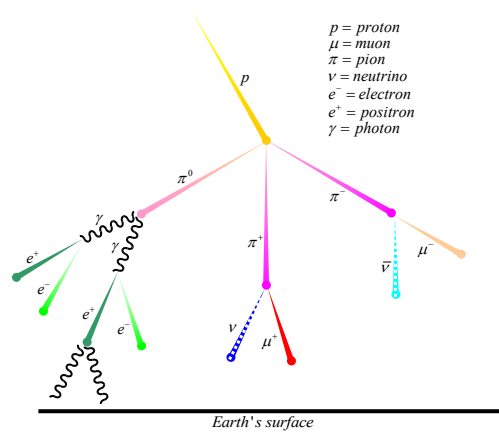


Figure 1.1: simplified schematic representation of a hadronic shower originated by a high-energy proton.

The neutral pions decay into high-energy photons, which produce electron–positron pairs leading to the production of annihilation photons hence pair production and so on. The decay of the charged pions generates the muon cascade.

$$\pi^+ \rightarrow \bar{\mu}^+ + \nu_{\mu} \text{ producing anti-muon and a muon-neutrino}$$

$$\pi^- \rightarrow \mu^+ + \bar{\nu}_{\mu} \text{ producing a muon and a muon-anti-neutrino}$$

The creation of these secondary particles is in competition with attenuation by atmosphere where the shielding effect is determined by the atmospheric depth, that is, the mass thickness of the air above

(about 12 km of water equivalent thickness). This altitude effect shows a doubling of the exposure due to cosmic radiation at about 1.5 – 2 km height relative to the sea level ([UNSCEAR 2000](#); [Paschoa and Steinhudler 2010](#)). The main source of ground exposure at sea level is due to muons, because of their long mean free path (with typical energy range from 1 to 20 GeV) contributing about 80% of the absorbed dose rate in free air from the directly ionizing radiation (the remainder results from electrons).

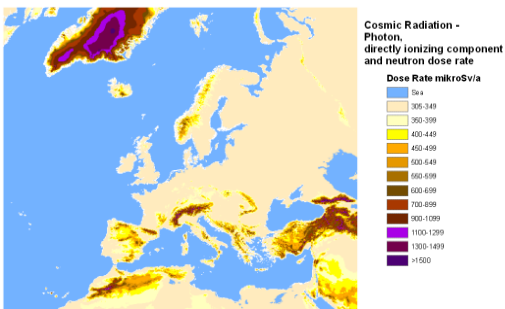
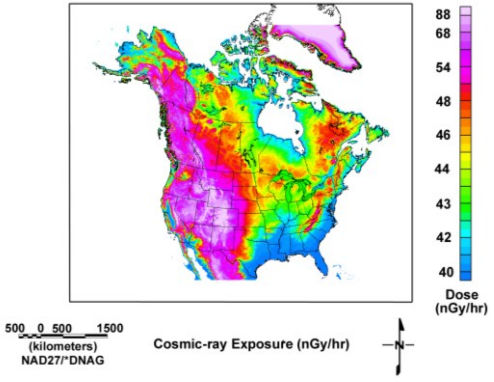
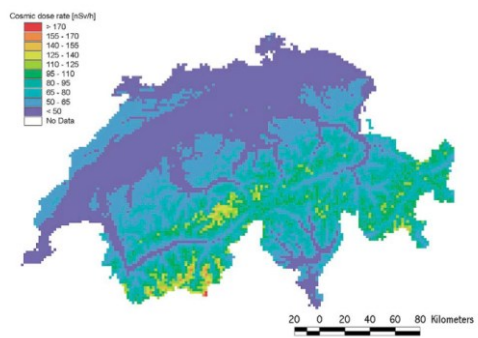
The spatial variation of the exposure due to cosmic radiation can be synthesized with the following factors: latitude; altitude; emission of radiation by terrestrial natural radionuclides; and cloud coverage of the skies. However, models can be used to estimate the cosmic radiation dose within a certain degree of uncertainty based on digital terrain model (for calculating altitude effect) and on latitude effect and taking into consideration the ionization and neutron component ([Table 1.1](#)).

1.2 Primordial radionuclides

Primordial radionuclide called also terrestrial radionuclides found in nature are related primarily to the fact that these isotopes themselves have very long half-lives or are created in decay chains with the head parents having very long half-life. The principal sources of environmental radioactivity monitoring interest are due to the presence of ^{238}U , ^{232}Th and ^{40}K in the Earth's crust. Generally other major trace elements like ^{235}U and ^{87}Rb are negligible for radioactivity monitoring purposes. The world average abundances of the continental upper crust for ^{238}U , ^{232}Th and ^{40}K are respectively 2.7 ppm¹, 10.5 ppm and 2.3% ([Rudnick and Gao 2003](#)). Many countries have already monitored the distribution of natural radioactivity finalized with the construction of the radiometric maps of their territory (USA, Canada, Australia, Switzerland, Slovakia, Slovenia, Czech Republic, UK etc). The nuclides of the ^{238}U , and ^{232}Th radioactive decay series and ^{40}K are shown in [Figure 1.2 - 1.4](#) with their half-lives and branching ratios.

¹ Conversion of radioelement concentration to specific activity ([IAEA 2003](#)) for 1% K = 313 Bq/kg; 1 ppm U = 12.35 Bq/kg and 1 ppm Th = 4.06 Bq/kg. NOTE: These coefficients are calculated for natural isotopic abundances of 99.2745% for ^{238}U , 100% of ^{232}Th and 0.0118% of ^{40}K .

Table 1.1: confrontation of some models used for the estimation of cosmic radiation dose based on digital terrain model.

Model description	Cosmic radiation absorbed dose rate
<ul style="list-style-type: none"> DTM SRTM resolution 1 x 1 km grid Ionizing component: $H_I(z) = H_I(0) \left[0.205e^{-1.649z} + 0.795e^{0.4528z} \right]$ Neutron component: $H_N(z) = H_N(0)e^{1.04z} \text{ for } z < 2\text{km}$ $H_N(z) = H_N(0) \left[1.98e^{0.698z} \right] \text{ for } z > 2\text{km}$ <p>where z (km), H_I (H_N) ($\mu\text{Sv/a}$) and $H_I(0) = 240\mu\text{Sv/a}$ and $H_N(0) = 20\mu\text{Sv/a}$</p> <ul style="list-style-type: none"> Latitude effect: NA <p>Model Ref: Bouviell and Lowder 1988</p>	 <p>Cosmic Radiation - Photon, directly ionizing component and neutron dose rate</p> <p>Dose Rate mikroSv/a</p> <ul style="list-style-type: none"> 345-349 350-359 400-449 450-499 500-549 550-599 600-699 700-699 800-1099 1100-1299 1300-1499 >1500 <p>Source: http://ec.europa.eu/dgs/jrc/index.cfm</p>
<ul style="list-style-type: none"> DTM resolution NA Ionizing component: $D(\varphi, H) = a(\varphi) + be^{H/c(\varphi)}$ <p>where D (mrad/a), latitude φ (degree), altitude H (km) b is a constant, and a and c are functions of the latitude</p> <p>$b = 11$</p> <p>$a(\varphi) = 15$ for $\varphi < 25^\circ$</p> <p>$a(\varphi) = 15 + 0.118(\varphi - 25)$ for $25^\circ < \varphi < 42^\circ$</p> <p>$a(\varphi) = 17$ for $\varphi > 42^\circ$</p> <p>$c(\varphi) = 1.96$ for $\varphi < 10^\circ$</p> <p>$c(\varphi) = 1.96e^{-0.0028(\varphi-10)}$ for $10^\circ < \varphi < 50^\circ$</p> <p>$c(\varphi) = 1.75$ for $\varphi > 50^\circ$</p> <ul style="list-style-type: none"> Neutron component: NA <p>Model Ref: Boltneva et al. 1974</p>	 <p>Cosmic-ray Exposure (nGy/hr)</p> <p>Dose (nGy/hr)</p> <ul style="list-style-type: none"> 88 68 54 48 46 44 43 42 40 <p>500 0 500 1500 (kilometers) NAD27/DNAG</p> <p>Source: http://www.usgs.gov/</p>
<ul style="list-style-type: none"> DTM resolution 2 x 2 km grid Ionizing component: $D(z) = 37e^{0.38z}$ <p>where D (nSv/h) and z (km)</p> <ul style="list-style-type: none"> Neutron component: NA Latitude effect: NA <p>Model Ref: Murith and Gunter 1994</p>	 <p>Cosmic dose rate (nSv/h)</p> <ul style="list-style-type: none"> > 170 165 - 170 140 - 155 125 - 140 110 - 125 85 - 110 80 - 95 65 - 80 50 - 65 < 50 No Data <p>20 0 20 40 60 80 Kilometers</p> <p>Fig. 1. Cosmic dose rate map (in nSv/h) of Switzerland. Min. value: 40 nSv/h; Max. value: 191 nSv/h; Average value: 64 nSv/h; Std. deviation 22 nSv/h. Cell size: 2 kmx2 km.</p> <p>Source: Rybach et al., 2002</p>

1.2.1 Potassium, uranium and thorium

Potassium

Natural potassium comprises three isotopes (^{39}K , ^{40}K , ^{41}K) where ^{40}K is the only radioactive potassium isotope having a natural isotopic abundance of 0.0118%. The beta and electron capture decay modes of ^{40}K to ^{40}Ca (89.28%) and ^{40}Ar (10.72%) (**Fig. 1.2**), respectively, the latter followed by the emission of a 1460.8 keV gamma ray, contribute significantly to the natural radioactivity. Potassium in rocks is concentrated mainly in potassium feldspars and micas. Its distribution in weathered rocks and soils is determined by the break-up of these host minerals. Potassium is soluble under most conditions and during weathering is lost into solution.

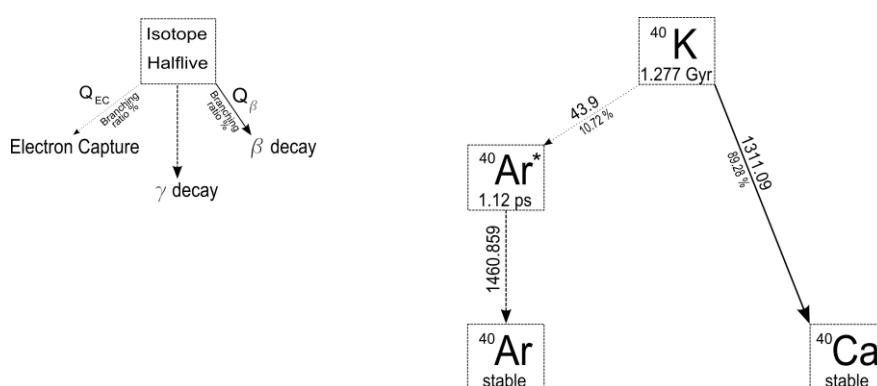


Figure 1.2: potassium decay modes.

Uranium

Natural uranium is mainly constituted by ^{238}U , ^{235}U and ^{234}U created in ^{238}U decay chain, having natural isotopic ratios 99.2745%, 0.730% and 0.0055%, respectively. The decay chain of ^{238}U includes 8 alpha decays and 6 beta decays respectively (**Fig. 1.3**), often associated with gamma de-excitation of nuclei.

Generally uranium and its daughters are found on rough secular equilibrium mainly because weathering and alteration processes during time due to different specific radionuclide mobility along the decay chains. Here are briefly discussed the chemical properties of the some particular isotopes in uranium decay chain.

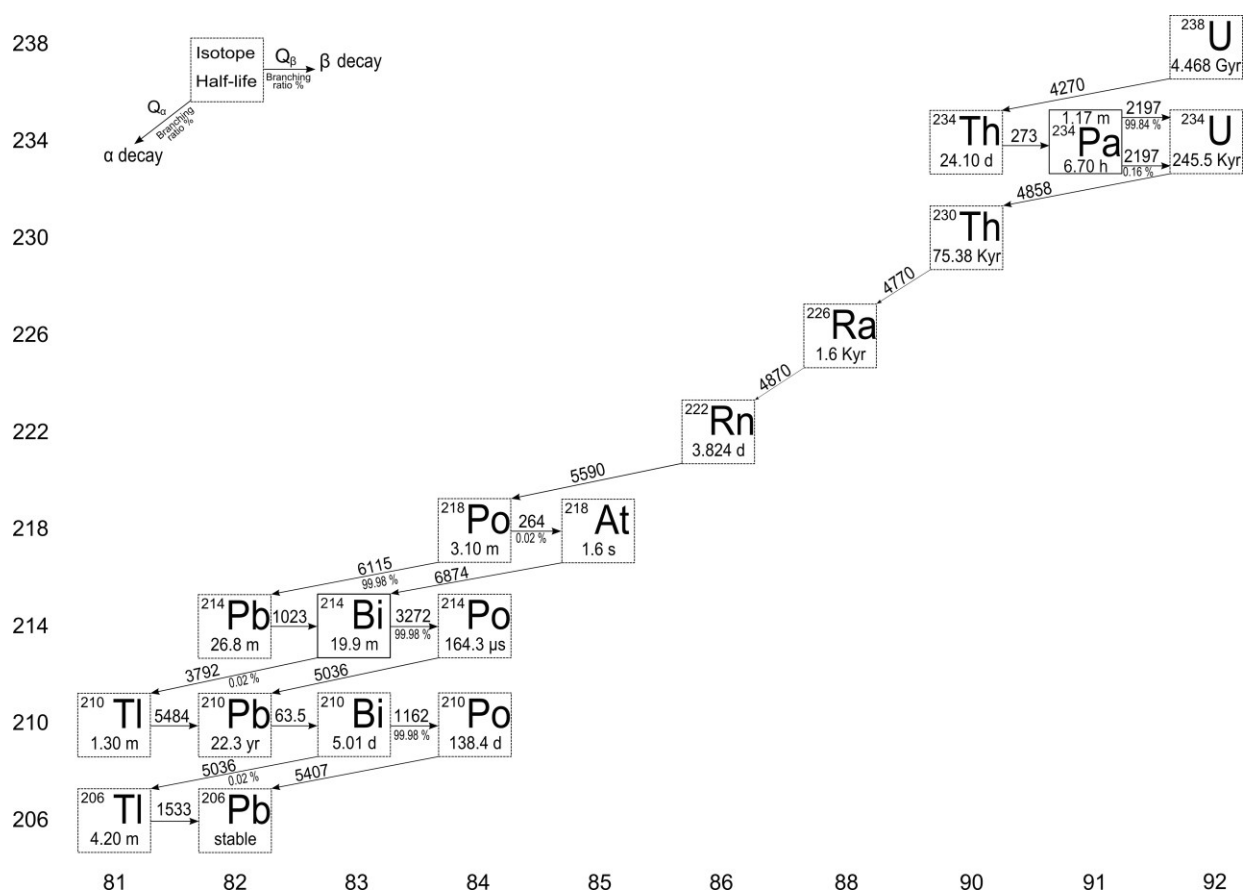


Figure 1.3: uranium decay chain.

The occurrence and the behavior of uranium in aqueous environment, a source of chain disequilibrium, is governed principally by the oxidation-reduction processes. Under oxidizing conditions uranium exists in the hexavalent state (uranyl, U^{6+}) and forms carbonate, phosphate or sulphate complexes that can be very soluble (Langmuir 1978), while under reducing conditions, exists in the tetravalent state (uranous, U^{4+}) which is insoluble. Radium (^{226}Ra) exhibits only the +2 oxidation state in solution, and its chemistry resembles that of barium. Radium forms water-soluble chloride, bromide, and nitrate salts. The phosphate, carbonate, selenate, fluoride, and oxalate salts of radium are slightly soluble in water, whereas radium sulfate is relatively insoluble in water. Radium does not form discrete minerals but can coprecipitate with many minerals, including calcium carbonate, hydrous ferric oxides, and barite (BaSO_4). Radon (^{222}Rn) is a noble gas having a half life of 3.82 days, which can escape from soil to the atmosphere by mechanisms treated extensively by Tanner 1992; Tanner 1980; Tanner 1964. When the parent radium decays in rock or soil, the resulting radon atoms recoil and some of them come to rest in geologic fluids, most likely water in the capillary spaces. Some of the radon in soil water enters soil gas, primarily by diffusion, and then becomes more mobile. Radon reaches the atmosphere mainly when soil gas at the surface exchanges with atmospheric gas. A less important mechanism is diffusion from soil gas to atmospheric gas.

Activity concentrations of ^{222}Rn outdoors vary from <1 up to a few tens of Bq/m^3 (Gesell 1983; NAS NRC 1999). Outdoor radon activity concentrations, however, vary diurnally as a function of the time of day, temperature, atmospheric pressure, humidity, and with exhalation rate from soil (Åkerblom 1986; Wilkening 1990; Mahesh et al. 2005; Kozak et al. 2005).

However, in the study of uranium decay chain through gamma-ray spectrometry techniques it is important to emphasize that some long lived radionuclides (^{238}U , ^{226}Ra , ^{210}Pb) can be the head of decay chain segments which can be directly measured or through secular equilibrium grow-up conditions in less than one year. The segments of ^{234}U and ^{210}Po can not be measured under the above mentioned conditions.

In Table 1.2 are listed the principal isotopes which may form decay chain segments in uranium decay chain, and used to study the secular equilibrium through gamma-ray spectrometry measurements. For each segment chain are indicated the isotopes which can be detected using gamma-ray spectrometry measurements and the grow-up time.

Table 1.2: heads of decay chain segments in uranium decay chain and the respective grow-up times.

Chain-Segment Head	Grow-up time interval (> 99%) ^a	Isotope	Energy (keV)	Intensity (%)
1 ^{238}U	168.7 (d)	^{234}Th	63.9 ^d 92.4 ^e 92.8 ^e	4.80 2.81 2.77
		$^{234}\text{Pa}^m$	1001.0 ^b	0.84
2 ^{234}U	not-detected	-	-	-
3 ^{230}Th	directly-detected	^{230}Th	67.7 ^d	0.38
4 ^{226}Ra	directly-detected 26.7 (d)	^{226}Ra ^{214}Pb	186.2 ^c 351.9 295.2 242.0	3.59 37.6 19.3 7.43
		^{214}Bi	609.3 1764.5 1120.3	46.1 15.4 15.1
5 ^{210}Pb	direct	^{210}Pb	46.5 ^d	4.25
6 ^{210}Po	not-detected	-	-	-

^a Grow-up time (>99%) calculated as 7 time half-life of the longest lived isotope of the chain-segment.

^b Low yield gamma energy.

^c Generally recorded as a doublet with 185.7 keV (^{235}U).

^d Low energy (requires n-type HPGe detector for best sensitivity and accuracy).

^e Recorded as doublet between 92.4 keV and 92.8 keV from ^{234}Th .

Thorium

Natural thorium has only one primordial isotope that of ^{232}Th having an natural isotopic ratio of 100%. The decay chain of ^{232}Th includes 6 alpha decays and 4 beta decays respectively (Fig. 1.4), often associated with gamma de-excitation of nuclei. There are shorter-lived thorium isotopes in all three

natural decay chains, as follows: ^{234}Th (24.1 d half-life) and ^{230}Th ($7.54 \cdot 10^4$ y half-life) in the ^{238}U chain; ^{228}Th (1.9 y half-life) in the ^{232}Th chain; and ^{231}Th (1.06 d half-life) in the ^{235}U chain.

Generally thorium and its daughters are found in secular equilibrium. However, in ^{232}Th decay chain the two chain segments having on head ^{228}Ra and ^{228}Th reach the secular equilibrium in about one month (**Table 1.3**). Thorium occurs in the tetravalent (Th^{4+}) oxidation state and is insoluble except at low pH (near-neutral), or in the presence of organic compounds such as humic acids (**Langmuir and Herman 1980**). At near-neutral pH and in alkaline soils, the precipitation of thorium as a highly insoluble hydrated oxide phase and the co-precipitation with hydrated ferric oxides can, with sorption reactions, are two important mechanisms for the removal of thorium from solution. Because of sorption and precipitation reactions and the low solution rate of thorium-bearing minerals, thorium concentrations in natural waters are generally low. Radium (^{228}Ra) show the same geochemical properties as radium isotope in uranium decay chain. Thoron (^{220}Rn) has a lesser opportunity to escape in the atmosphere than radon isotopes (^{222}Rn) due to its shorter half-life (55.6 s half-life). However, particularly in the last decade, the number of researches on thoron has been increasing especially in indoor ambients. It is worth mentioning that a study carried out in China indicated that the ratio of the average equilibrium equivalent concentration of thoron progeny (EEC Tn) to that of radon progeny (EEC Rn) ranged from 0.06 to 0.13, but the range of the dose ratio (thoron progeny)/(radon progeny) was between 0.31 and 0.47 (**Guo et al. 2005**). This ratio indicates that the dose from thoron progeny may be not negligible for radiological purposes.

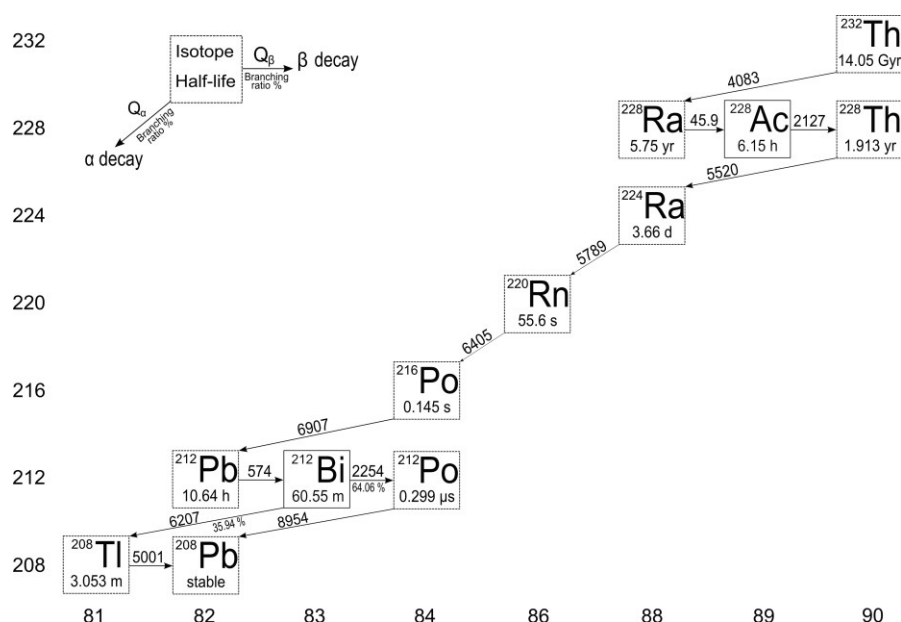


Figure 1.4: thorium decay chain.

In **table 1.3** are listed the principal isotopes which may form decay chain segments in thorium decay chain, and used to study the secular equilibrium through gamma-ray spectrometry measurements. For each segment chain are indicated the isotopes which can be detected using gamma-ray spectrometry measurements and the grow-up time.

Table 1.3: heads of decay chain segments in thorium decay chain and the respective grow-up times.

Chain-Segment Head	Grow-up time interval (> 99%) ^a	Isotope	Energy (keV)	Intensity (%)
1 ²³² Th	not-detected	-	-	-
2 ²²⁸ Ra	1.8 (d)	²²⁸ Ac	911.1	26.0
			968.9	16.2
			338.4	11.3
3 ²²⁸ Th	25.7 (d)	²¹² Pb	115.2	0.592
			238.6	43.3
			300.1	3.28
		²¹² Bi	727.2	6.58
			1078.6	0.564
			1620.56	1.49
		²⁰⁸ Tl	583.1	84.5
			860.5	12.42
		2614.0	99	

^a Grow-up time (>99%) calculated as 7 time half-life of the longest lived isotope of the chain-segment.

Terrestrial absorbed dose rate coming from external gamma radiation

For health protection purposes the absorbed dose rate coming from the external gamma radiation can be calculated by knowing the activity concentrations in soil using a simple formula:

$$D (nGy h^{-1}) = C_K S_K + C_U S_U + C_{Th} S_{Th} \quad (\text{Eq. 1.1})$$

where S_{Th} , S_U , and S_K are the dose conversion coefficients for Th, U, and K, respectively (**Table 1.4**) and C_{Th} is the activity concentration measured through the ²⁰⁸Tl photo-peak (in Bq/kg), C_U is the activity concentration measured through the ²¹⁴Bi photo-peaks (in Bq/kg), and C_K is the activity concentration measured through the ⁴⁰K photo-peak (in Bq/kg). In general the estimates of uranium and thorium concentration is based on the assumption of equilibrium conditions through the direct measurement of daughter isotopes and therefore usually reported as “equivalent uranium” (eU) and “equivalent thorium” (eTh).

Table 1.4 shows the evolution of dose conversion coefficients in nGy/h per Bq/kg as reported by the United Nations Scientific Committee on the Effects of Atomic Radiation (**UNSCEAR 2000**) and other publications. The dose coefficients listed in **Table 1.4** have been used worldwide throughout the years since published. The slight differences in dose coefficients are not taken into consideration in most calculations.

Table 1.4: dose conversion coefficients for external gamma radiation coming from natural radionuclides present in soil.

Reference	S_K (nGy h ⁻¹ / Bq kg ⁻¹)	S_U (nGy h ⁻¹ / Bq kg ⁻¹)	S_{TH} (nGy h ⁻¹ / Bq kg ⁻¹)
UNSCEAR 1977; Beck 1972	0.043	0.427	0.662
ICRU 1994; Saito and Jacob 1995; Saito et al. 1998; UNSCEAR 2000	0.0417	0.462	0.604
Eckerman and Ryman 1993	0.046	0.561	0.682

1.2.2 Radioactive decay series

The natural decay series of ²³⁸U, ²³⁵U and ²³²Th are an example of natural radioactive decay series and therefore are briefly discussed in this section. Radioactive decay series (or chain) often occurs in a number of daughter products, which are also radioactive, and terminates in a stable isotope $A(\lambda_A) \rightarrow B(\lambda_B) \rightarrow C(stable)$. Assuming that at time $t = 0$ we have N_{A_0} atoms of the parent element and no atoms of the decay product are originally present, the number of parent nuclei decrease with time according to the [Eq 1.2](#).

$$\frac{dN_A}{dt} = -\lambda_A N_A \quad (\text{Eq. 1.2})$$

where

$$N_A = N_{A_0} e^{-\lambda_A t} \quad (\text{Eq. 1.3})$$

While the number of daughter nuclei increases (grow-up) as a result of decays of the parent and decreases as a result of its own decay:

$$\frac{dN_B}{dt} = \lambda_A N_A - \lambda_B N_B \quad (\text{Eq. 1.4})$$

The solution of the first order differential equation $(dN_B / dt) + \lambda_B N_B = \lambda_A N_{A0} e^{-\lambda_A t}$ is of the form $N_B = A e^{-\lambda_A t} + B e^{-\lambda_B t}$ and by substituting into the above equation with the initial conditions described above we find:

$$N_B = \frac{\lambda_A N_{A0}}{\lambda_B - \lambda_A} (e^{-\lambda_A t} - e^{-\lambda_B t}) \quad (\text{Eq. 1.5})$$

From [equations 1.3](#) and [1.5](#) can be calculated the relative activity ratio of the two species:

$$\frac{\lambda_B N_B}{\lambda_A N_A} = \frac{\lambda_B}{\lambda_B - \lambda_A} [1 - e^{-(\lambda_B - \lambda_A)t}]$$

- $\lambda_A \ll \lambda_B$: in the case when the half-life of nuclide A is much greater than the half-life of nuclide B, so the parent decays at constant rate we have:

$$\lambda_B N_B = \lambda_A N_{A0} (1 - e^{-\lambda_B t})$$

This equation express the **secular equilibrium condition**, where as t becomes large nuclei B decay at the same rate at which they are formed: $\lambda_B N_B = \lambda_A N_{A0}$. This result can also be immediately obtained from [equation 1.4](#), taking $dN_B / dt = 0$. For practical purposes, equilibrium may be considered established after seven daughter half-lives (more than 99% of daughter nuclides grow-up) ([Fig. 1.5](#)).

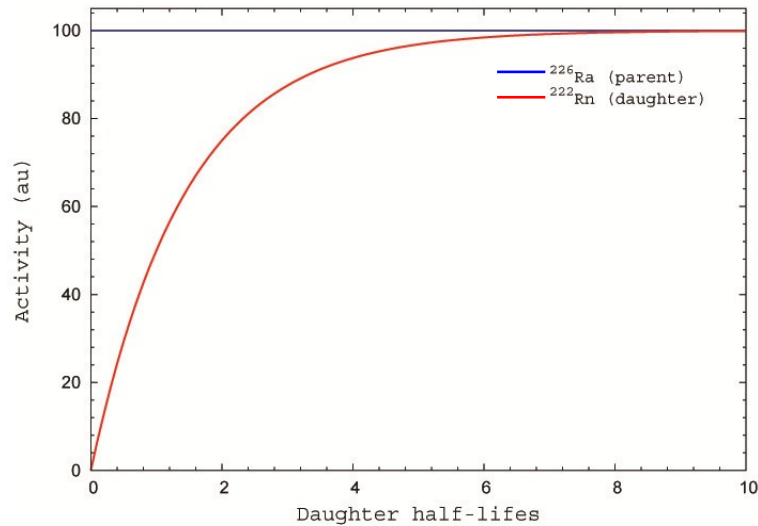


Figure 1.5: secular equilibrium buildup of a very short-lived daughter (^{222}Rn of half-life 3.824 d) from a long-lived parent (^{226}Ra of half-life 1600 y). The activity (arbitrary unit) of the parent remains constant, while the activity of the daughter reaches secular equilibrium (more than 99%) just after seven half-lives.

- $\lambda_A < \lambda_B$: as t increases, the exponential term becomes smaller and the activity ratio (A_B / A_A) approaches the limiting constant value $\lambda_B / (\lambda_B - \lambda_A)$. The activities themselves are not constant, but the nuclei of type B decay (in effect) with the decay constant of type A. This situation is known as **transient equilibrium condition (Fig. 1.6)**.

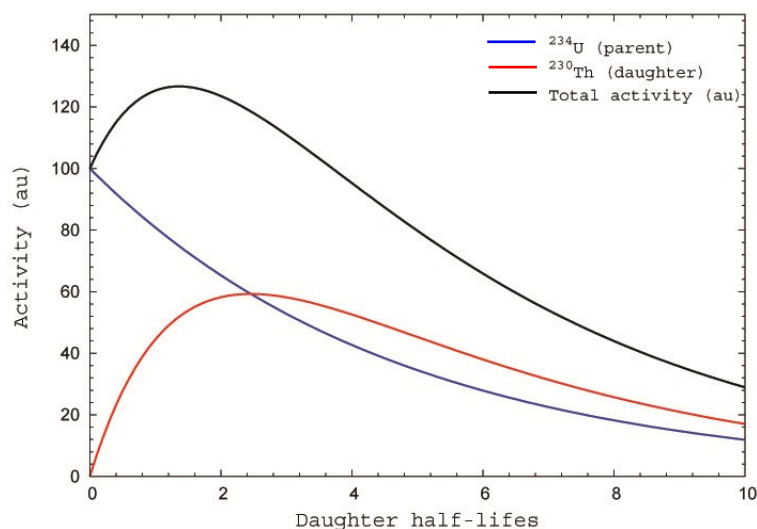
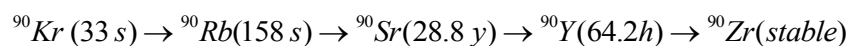


Figure 1.6: transient equilibrium of the decay of ^{234}U (of half-life 2.45×10^5 y) to ^{230}Th (of half-life 7.54×10^4 y). The activity ratio daughter/parent approaches the constant value 1.48.

- $\lambda_A > \lambda_B$: in the case when the parent decays quickly, ($\lambda_A > \lambda_B$), and the daughter activity rises to a maximum and then decays with its characteristic decay constant, if t is so long the number of nuclei type A is small ($e^{-\lambda_A t} \sim 0$): $\lambda_B N_B \approx (\lambda_B \lambda_A N_A / \lambda_A - \lambda_B) e^{-\lambda_B t}$, which reveals that the type B nuclei decay approximately according to the exponential law (Fig. 1.7). An example of no equilibrium condition, is the nuclear fission product series containing ^{90}Sr which is largely studied for environmental radioprotection purposes:



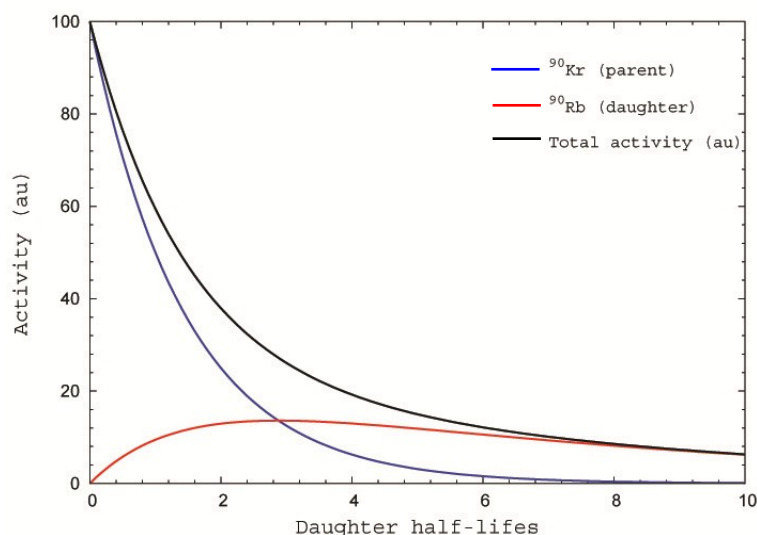


Figure 1.7: no equilibrium: the growth and decay of ^{90}Rb (of half-life 158 s) from ^{90}Kr (of half-life 33.33 s). If ^{90}Kr is not continuously produced it will vanish more quickly producing ^{90}Rb which on turn will vanish quickly respective ^{90}Sr having a much longer half-life and reaching secular equilibrium with its daughter ^{90}Y .

Another example of no-equilibrium condition is the growth of ^{235}U (7.04×10^8 y) from ^{239}Pu (2.41×10^4 y): indeed the head isotope of this decay chain is ^{235}U .

1.3 Man-made radionuclides

Fallout from atmospheric weapon testing and from NPP accidents

Over 2000 nuclear tests distributed all over the world from 1945 to 1998 gave rise to the atomic age causing a global radiological contamination. The estimated global release of ^{137}Cs and ^{131}I from atmospheric nuclear weapon testing were respectively 9.48×10^{17} Bq and 6.75×10^{20} Bq (**UNSCEAR 2008**). In the **figure 1.8** below are distributed the nuclear test around the world divided in atmospheric and underground regarding their yield.

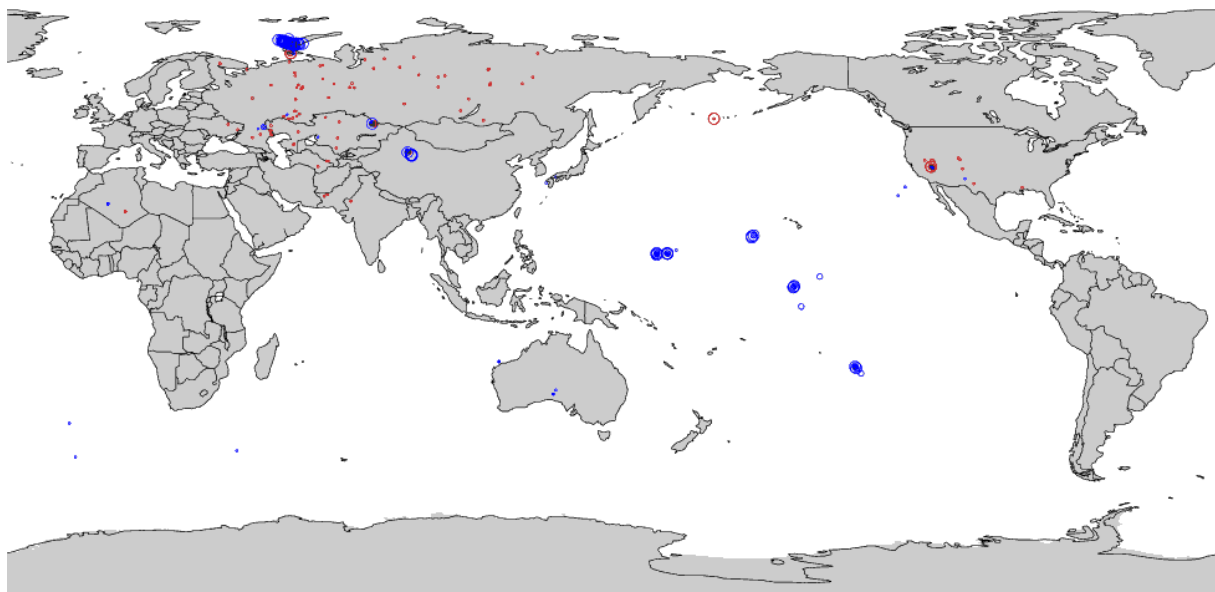


Figure 1.8: the global distribution of the locations of all nuclear tests and other detonations worldwide. Atmospheric tests are in blue, underground tests in red. Successively larger symbols indicate yields from 0 to 150 kt, from 150 kt to 1 mt, and over 1 mt. Data taken from: <http://www.johnstonsarchive.net/>.

About 30 major NPP incidents and accidents have occurred, ranked by INES (International Nuclear and Radiological Event Scale) scale, with Chernobyl and Fukushima as the first two accidents caused more damages and contamination. There are over 440 nuclear power plants for electricity generation with 60 more NPP under construction (IAEA 2011), which operate in about 30 countries (Fig. 1.9) producing about 14% of world electricity demand.



Figure 1.9: distribution of 440 nuclear power plants operating around the world.

According to INES scale (IAEA 2008) Chernobyl (1986) and Fukushima (2011) are classified as the most severe accidents occurred in nuclear power industry. Chernobyl accident caused the largest uncontrolled radioactive release into the environment; when large quantities of radioactive substances were released into the air for about 10 days. The radioactive cloud dispersed over the entire northern hemisphere, and deposited substantial amounts of radioactive material over large areas. A enormous number of studies have been undertaken in order to estimate the fallout distribution in particular the two radioisotopes, the short-lived ^{131}I (8 d half-life) and the long lived ^{134}Cs (2 y half-life) and ^{137}Cs (30 y half life) which are particularly significant for the radiation dose they deliver. In the figure below is shown the combined work of many countries showing the distribution of ^{137}Cs all over the world guided by European Commission Joint Research Centre (Fig. 1.10).

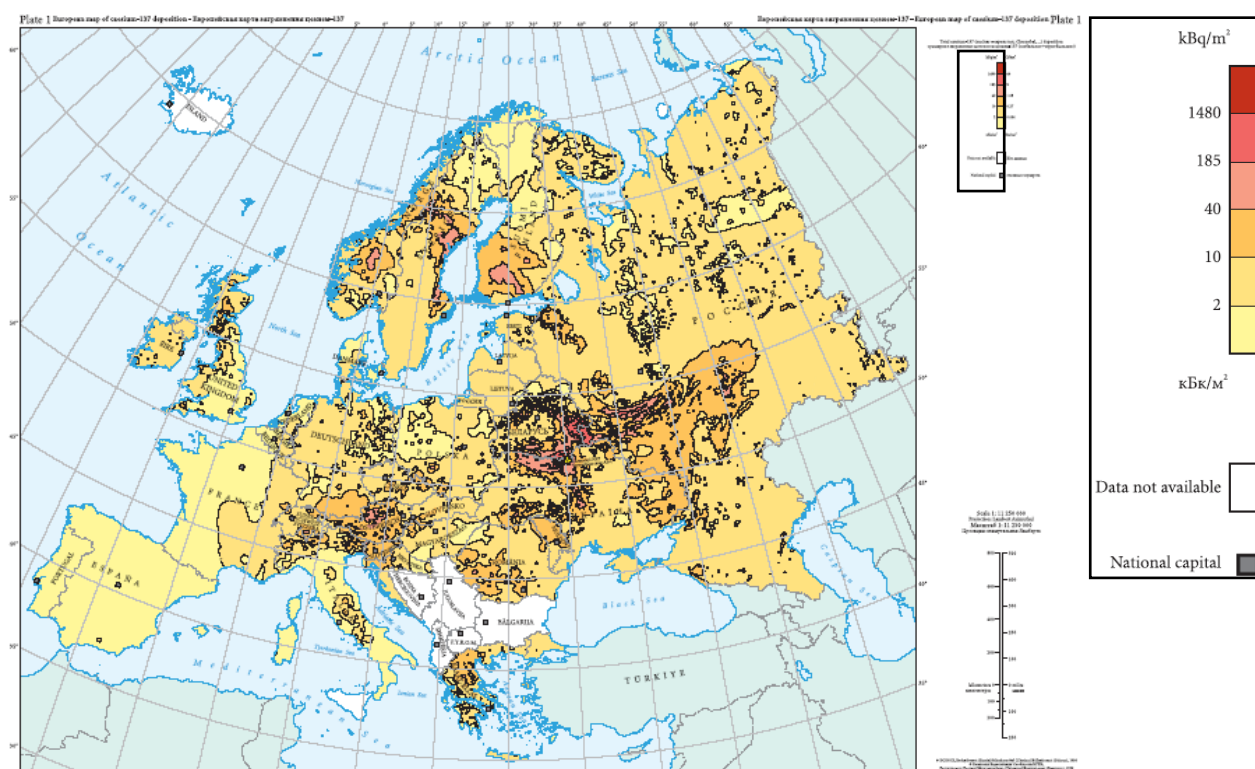


Figure 1.10: European map 1 : 11 250 000 of ^{137}Cs deposition following Chernobyl NPP accident. Data taken from: <http://rem.jrc.ec.europa.eu/>.

Recently, Japan was hit by a 9.0 magnitude earthquake followed by a tsunami that affected hundreds of thousands of people and seriously damaged the Fukushima Daichi power plant in Japan, where radioactive emissions from Fukushima spread across the entire northern hemisphere. Fukushima nuclear power plant accident was classified as INES scale 6 regarding to Chernobyl (INES scale 7). In **Table 1.5** are compared the radionuclide release budget from the Chernobyl accident (**UNSCEAR**

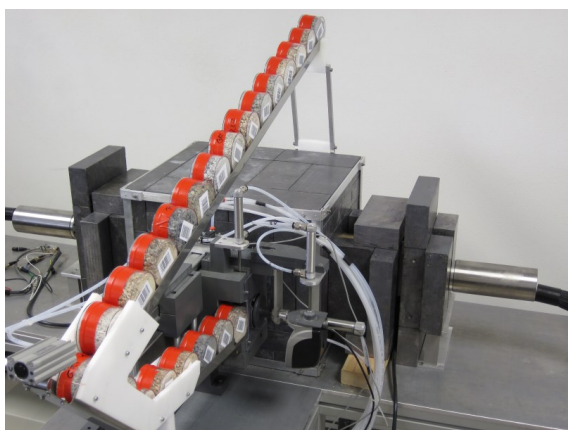
2008) which can be compared with Fukushima first data received, showing about one order of magnitude differences between them.

Table 1.5: principal radionuclides released (volatile elements) in Chernobyl accident compared to those assumed from Fukushima Dai-ichi accident.

Radionuclide	Half-life	Activity released (10^{15} Bq)		
		Chernobyl UNSCEAR 2008	Fukushima Dai-ichi (NISA) http://www.nisa.meti.go.jp/	Fukushima Dai-ichi (NSC) http://www.nsc.go.jp/
^{131}I	8.04 d	~1760	130	150
^{134}Cs	2.06 y	47	-	-
^{137}Cs	30.0 y	~85	6.1	12

Chapter 2

Laboratory γ -ray spectrometry: a fully automated low-background high-resolution γ -ray spectrometer



MCA_Rad system composed by two coupled HPGe detectors accurately shielded and an automatic sample changer driven by electromechanical pistons using compressed air.

- 2.1 **MCA_Rad system: set-up design and automation**
 - 2.1.1 *Features of HPGe detectors*
 - 2.1.2 *Shielding design and evaluation*
 - 2.1.3 *Automation: hardware and software developments*
- 2.2 **MCA_Rad system calibration**
 - 2.2.1 *Energy calibration*
 - 2.2.2 *Efficiency calibration with uncertainty budget*
- 2.3 **Case of study: bedrock radioelement mapping of Tuscany Region**
 - 2.3.1 *Representative sampling strategy and sample preparation*
 - 2.3.2 *Summary of the results: mapping of radioelements*
- 2.4 **Appendix A: calculation of simplified coincidence summing correction factor for ^{152}Eu**

Chapter 2

Laboratory γ -ray spectrometry: a fully automated low-background high-resolution γ -ray spectrometer

2.1 MCA_Rad system: set-up design and automation

2.1.1 Features of HPGe detectors

The core of MCA_Rad system is composed by two coupled HPGe detectors described in details in [Table 2.1](#). The choice of HPGe detectors must be made taking into account their characteristics in order to match their response functions without losing any singular information during spectra summing. Here are analyzed the characteristics of the two HPGe detectors composing the MCA_Rad system.

The **relative efficiency**² is an important feature of HPGe detectors which is related with crystal volume and shape. Moreover the **peak-to-Compton ratio** is also an important quoted feature for coaxial HPGe detectors expressed as the 1332 keV (⁶⁰Co) peak height divided by the average counts measured over the energy region from 1040 to 1096 keV associated with the peak. As defined in

² According [ANSI No.42.14 1999](#) the relative efficiency is defined as, $\varepsilon_r = N / At\varepsilon_{NaI(Tl)}$, calculated as relative to that of a 7.6 cm x 7.6 cm cylindrical NaI(Tl) detector ($\varepsilon_{NaI(Tl)} = 1.2 \times 10^{-3}$) for 1332 keV gamma-ray (N) emitted by ⁶⁰Co of known activity (A) counted 25 cm from the face of the detector for a time (t).

ANSI No.42.14 1999, the peak-to-Compton ratio is dependent on the energy resolution and the detector efficiency and therefore gives a better description of the detector performance than does either the detection efficiency or energy resolution alone. It can be seen that there is a slight difference between the two detectors which can be expected since the relative efficiencies are slightly different.

Table 2.1: the features of the two detectors used in the project design of MCA_Rad system.

Description	Detector A	Detector B
Detector type (ORTEC®)	cylindrical coaxial p-type	cylindrical coaxial p-type
HPGe crystal net volume (cm ³)	234.4	292.84
HPGe crystal base surface (cm ²)	65.00	56.58
HPGe crystal length (cm)	5.43	7.96
End-cup type	1.5 mm Al	1.5 mm Al
Relative efficiency (⁶⁰ Co gamma-ray at 1332 keV)	60%	67%
FWHM at 1332 keV (⁶⁰ Co)	1.67 keV	1.84 keV
FWHM at 122 keV (⁵⁷ Co)	0.77 keV	0.82 keV
Peak shape (FWTM/FWHM) for ⁶⁰ Co	1.9	1.9
Peak shape (FWFM/FWHM) for ⁶⁰ Co	2.4	2.6
Peak-to-Compton ratio (⁶⁰ Co gamma-ray at 1332 keV)	81:1	83:1
HPGe cooling system	electro-mechanical	electro-mechanical
Positive High Voltage (kV)	4.8	2.0

Figures represent values measured by the manufacturer.

During spectra summing some response function characteristics of individual detectors may be lost due to the difference in energetic resolution: the values indicated in **table 2.1** shows the differences in energy resolution for the two detectors. It is important to keep in mind that the energetic resolution has specific limitations due to the gain settings (MCA_Rad system overall gains of 1.00 and 1.01 for detector A and B respectively) and the channels comprising the spectrum. For example, in 8192 channels covering an energetic region from 0 to 3 MeV, each channel is 0.37 keV wide and the difference between 1.87 and 1.64 keV (or 0.77 and 0.82 keV) FWHM resolution will not be seen in the spectrum and therefore does not influence the spectrum shape characteristics after summing. The peak shape is another important feature which can change the characteristics of the resulting spectra. Just to remember, a Gaussian function has a FWTM/FWHM = 1.82 and a FWFM/FWHM = 2.3, where the FWTM and FWFM are the energy resolutions at tenth and at fiftieth maximum, respectively. When the peak shape closely approximates a Gaussian function no additional fitting components in spectrum analysis are required (e.g., one or more tailing terms). **ANSI No.42.14 1999**

can provide guidance in specifying and measuring these peak-shape parameters. The shape peak characteristics shown in [table 2.1](#) indicate a near Gaussian function with similar characteristics.

2.1.2 Shielding design and evaluation

The core of the MCA_Rad system consist in two vertical p-type HPGe gamma-ray spectrometers ([Table 2.1](#)) facing each other at about 5 cm apart ([Fig. 2.1a](#) and [Fig. 2.1b](#)). The two detectors are controlled by individual integrated gamma spectrometers for the digital signal processing using commercial software for spectra acquisition. The new cooling technology which use mechanical coolers permits to simplify the management of the system, however, a similar system was developed also for LN₂ cooled HPGe detectors.

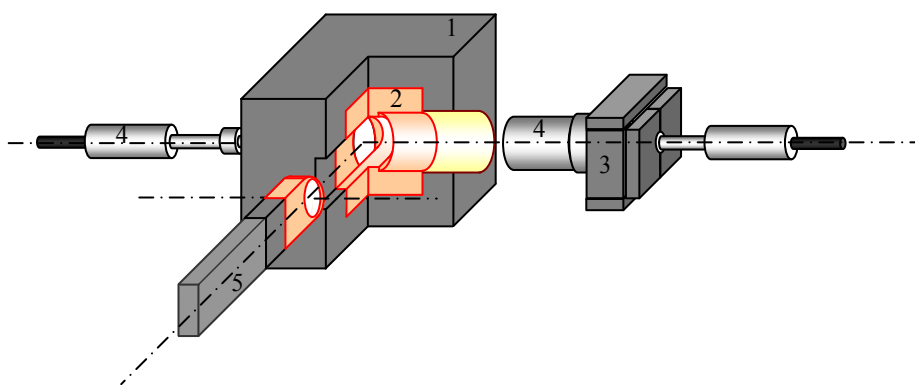


Figure 2.1a: schematic design of the MCA_Rad system. 1) The main lead shielding construction (20 cm x 25 cm x 20 cm). 2) The core copper shielding (10 cm x 15 cm x 10 cm). 3) The rear lead shielding construction. 4) HPGe semiconductor detectors. 5) The mechanical sample changer.

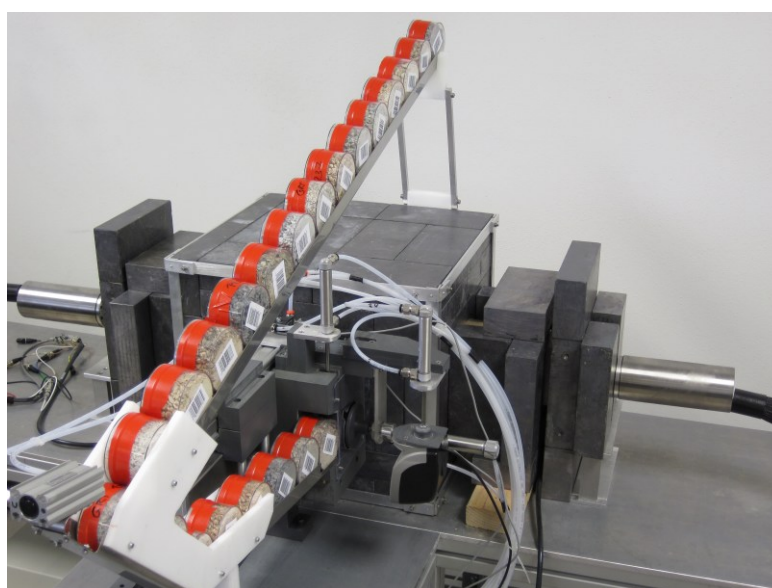


Figure 2.1b: view of MCA_Rad system.

The shielding construction is an important parameter in gamma-ray spectrometry regardless of the activity level of the sample being counted. As a good practice graded shielding is commonly used: indeed in order to attenuate higher energy KX-rays (up to about 90 keV) of lead a layer of cadmium is used producing itself an intermediate KX-ray (26.7 keV) and a layer of copper in reduces the KX-ray to 8.98 keV. In **figure 2.2** are shown the total attenuation coefficients of surrounding materials of the HPGE detector: here can be directly seen the migration of KX-rays toward lower energies due to attenuation.

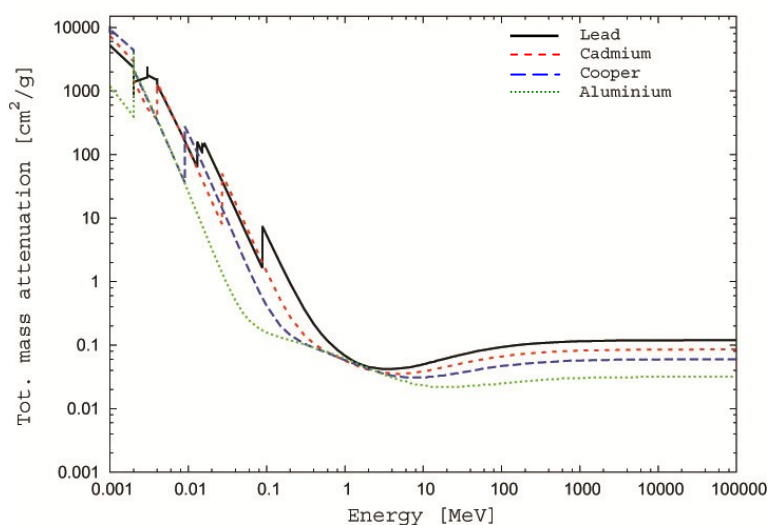


Figure 2.2: the total attenuation coefficients of a standard graded shielding composition showing the migration of X-rays toward low energy range. Data taken from National Institute of Standards and Technologies (NIST) (<http://www.nist.gov>) XCOM 3.1 Photon Cross Sections Database.

The background radiation is mainly due to a combination of:

- radio-impurities present in the detectors constituent materials,
- radio-impurities in the shielding materials,
- environmental terrestrial gamma radiation and laboratory structures,
- radioactivity in air surrounding the detector: mainly due to radon gas and
- primary and secondary components of the cosmic radiation.

The radioactivity concentration of common detector construction and shielding materials is in large part due to low concentrations of naturally radioactive elements often contained as impurities. The reduction of radon gas in air is sometimes solved using airtight volume constructions around the detector and purged with radon free-gas, like N₂. The cosmic radiation has a significant contribution in

background radiation and is generally solved with construction of underground laboratories, while in surface laboratories the sea-level height at laboratory location is a distinguishable parameter for background reduction knowing that the cosmic radiation doubles every 1.5 – 2 km. MCA_Rad system is located at a facility at about 15 m height above sea level. However, the most important component of background radiation for environmental measurements is the terrestrial and facility radiation. Therefore, in order to effectively reduce the environmental gamma radiation an adequate shielding construction is needed.

In the MCA_Rad system, around the two detectors configuration is constructed a dedicated shielding design (**Fig. 2.1a**). A 10 cm thick lead house shields the detector assembly, leaving an inner volume around the detectors of about 10 dm³. As we mentioned above, the commercial lead bricks often used as shielding materials are certified having a specific activity of 25 mBq/g. This activity is mainly due to the presence of ²¹⁰Pb, produced by ²³⁸U decay chain and obviously adds some extra background in the blank spectrum. This isotope having an half life of 22.3 years shows itself with a gamma energy of 46.5 keV and a bremsstrahlung continuum from beta decay of its daughter ²¹⁰Bi, extending from low energy up to 1162 keV. Furthermore, as we described above, when a gamma ray strikes the lead surface, characteristic lead X-rays may escape and hit the detector. For this reason and for structural stability purposes the inner volume is occupied by 10 cm thick oxygen free copper house leaving empty only the space devoted to host the sample under investigation. This choice has also the advantage that reduces the air volume around the detector, but shows two disadvantages: firstly fixes the sample volume and secondly rises the costs of the shielding construction. In order to reduce the X-rays and high energy beta particles coming from the sample, the end-cup windows of the detectors is further shielded with a tungsten (W) alloy sheet of 0.6 mm. A 10 mm thick bronze cylinders and walls of about 10 cm of lead are also used to shield the rear part of the system (**Fig 2.1b**).

In **figure 2.3** is shown the background spectra acquired for 100h: the spectra without shielding (in red) was measured for bared detectors, positioned distant to shielding construction and the spectra with shielding (in green) is measured for the final shielding configuration. The final intrinsic background is reduced by two order of magnitude respect to unshielded detectors. However, while a graded shield reduces fluorescence X-rays, it enhances the counts in the low-energy range. A particularly interesting section of the spectrum are magnified in **figure 2.3**. Neutrons are produced in upper atmosphere and from muon interactions in the shield itself as cosmic-ray reaction products. These naturally occurring neutrons will interact with the bulk shield and with the detector crystal (e.g., observe the 139 keV ^{75m}Ge and 198 keV ^{71m}Ge. These and others peaks result from (n,n') and (n,γ) reactions that emit prompt or decay gamma-rays discussed more in details in **Bossew 2005** and **Gehrke and Davidson**

2005. In [table 2.2](#) we report the background count rates and the sensitivity of the measurement expressed by L_D for the main gamma lines of radionuclides used in environmental radioactivity measurements.

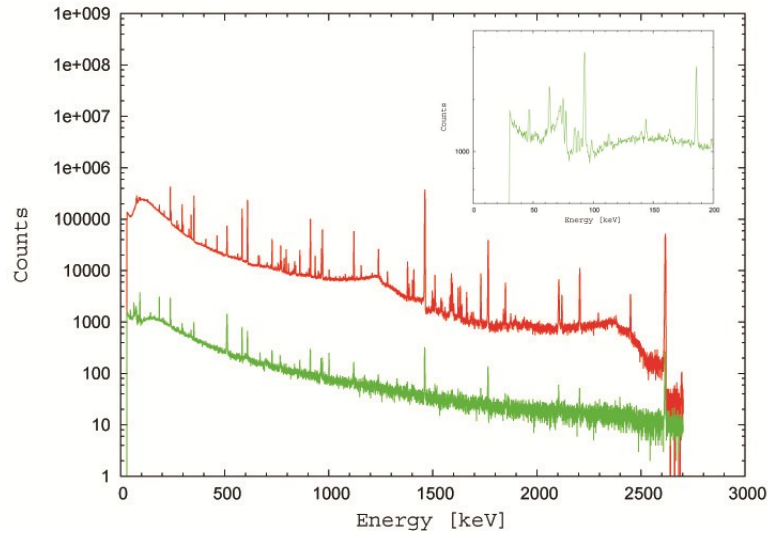


Figure 2.3: MCA_Rad system background spectra (live time 100h) without (red) and with (green) shielding showing a reduction of two order of magnitudes.

As a good practice of gamma-ray spectrometry analysis, the knowledge of background spectra is required in order to detect any potential residual contaminations and for background corrections. A measurement with acquisition time of several days is performed regularly. The final sensitivity of the measurements can be evaluated by using the detection limit (L_D) described in ([Currie 1986](#)) assuming a Gaussian distribution of the events B and rejecting the data not included in a range of 1.645σ (95% confidence level):

$$L_D = 2.71 + 4.65\sqrt{B} \approx 4.65\sqrt{B} \quad (\text{Eq. 2.1})$$

where the approximation is admitted for high number of counts ([Table 2.2](#)).

The minimum detectable activity (MDA) for the blank test is calculated using the L_D , according to the formula:

$$MDA = \frac{L_D}{\epsilon I_\gamma t} \quad (\text{Eq. 2.2})$$

where ε is the efficiency, $I\gamma$ is the gamma line intensity and t is the acquisition live time.

Table 2.2: characterization of MCA_Rad system background (Bckg. without shielding and Bckg. with shielding) expressed in count per hour (cph) for the most intense energetic lines and the corresponding detection limit L_D in counts (Eq. 2.1) for 95% confidence interval (CI) and minimum detectable activity (MDA) in Bq/kg (Eq. 2.2).

Parent Nuclide	Daughter Nuclide	Energy (keV)	I (%)	Bckg. without (Counts)	BCkg. with (Counts)	$L_D(5\%)*$ (Counts)	MDA* (Bq/kg)
^{238}U	$^{234\text{m}}\text{Pa}$	1001.0	0.837	180 ± 13	8 ± 1	21	22.16
	^{214}Pb	351.9	35.8	9704 ± 40	31 ± 2	49	0.50
	^{214}Pb	295.2	18.5	5165 ± 37	13 ± 2	51	0.35
	^{214}Bi	609.3	44.8	10273 ± 34	44 ± 1	32	0.49
	^{214}Bi	1764.5	15.36	2801 ± 16	27 ± 1	13	1.97
	^{214}Bi	1120.3	14.8	3022 ± 21	17 ± 1	23	1.67
	^{214}Bi	1238.1	5.86	1152 ± 17	9 ± 1	19	3.58
^{232}Th	^{228}Ac	911.2	26.6	5050 ± 26	27 ± 1	27	0.94
	^{228}Ac	968.9	16.2	3045 ± 21	17 ± 1	24	1.38
	^{228}Ac	338.3	11.3	3014 ± 33	7 ± 2	51	1.47
	^{212}Pb	238.6	43.3	12984 ± 52	100 ± 2	62	0.46
	^{212}Bi	727.3	6.58	1463 ± 21	10 ± 1	31	3.00
	^{208}Tl	2614.5	99	4857 ± 20	64 ± 1	9	1.58
	^{208}Tl	583.2	84.5	6579 ± 30	42 ± 1	33	0.71
^{40}K	-	1460.8	10.7	24947 ± 47	151 ± 1	19	5.53

* Values calculated for typical background (with shielding) spectra of 1h counting time.

2.1.3 Automation: hardware and software developments

The MCA_Rad system is designed as a stand alone low-background gamma-ray spectrometer composed by two coupled HPGe detectors as described above. The MCA_Rad system is fully automated for normal working processes including automatic samples changer and spectrum analysis.

The mechanical automation consist on a set of compressed air driven electro-pneumatic valves programmed under Agilent VEE graphical language environment using an Agilent 34970A Data Acquisition Switch Unit. The Agilent 34970A consists of a three-slot mainframe with a built-in 6 1/2

digit digital multimeter with specialized plug-in modules. The main processes managed during measurement processes are (Fig. 2.4):

- sample identification,
- sample introduction and/or expel,
- spectrum acquisition and save,
- cycle until end job.

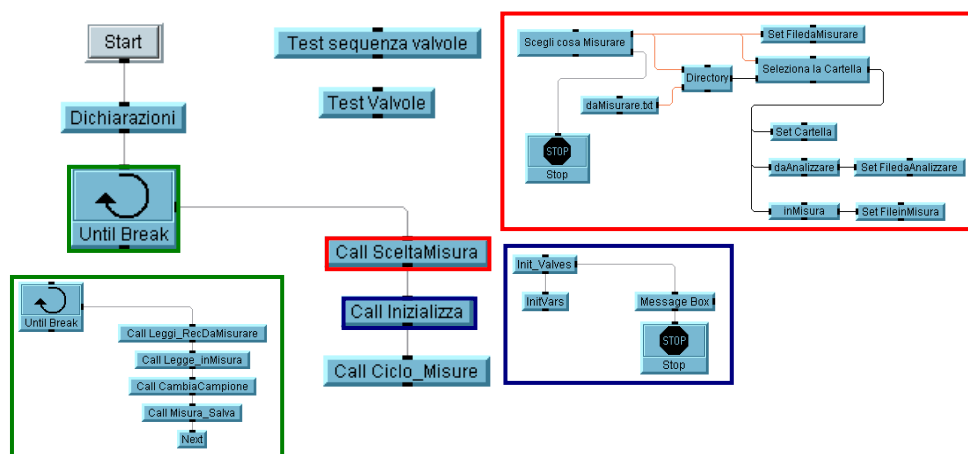


Figure 2.4: the VEE graphical algorithm which drive the MCA_Rad system.

Sample material is contained in a cylindrical polycarbonate box of 75 mm in diameter and 45 mm in height (180 cm³ of useful volume), labeled by a barcode which allow the sample identification through a barcode scanner and permitting the match with the job batch file. The software receives by the operator an input file with the relevant information about the slot of samples: acquisition live time, spectra file name, sample weight, sample description and barcode. Up to 24 samples can be charged in a slider moving on gravity and further introduced at the inner chamber through an automatic “arm” made of copper, lead and plastic closing the lateral hole of the housing and matching with the main shield material.

Furthermore the program control the spectrum acquisition procedure automatically generating and running a job file (commonly used by commercial software) which contain relevant information containing duration of acquisition live time and spectra nomination codes. At the end of the each measurement the procedure is repeated until whether no more samples are detected by the bar-code reader or an error is detected in the sample change procedure generating a batch file used to automatically analyze the spectra.

The VEE algorithm is used also for a similar system which uses LN₂ cooled HPGe detectors (not

discussed here). In order to supervise the detector temperature through a PT100 device placed at the LN₂ output port of the detector dewars (every 12 hours or in case of a detector temperature early rise) and automatically refill the dewars with LN₂ from a connected deposit permitting a normal work in completely independence for one week. The refilling procedure is continuously represented graphically together with the detector temperature history.

2.2 MCA_Rad system calibration

2.2.1 Energy calibration

The energy calibration (gamma-ray energy as a function of channel number) of the HPGe spectrometer system is established by measuring the position of selected full-energy gamma-ray peaks with large peak-height to background ratios, and whose energies are known precisely. The source is chosen that the gamma-rays cover the energetic range of interest 200 – 3000 keV. As we described above the MCA_Rad system is composed by two coupled HPGe detectors, and in order to increase the detection efficiency the two simultaneously measured spectra are summed together. For this reason an accurate energetic calibration of the system, and a periodical check is required. When a shift greater than ± 0.5 keV is observed, the energetic calibration procedure is repeated. Furthermore, in order to allow the direct comparison of spectra from different detectors it was seen useful to adjust at same values the ADC zeros and discriminators along with the gains. However, the summing of the spectra is done after re-binning and energetically calibrating the two simultaneously measured spectra.

The calibration source is counted for a duration time that gives sufficient counts in the peaks to permit measurements of the peak position with a precision of less than ± 0.2 keV. The peak positions at the calibration energies is used to determine the coefficients of the fitting function (linear) for the energetic calibration of MCA_Rad system. In [figure 2.5](#) is shown the energy calibration of summed spectra after re-binning, for the MCA_Rad system.

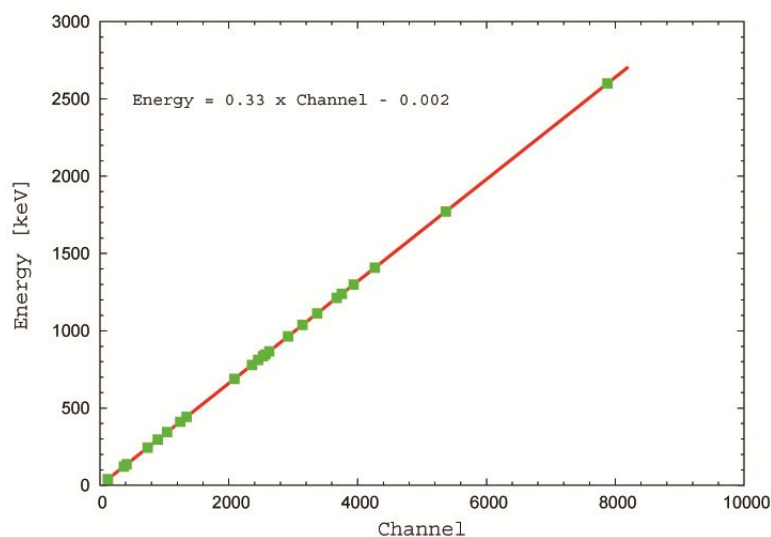


Figure 2.5: energy calibration function for the MCA_Rad system.

2.2.2 Efficiency calibration with uncertainty budgeted

The efficiency calibration of the MCA_Rad system is done determining the full energy peak efficiency, $\varepsilon_p(E)$, as a function of energy using two low activity point sources with complex decay schemes (DeFelice et al. 2006): a certificated ^{152}Eu source, with an activity of 6.56 kBq (certified by ENEA in 1995), known with an uncertainty of 1.5% and a ^{56}Co home made source, that has been normalized to the previous one using the 847 keV gamma line. The ^{56}Co source is used in order to extend the efficiency calibration for gamma energies up to 3000 keV (in Fig 2.6 are shown for ^{152}Eu and ^{56}Co point sources and background spectra normalized to 1 h).

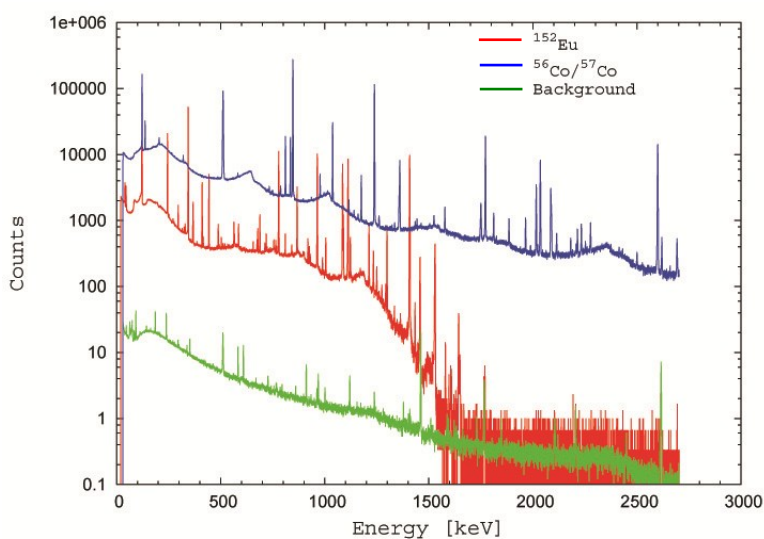


Figure 2.6: standard spectra of ^{152}Eu , ^{56}Co and background normalized for one hour.

The full energy peak efficiency values, $\varepsilon_p(E)$, for the particular gamma-lines emitted from standard point source are calculated from the standard spectra (**Fig. 2.6**) using the general **equation 2.3**:

$$\varepsilon_p(E) = \frac{R}{Ap_\gamma} C_{D1} C_{D2} C_{RS} C_{CS} C_G C_{SA} \quad (\text{Eq. 2.3})$$

when R is the background corrected count rate in the photopeak (**Eq. 2.4**) for the standard spectrum calculated as

$$R = \frac{N}{t_s} = \frac{1}{t_s} \left(N_s - \frac{t_s}{t_b} N_b \right) \quad (\text{Eq. 2.4})$$

and N_s is net peak area of the photopeak in the sample spectrum, t_s is the live time of the standard spectrum collection (second), N_b is the corresponding net peak area in the background spectrum, t_b is the live time of the background spectrum collection (second), A is the activity of the calibration source radionuclide (Becquerel), p_γ is the emission probability of the gamma-ray corresponding to the peak energy, C_{D1} is the correction factor for the nuclide decay from the time the sample was collected to the start of the measurement, C_{D2} is the correction factor for the nuclide decay during counting period, C_{RS} is the correction factor for pulse loss due to random summing, C_{CS} is the coincidence summing correction factor for those nuclides decaying through a cascade of successive photon emissions and important for close source-to-detector distances, C_G is the correction factor due to a differences between standard source and measurements counting geometry and C_{SA} is the correction factor for self-attenuation in the standard.

Analysis of correction factors

There are two **correction factors due to radioactive decay**, C_{D1} , C_{D2} : the correction factor for the radioactive decay prior to the counting period and during the counting period (**Eq. 2.5** and **2.6**), respectively:

$$C_{D1} = e^{-\lambda_{diff} t} \quad (\text{Eq. 2.5})$$

and

$$C_{D2} = \frac{\lambda t_r}{1 - e^{-\lambda t_r}} \quad (\text{Eq. 2.6})$$

where t_{diff} is the decay time (real time) prior to the start of the count, t_r is the elapsed time (real time) of the count, $\lambda = \ln(2)/T_{1/2}$ is the radionuclide decay constant, and $T_{1/2}$ = the radionuclide half-life. For the point sources considered here (^{152}Eu and ^{56}Co) the correction coefficient is $C_{D2} \approx 1$.

The **random summing** correction factor (Eq. 2.7) is defined as the possibility of more than one photon to be absorbed by the detector during a pulse sampling cycle, the sum of the energies of two (or more) is recorded in the spectrum instead of two (or more) different signals. Any full-energy photon that is summed with another pulse is not recorded in the single photon peak and represents a loss of counts or efficiency. This loss is count rate dependent and is relevant for high count rates, while for low count rates this correction factor could be taken as $C_{RS} \approx 1$.

$$C_{RS} = e^{-2R\tau} \quad (\text{Eq. 2.7})$$

where τ is the time resolution of the measurement system.

The **coincidence-summing correction** factor C_{CS} (Eq. 2.8) for the specific gamma line (with energy E) emitted from a nuclide decaying in a cascade mode is defined as the ratio of the corresponding apparent photopeak efficiency $\varepsilon_p^{app}(E)$ to the full energy peak efficiency, $\varepsilon_p(E)$, at the same energy obtained from the energy curve (or Monte Carlo simulation) measured with single-photon emitting nuclides.

$$C_{CS} = \frac{\varepsilon_p^{app}(E)}{\varepsilon_p(E)} \quad (\text{Eq. 2.8})$$

Coincidence summing is due to the simultaneous detection of two or more gamma-rays occurring in cascade from the decay of an excited nucleus in which the lifetimes of intermediate levels are short relative to the integration time of the amplifier. If the nuclide has no cascade of gamma-rays than $C_{CS} = 1$. The C_{CS} depend on the nuclide decay scheme, on sample geometry and composition and on

detector features. The coincidence summing corrections becomes relevant for close source-to-detector configuration of the counting geometry, like in the case of MCA_Rad system.

The measured apparent absolute efficiency $\varepsilon_p^{app}(E)$ for ^{152}Eu and ^{56}Co source was corrected for coincidence summing using the mathematical formalism developed by [Semkow et al. 1990](#) and further simplified by [DeFelice et al. 2000](#) (Eq. 2.9a).

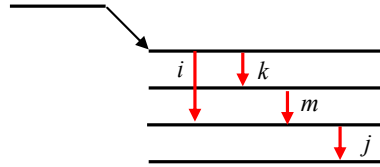


Figure 2.7: simplified decay scheme showing the effect of summing in and out.

Considering a simple decay scheme ([Fig. 2.7](#)) the coincidence summing of $\gamma-\gamma$ and $\gamma-KX$ (normally only KX-rays have sufficient energy to be observed by a HPGe detector) can be reconstructed as:

$$C_{CS(i)} = \left[1 - \frac{\sum_j P_{ij} P_i P_j \varepsilon_j}{I_{\gamma_i}} \right] \left[1 + \frac{\sum_{k,m} P_{tkm} P_k P_m \varepsilon_k^{app} \varepsilon_m^{app}}{I_{\gamma_i} \varepsilon_i^{app}} \right] \quad (\text{Eq. 2.9a})$$

where P_{ij} is the probability of coincident transitions (i, j); P_i is the probability of photon emission in transition i ; I_{γ} is the photon emission probability; ε_i is the apparent full energy peak efficiency and ε_j is the total apparent efficiency.

The [equation 2.9a](#) can be simplified in function of photopeak apparent and total efficiencies:

$$C_{CS(i)} = \left[1 - \sum_j C_j \varepsilon_j \right] \left[1 + \sum_{k,m} C_{k,m} \frac{\varepsilon_k^{app} \varepsilon_m^{app}}{\varepsilon_i^{app}} \right] \quad (\text{Eq. 2.9b})$$

where C_j and $C_{k,m}$ can be calculated using the decay data (described later in [Appendix A](#)).

The gamma rays emission probability, P_{γ} , ([Eq. 2.10](#)) can be calculated as

$$P_\gamma = \frac{1}{1 + \alpha_i} \quad (\text{Eq. 2.10})$$

and transition probability of KX-rays, P_{KX} , (Eq. 2.11) emitted as a result of the internal conversion of the electron capture process can be calculated as

$$P_{KX(i)} = \frac{\omega_K \alpha_{KX(i)}}{1 + \alpha_{i(i)}} \quad (\text{Eq. 2.11})$$

where α_i is the total internal conversion coefficient; ω_K is the K-fluorescence yield for the daughter nuclide and $\alpha_{K(i)}$ is the K-conversion coefficient of transition i . For decay schemes with several transitions that decay by K-conversion, the total KX-ray emission probability is equal to the sum of the individual KX-ray emission probability of the transition.

The coincidence summing correction depend on the angular correlation between gamma rays averaged over the solid angle which for close source-to-detector distances is usually negligible, and therefore has been neglected in this treatment. When considering the angular correlation between two gamma rays the [equation 2.9](#) must be written as:

$$C_{CS(i)} = \left[1 - W_{ij} \frac{\sum_j P_{ij} P_i P_j \varepsilon_j}{I_{\gamma i}} \right] \left[1 + W_{km} \frac{\sum_{k,m} P_{tkm} P_k P_m \varepsilon_k \varepsilon_m}{I_{\gamma i} \varepsilon_i} \right] \quad (\text{Eq. 2.12})$$

where W is the angular correlation factor (Eq. 2.13) of two gamma rays. The angular correlation terms can be expanded as the Legendre series:

$$W(\theta) d\Omega = \sum_{i=1}^L A_{ij} P_{ij}(\cos \theta) d\Omega \quad (\text{Eq. 2.13})$$

where A_{ij} are catalogued for some standard radionuclides by IAEA (<http://www-nds.iaea.org/>)

In order to correct for summing, the total efficiency, $\varepsilon_t(E)$, was obtained by the empirical calculation of the peak-to-total ratio (P/T) (Cesana and Terrani 1989) and utilizing the relationship:

$$\frac{P}{T} = \frac{\varepsilon_p(E)}{\varepsilon_t(E)} \quad (\text{Eq. 2.14})$$

The empirical calculation was compared by experimental measurements (**Fig. 2.8**) of single and double gamma ray emitting points sources like ^{137}Cs , ^{60}Co , ^{40}K and ^{22}Na (**Debertin and Helmer 1988**). However, from the total efficiency curve it is shown that the value of total efficiency in the energetic range 200 - 3000 keV can be appropriately chosen as a constant (not in our study).

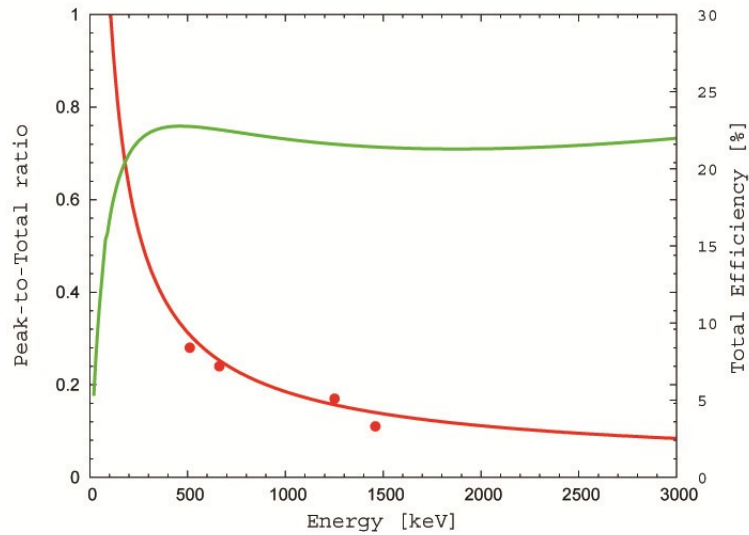


Figure 2.8: empirical calculation of P/T ratio curve (red) and experimental check by measuring single and double gamma ray emitting points sources like ^{137}Cs , ^{60}Co , ^{40}K and ^{22}Na . The related total efficiency curve (green).

The coefficients C_j and $C_{k,m}$ of **equation 2.9b** for ^{152}Eu are calculated (**Appendix A**) using the decay data catalogued and available by **Monographie BIMP 2005**, together with a bibliographic confrontation of similar studies. The coefficients for ^{56}Co were not calculated here, because of poor information of decay data, but directly taken from bibliographic studies. Finally, the absolute efficiency of the standard point source $\varepsilon_p(E)$ corresponding to standard energy lines is calculated by:

$$\varepsilon_p(E_i) = \varepsilon_p^{app}(E_i)C_{csc}(E_i) \quad (\text{Eq. 2.15})$$

where the results obtained from this calculation are listed in the **Table 2.3**.

The absolute efficiency of the standard point source $\varepsilon_p(E)$ in the energetic range from 200 to 3000 keV is obtained by fitting the function described by **Knoll 1999**, excluding the fourth term (**Fig. 2.9**):

$$\varepsilon(\%) = \left(b_0 \frac{E}{E_0} \right)^{b_1} + b_2 \exp\left(-b_3 \frac{E}{E_0} \right) + b_4 \exp\left(-b_5 \frac{E}{E_0} \right) \quad (\text{Eq. 2.16})$$

where E is the energy of gamma ray and E_0 is introduced to make the argument of the logarithm dimensionless and b_i are the fitting parameters (where $b_0 = 1.38$, $b_1 = 1.41$, $b_2 = 22.97$, $b_3 = 5.43$, $b_4 = 6.61$ and $b_5 = 0.44$).

Table 2.3: apparent efficiency and corrected efficiencies for coincidence summing according to [equation 2.15](#).

Isotope	E (keV)	I (%)	C_{CS}	ε^{app} [%]	$corr(\varepsilon^{app})$ [%]
^{152}Eu	121.8	28.41 (13)	1.2773	12.98 (20)	16.58 (25)
	244.7	7.55 (4)	1.2979	9.21 (14)	11.95 (18)
	344.3	26.59 (12)	1.1633	8.14 (12)	9.47 (14)
	778.9	12.97 (6)	1.0552	4.21 (6)	4.45 (7)
	964.1	14.50 (6)	1.0977	3.78 (6)	4.14 (6)
	1112.1	13.41 (6)	1.0723	3.53 (5)	3.79 (6)
	1408.0	20.85 (8)	1.0613	2.93 (4)	3.11 (5)
$^{56}\text{Co}^*$	1771.4	15.45 (4)	1.2822	2.20 (4)	2.82 (6)
	2034.8	7.74 (1)	1.2721	1.95 (4)	2.47 (5)
	2598.5	16.96 (4)	1.1757	1.79 (4)	2.11 (4)
	3253.5	7.87 (3)	1.1641	1.44 (3)	1.68 (3)

* the efficiency for ^{56}Co was calculated normalizing the activity at 846 keV.

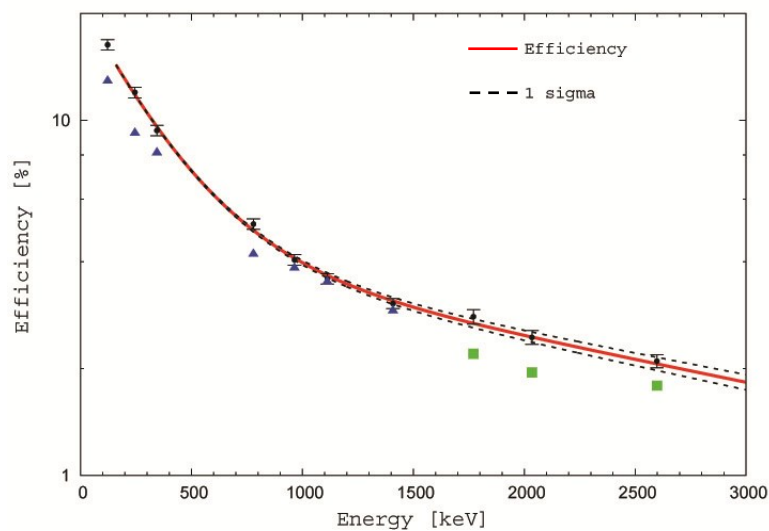


Figure 2.9: absolute efficiency curve for the MCA_Rad system obtained by fitting the corrected values for coincidence summing with [equation 2.16](#). Apparent efficiencies of ^{152}Eu (blue triangles) and ^{56}Co (green squares) are also presented.

The **geometrical correction factor** C_G is defined as the ratio of the full energy peak efficiency $\varepsilon_p(E)$ for a counting geometry and the full energy peak efficiency $\varepsilon_p^{ref}(E)$ for reference geometry (point source, in our study).

$$C_G = \frac{\varepsilon_p^{ref}(E)}{\varepsilon_p(E)} \quad (\text{Eq. 2.17})$$

Evidently, if the geometry of both the calibration and the measured sample is the same, then $C_G = 1$. In our case there is a difference due to calibration standard point source and cylindrical shape counting geometries (75 mm x 45 mm), therefore, because of the difference between the standard point source a geometrical correction is done using an empirical approach. The effect of volume geometry can be described in terms of the effective solid angle developed analytically by **Moens et al. 1981** within less than 2% of uncertainty between numerical and experimental calculations. The geometrical factor for MCA_Rad system is deduced from a set of measurements using ^{56}Co and ^{57}Co point sources placed at different radial distances from the detector axis on three different planes (**Fig. 2.10**).

$$C_G(E_i) = \frac{\bar{\Omega}_x}{\Omega_{ref}} \approx \frac{\sum_{j=1}^N \frac{[R_x(E_i)]_j}{N}}{R_{ref}(E_i)} \quad (\text{Eq. 2.18})$$

where $R_x(E_i)$ is the net count rate in the standard spectrum collected in different positions (j) and $R_{ref}(E_i)$ is the net count rate in the standard spectrum collected in the reference positions (center).

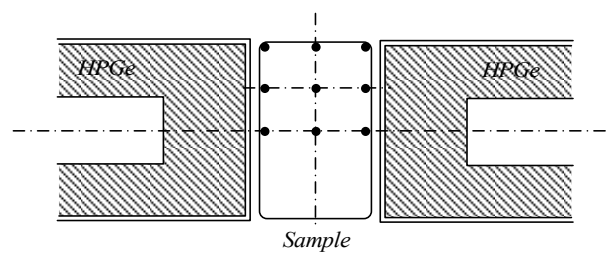


Figure 2.10: measurement configuration of the experimental measurement done for the calculation of geometrical correction factor.

The geometrical correction factor was then fitted as a function of energy and considered independently in order correct the efficiency curve of the standard point source (**Fig. 2.11**).

$$C_G(E) = \sum_{i=0}^n a_i \left(\frac{E}{E_0} \right)^i \quad (\text{Eq. 2.19})$$

where $n = 4$ and a_i are the fitting coefficients ($a_1 = 0.8678$, $a_2 = 0.1098$, $a_3 = -0.0541$, $a_4 = 0.0077$).

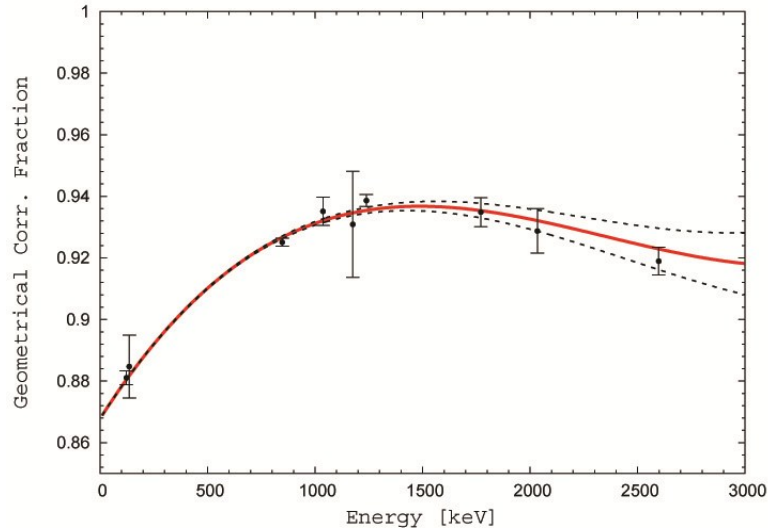


Figure 2.11: curve reconstructing the geometrical correction factor obtained by fitting photopeaks of ^{56}Co and ^{57}Co with a third order polynomial (Eq. 2.19).

The **self attenuation correction factor**, C_{SA} , (Eq. 2.20) is defined as the ratio of the full energy peak efficiency $\varepsilon_p(\mu_i, E_i)$ for a sample with the linear attenuation coefficient μ and the full energy peak efficiency $\varepsilon_p(\mu_i^{ref}, E_i)$ for a sample with linear attenuation μ^{ref} .

$$C_{SA}(E_i) = \frac{\varepsilon(\mu_i^{ref}, E_i)}{\varepsilon(\mu_i, E_i)} \quad (\text{Eq. 2.20})$$

Evidently, if the matrix of both the calibration and the measured sample is the same, then $C_{SA} = 1$. In our case we are using standard point sources for absolute efficiency calibration (approximately air matrix composition) while the measurement sample test have different composition, therefore, need for correction. The self-absorption correction factor was calculated following a simple approach discussed by [Bolivar et al. 1997](#) and [Cutshall et al. 1983](#):

$$C_{SA} = \frac{1 - e^{-(\mu_s \rho_s - \mu_{ref} \rho_{ref})t}}{(\mu_s \rho_s - \mu_{ref} \rho_{ref})t} \quad (\text{Eq. 2.21})$$

where μ_s , μ_{ref} are the densities of test sample and reference material, ρ_s , ρ_{ref} are the densities of sample and reference material and t is the sample thickness. This approach is valid under the assumption made is that the photon emitters are uniformly distributed within the source of thickness t and that the photon paths were parallel to each other and perpendicular to the disk bottom surface. The **equation 2.21** can be expanded for $\mu_s \rho_s - \mu_{ref} \rho_{ref} \ll 1$ to:

$$C_{SA}(E_i) = A(E_i)e^{-B(E_i)\rho_s} \quad (\text{Eq. 2.22})$$

where $A(E_i) = e^{\mu_{ref} \rho_{ref} \frac{t}{2}} = 1 + a_1 E^{-a_2}$ and $B(E_i) = \mu_s (t/2) = b_1 E^{-b_2}$. Since we are using a standard point source (air matrix) the function $A(E_i) \approx 1$. In order to calculate the $B(E_i)$ function the mass attenuation coefficient is required. The mass attenuation coefficient is strongly Z dependent in the energy window below few hundred keV while for higher energies the trend is smoother and it depends mainly on energy. Since MCA_Rad efficiency calibration procedure is specifically designed for investigating of gamma emitters having energies higher than hundred keV. We can parameterize the mass attenuation coefficient as a function of energy (calculated using XCOM 3.1 database available on-line developed by Nuclear Institute of Standards and Technology (NIST)) for various rocks forming minerals by fitting their average mass attenuation coefficient (**Fig. 2.12**) deduced with a standard deviation of less than 2% in the energetic range 200 – 3000 keV.

$$\frac{\mu}{\rho}(E) = 0.5429 - 0.1081 \ln(E/E_0) + 0.0056 \ln(E/E_0)^2 \quad (\text{Eq. 2.23})$$

where $E_0 = 1$ keV are arbitrary coefficients chosen to make dimensionless the logarithm argument.

The self attenuation correction factor was then given as a function of energy and considered independently in order correct the efficiency curve of the standard point source.

$$C_{SA}(E, \rho_s) = \exp[(1.2609 - 0.2547 \ln(E) + 0.0134 \ln(E)^2) \rho_s] \quad (\text{Eq. 2.24})$$

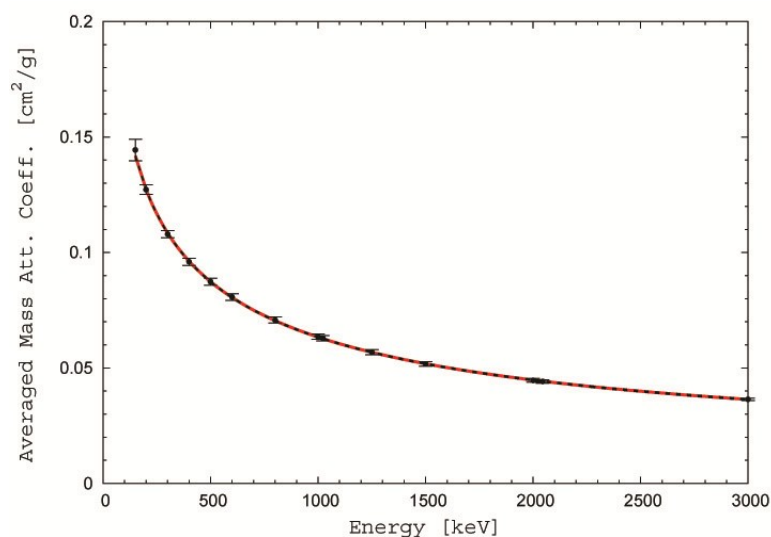


Figure 2.12: average mass attenuation coefficient deduced from weighting different rock forming minerals (calcite (CaCO_3); quartz (SiO_2); dolomite ($\text{CaMg}(\text{CO}_3)_2$); feldspar albite ($\text{NaAlSi}_3\text{O}_8$); feldspar anorthite ($\text{CaAl}_2\text{Si}_2\text{O}_8$); feldspar orthoclase (KAlSi_3O_8); anhydrite (CaSO_4); gypsum ($\text{CaSO}_4 \cdot 2\text{H}_2\text{O}$); muscovite ($\text{KA}_2(\text{Si}_3)\text{O}_{10}(\text{OH},\text{F})_2$); rutile (TiO_2); bauxite gibbsite ($\text{Al}(\text{OH})_3$).

Efficiency calibration cross-check using certified reference materials

The standard efficiency calibration method and the correction factors used are verified through a cross-check measurement using reference materials. Therefore three IAEA reference materials (certified within 95% confidence level (2σ)) in powder matrix (240 mesh) containing uranium ore RGU-1 (4940 ± 30 Bq/kg), thorium ore RGTTh-1 (3250 ± 90 Bq/kg) in secular equilibrium and K_2SO_4 element RGK-1 (14000 ± 400 Bq/kg) are used. The reference materials were transferred in the counting geometries and hermetically sealed and left undisturbed for 3 weeks in order to establish radioactive equilibrium in ^{226}Ra decay chain segment. In **Table 2.4** we report the measured activities for the main energetic lines used to study the ^{238}U and ^{232}Th decay chains and for ^{40}K . As we described in the calibration procedure the corrections due to differences in counting geometry C_G and self-absorption in test sample matrix, C_{SA} , were taken as independent correction functions. However, when measuring natural isotopes it is important to calculate the coincidence summing effect C_{CS}^* since most of the natural gamma ray emitting isotopes decay in relative complex schemes and possibly undergo in coincidence summing. The coincidence summing correction factors for the most important gamma rays of natural radioelements used for the estimation of their activity concentration were calculated using the same mathematical formalism described above and reported in **Appendix A**. Finally the activity concentration is estimated using the following equation:

$$A = \frac{R}{\varepsilon p_{\gamma} m} C_{SA} C_G C_{CS}^* \quad (\text{Eq. 2.25})$$

Table 2.4: activity concentrations calculated for the main energetic lines used to study the ^{238}U and ^{232}Th decay chains and for ^{40}K and the respective statistical uncertainty. An evaluation of efficiency calibration method uncertainty budget is described in details below.

Parent Isotope	Daughter Isotope	E (keV)	I (%)	C_{CS}	C_{SA}	Activity (Bq/kg)
^{238}U	^{234m}Pa	1001.0	0.837	1.0002	1.24	4875 ± 48
	^{214}Bi	609.3	44.8	1.1904	1.32	4872 ± 4
	^{214}Bi	1764.5	15.36	-	1.18	-
	^{214}Bi	1120.2	14.80	1.1902	1.23	5074 ± 8
	^{214}Bi	1238.1	5.86	1.1817	1.22	4932 ± 15
	^{214}Pb	351.9	35.8	1.0015	1.42	4773 ± 3
	^{214}Pb	295.2	18.5	1.0000	1.46	4826 ± 5
^{232}Th	^{228}Ac	911.2	26.6	1.0236	1.24	3092 ± 4
	^{228}Ac	969.0	16.2	1.0120	1.23	3086 ± 6
	^{228}Ac	338.3	11.3	1.0339	1.40	3059 ± 5
	^{212}Pb	238.6	43.3	0.9904	1.48	3246 ± 2
	^{212}Bi	727.3	6.58	1.0556	1.27	3389 ± 9
	^{208}Tl	2614.5	99.0	-	1.13	-
	^{208}Tl	583.2	84.5	1.2982	1.31	3342 ± 4
^{40}K	-	1460.8	11.0	-	1.21	14274 ± 71

NOTE: IAEA-RGU-1 and IAEA-RGTh-1 are measured for 24h counting time while IAEA-RGK-1 is measured for one hour counting time.

Uncertainty budget evaluation for efficiency calibration

Here are summarized the typical uncertainties evaluated for the efficiency calibration method. The combined standard uncertainty of the quantity of interest, y , it is derived by applying the error propagation law of Gauss. Thus, for uncorrelated quantities (independent) the combined standard uncertainty of y , $u_c(y)$, is calculated in terms of component uncertainties, $u(x_i)$, as follows (ISO/IEC Guide 98:1993):

$$u_c[y(x_1, x_2, \dots, x_n)] = \sqrt{\sum_{i=1}^n \left(\frac{\partial y}{\partial x_i} \right)^2 [u(x_i)]^2} \quad (\text{Eq. 2.26})$$

The expanded uncertainty is then given by $u(y) = ku_c(y)$ where k is the coverage factor (confidence interval). In **table 2.5** are summarized the main sources of uncertainty in efficiency calibration procedure.

Table 2.5: uncertainty budgeted evaluation for efficiency calibration method.

Description	Quantity ± unc.	Relative unc. [%]	Combined rel. unc. [%]
Certified standard source (¹⁵² Eu) activity in Bq/kg	6566 (99)*	1.5	-
Radionuclide (¹⁵² Eu) half-live in years	13.537 (6)	< 0.1	-
Emission probability of gamma-ray energy	-	< 0.6	-
Statistical uncertainty	-	-	< 0.5
Efficiency fitting uncertainty (with C _{CS} correction)			
200 - 1800 keV	-	-	< 2.9
1800 - 3000 keV	-	-	< 4.8
Geometrical correction fitting uncertainty			
200 - 1800 keV	-	-	< 0.3
1800 - 3000 keV	-	-	< 1.1
Self-absorption correction uncertainty			
200 - 1800 keV	-	-	< 0.5
1800 - 3000 keV	-	-	< 0.7

* certified expanded uncertainty (95% confidence level).

2.3 Case of study: bedrock radioelement mapping of Tuscany Region, Italy

The Northern Apennines are a fold-thrust belt originated during the Tertiary by the collision between the Apulia (or Adriatic) microplate related to the African plate, and the Briançonnais microplate

(Sardinia-Corsica massif), related to the European plate ([Boccaletti et al 1971](#); [Scandone 1979](#); [Stampfli et al 1991, 2001](#)).

The geological base map used for the development of the analysis of natural radioactivity, is the geological map of Tuscany at scale 1:250,000, realized by the Centre for Geotechnologies (University of Siena) with the collaboration of the Tuscany Region ([Fig. 2.13](#)). Compiling the Geological Map of Tuscany at a scale of 1:250,000, was a first and preliminary attempt to create a document which unifies and synthesise the information from the small-scale maps (that is the Carta Geologica Regionale, 1:10,000 scale) and from the “CARG Project” of the Italian Geological Surveying. The evolving knowledge regarding Tuscany and its geology, and the Northern Apennines in general, can be seen in the several versions of geological maps, and their related observations, from the twentieth century. The history of the extraordinary development of these maps actually begins in the mid-1800s, as geological investigations assumed great importance due to the exploration and utilization of natural resources. In 1867, the Royal Geological Committee of Italy (Regio Comitato Geologico d'Italia), was instituted in an initiative similar to that occurring in other European countries (beginning with France). The Geological Office, the executive organ, was created within the Committee. Tuscany, with its significant mineral sector, was the subject of an intensive research program. The 1:10,000 maps used for the compilation of the Geological Map of Tuscany exist for approximately 60% of the region. Not all areas were actually surveyed: the most recent published geological maps (1:25,000 and 1:10,000 scales) and Geological Map of Italy sheets (1:100,000) were utilized for the final map. The map is provisional and it is based on documents from diverse scientific frameworks.

The Legend for the Geological Map of Tuscany has been organized into: a) Tectonic Units originating from different palaeographic domains, which were deformed and emplaced during the Tertiary collisional phase (Early Miocene) related to the Apennines Orogeny, after the Ligurian Ocean closure (Paleocene-Eocene); b) sediments deposited after the main Tertiary tectonic phases. Each tectonic unit corresponds either to a single domain, or to part of a domain. The domains are based on the palaeogeography of the Apulian southern margin, and the adjacent Ligurian ocean domain, in the Cretaceous. Some tectonic units have been grouped together if the following conditions were met: they are of minor extent, they originate from the same palaeogeographical domain, and they are separated by relatively minor overthrusts on the original maps. A palinspastic reconstruction, oriented W-E in present day coordinates, evidences the following domains (the tectonic units with minor extension, incorporated within the domains, are shown in parentheses):

- Ligurian Domain: we retain the classical subdivision of an internal Ligurian Zone, which is characterized by a deep sea succession deposited on oceanic crust (Ophiolitic Unit, or Gottero Unit); an external Ligurian Zone characterized by several Helminthoid Flysch and their related "basal complexes" which were likely deposited upon oceanic crust, or mantle, near the continental margin (Helminthoid Flysch Unit, Antola Unit, Caio Unit, Ottone Unit, Monteverdi M.mo Unit, Montaione Unit, Morello Unit, S. Fiora Unit, Cassio Unit, etc.);
- Subligurian Domain (Limestone and Clay Unit, Canetolo Unit);
- Tuscan Domain; we distinguish a succession exhibiting little or no metamorphism (Tuscan Nappe) , and a succession with green schist facies metamorphism ("Apuan Autochthon," Massa Unit, S. Maria del Giudice Unit and M. Serra Unit, Monticiano-Roccastrada Unit);
- Umbrian-Marches Domain (limited outcrops of the Marnoso-Arenacea fm. and overlaying marls);

Separate tectonic units have been maintained for the "Successioni incertae sedis (Uncertain position successions)" and the "Successione oceanica con metamorfismo di alta pressione (Oceanic successions with high pressure metamorphism) ." The first mentioned unit essentially comprises the "Pseudoverrucano" succession, which outcrops in southern Tuscany. Its palaeographic context remains equivocal, and therefore it is considered as a singular unit. The second has been maintained as a distinct tectonic unit: it comprises lithotypes of varying provenance (from the Ligurian and also possibly the Tuscan successions), incorporated into tectonic *mélange* and shear zones, that experienced high pressure metamorphism related to the Tertiary collisional phases of the Northern Apennines (Cala Piatti Unit, Cala Grande Unit, M. Argentario, Gorgonia Metamorphic Units, etc.). Other sedimentary successions are distinguished in the legend. These successions, on the Tyrrhenian side of the Northern Apennines, have been deposited on the tectonic units, unconformably, after the tectonic unit was emplaced. The successions are separated by regional unconformities. From top to bottom they are:

- Pliocene to Quaternary, continental and coastal deposits;
- Pliocene to Quaternary marine deposits;
- Messinian lacustrine and lagoonal, evaporitic and pre-evaporitic, deposit;
- Messinian pre-evaporitic, marine deposits;
- EarlyTurolian lacustrine deposits;
- Epiligurian Deposits;

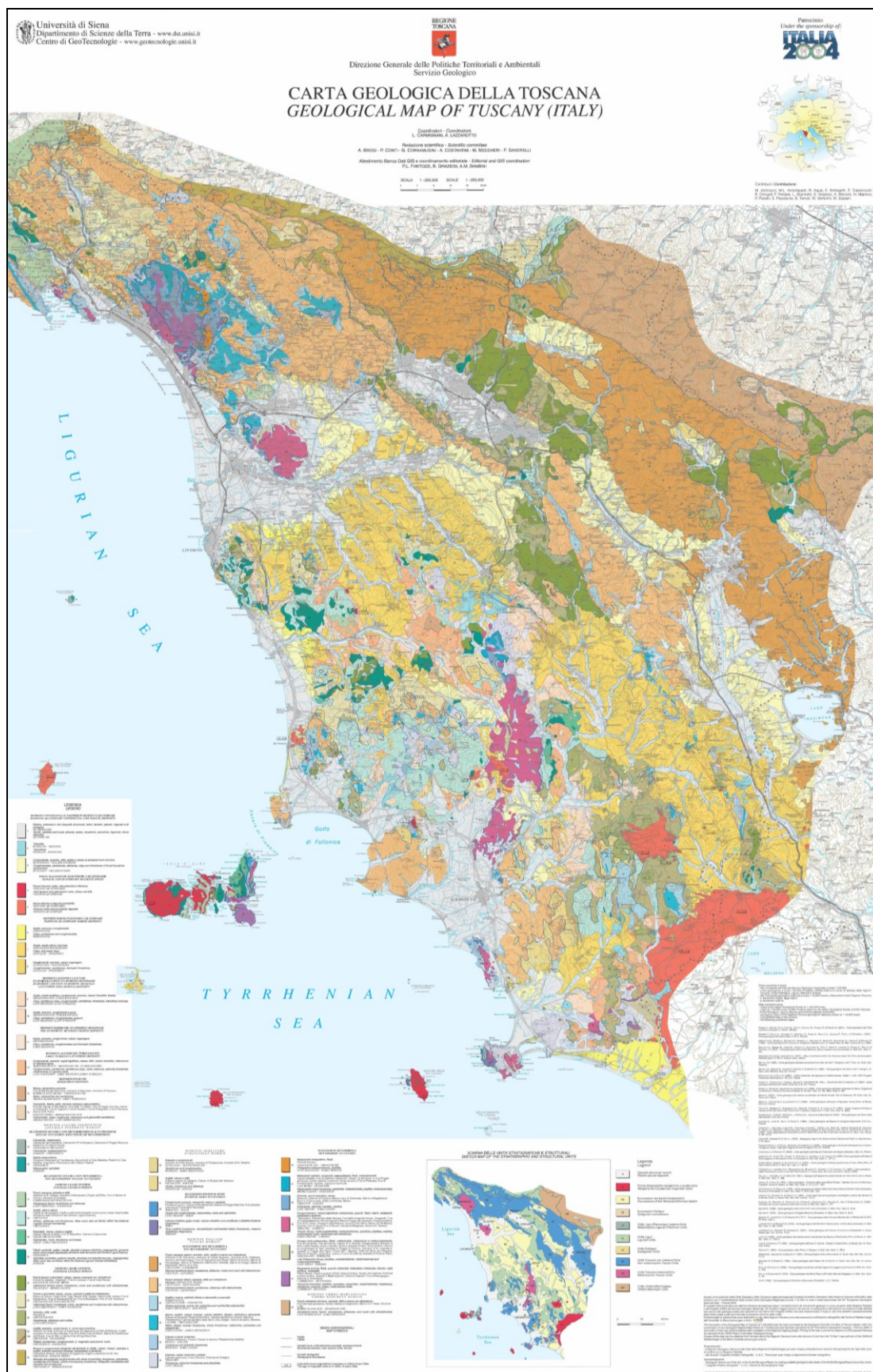


Figure 2.13: the geological map of Tuscany at scale 1:250,000.

Finally, some lithostratigraphic units have been grouped together, for ease of presentation at map scale as the magmatic intrusive and sub-volcanic rocks, effusive and pyroclastic rocks linked to Neogene magmatism, and the Quaternary cover (**Fig. 2.13**). The Legend of the Geological Map of Tuscany consists of 42 additional partitions formed by groups of formations, divided by age and, in some cases, by the composition:

Pliocene-Quaternary continental and coastal deposits

1-al) Sands, pebbles and muds (alluvial, eolian, lacustrine, palustrine, lagoonal, shore deposits), Quaternary.

2-tr) Travertines, Pliocene-Holocene.

3-VIL) Conglomerates, sandstones, siltstones, clays and limestones of fluvial-lacustrine environment, Ruscinian-Villafranchian.

Neogene and Quaternary magmatic rocks

4-gamma) Acid igneous and subvolcanic rocks, dykes and sills, Neogene-Quaternary.

5-alfa) Volcanic rocks and pyroclastic deposits, Neogene-Quaternary.

Pliocene-Quaternary marine deposits

6-PLQ) Clays, sandstone and conglomerates, Pleistocene.

7-PLIa) Clays, silty-marly clays, Zanclean-Piacenzian.

8-PLIs) Conglomerates, sandstones, bioclastic limestones, Zanclean-Piacenzian.

Evaporitic and Post-Evaporitic Messinian lacustrine and lagoonal deposits

9-MESp) Clays, lignitiferous clays, conglomerates, sandstones, limestones, travertines, breccias; Late Messinian (Late Turolian).

10-MESg) Clays, sandstones, conglomerates, gypsum; Late Messinian (Late Turolian).

Pre-Evaporitic Messinian marine deposits

11-MESa) Clays, sandstones, conglomerates and bioclastic limestone.

Early Turolian lacustrine deposits

12-FOS) Conglomerates, sandstones, lignitiferous clays, marls, siltstones, dolomitic limestones, olistostrome of Ligurian rocks; Late Tortonian-Early Messinian (Early Turolian).

Epiligurian deposits

13-MAN) Marls, calcarenites and sandstones; Middle Burdigalian-Early Tortonian.

14-MFU) Calcarenites, marls, mudstones, calcareous and glauconitic sandstones; Middle Eocene-Late Serravalian.

Ligurian-Piedmont Domain

Oceanic succession affected by hp metamorphism

15-SCI) Calcschists, metasandstones; Jurassic-Cretaceous.

16-OPR) Metamorphic ophiolites; Jurassic.

Non metamorphic oceanic succession

Internal Ligurian Domain

17-GOT) Arenaceous flysch: sandstones and siltstones; Late Campanian-Paleocene.

18-APA) Shales, siltstones and limestones (they occur also as blocks within the External Ligurian Domain formations); Cretaceous.

19-CCL) Radiolarites, marls, limestones and shales; Malm-Early Cretaceous.

20-OFI/OFIa) Ophiolites: peridotites, gabbros, basalts, ophicalcites and ophiolitic breccias, plagiogranites (they occur also as blocks within the External Ligurian Domain formations); Jurassic.

External Ligurian Domain

21-MOR) Helminthoid, tertiary flysch: limestones, marls and sandstones with olistostromes; Paleocene-Middle Eocene.

22-ELM) Helminthoid flysch: limestones, marls, sandstones and mudstones with olistostromes; Late Cretaceous-Early Paleocene.

23-PTF) Sandstones siltstones and rudites; Late Cretaceous.

24-AVA/a-beta) Shales, sandstones, conglomerates and magmatic subvolcanic rocks; Cretaceous-Paleocene.

25-BAS) Breccias and polygenic conglomerates with clasts of ophiolites, limestones, radiolarites, sandstones and shales, quartz-mica bearing sandstones, feldspathic sandstones and ophiolite-rich sandstones; Cretaceous-Middle Eocene.

Subligurian Domain

26-ARE) Sandstones and conglomerates; Rupelian-Early Aquitanian.

27-ACC) Shales, limestones and siltstones; Paleocene-Eocene.

Incertae sedis Successions

28-PSE) Quartz-rich conglomerates, calcarenites, marls and calcilutites; Late Triassic-Malm.

29-CCR) Gray-reddish limestones, recrystallized well-bedded black limestones, massive dolostones (Argentario); Triassic.

Tuscan Domain

Non Metamorphic Succession

30-CEV) External sandstone flysch: sandstones, siltstones, shales and marls with olistostromes; Chattian-Langhian.

31-MAC) Internal sandstone flysch: sandstones, siltstones with olistostromes; Chattian-Aquitanian.

32-STO) Shales and marls, quartz-rich calcilutites and nummulites calcarenites; Early Cretaceous-Oligocene.

33-SEL) Marls, shales, nodular limestones, cherty limestones, radiolarites, calcilutites and calcarenites; Early Liassic-Early Cretaceous.

34-MAS) Limestones and dolomitic limestones; Rhaetian-Early Liassic.

35-CAV) Dolostones, dolomitic limestones and anhydrites; Late Triassic.

Metamorphic Succession

36-PMG) Feldspathic metasandstones, phyllites; Late Oligocene-Early Miocene.

37-CSC) Metamorphic cherty limestones, calcschists, metaradiolarites, phyllites, metacalcarenites; Middle Liassic-Oligocene.

38-CAR) Dolostones, dolomitic marbles, marbles; Late Triassic-Early Liassic.

39-VER) Triassic Group: metaconglomerates, metasandstones, quartzites, phyllites, marbles, metavolcanic rocks, calcschists and dolostones; Early Triassic-Carnian.

40-PAL) Late Palaeozoic Group: phyllites, metasandstones, metalimestones and metaconglomerates; Late Viséan-Permian.

41-ERC) Hercynian basement: phyllites, quartzites, calcschists, metalimestones, metarkoses, dolostones, graphitic shales, metavolcanic rocks. Cambrian?-Devonian.

Umbro-Marchean Domain

42-FMA) Sandstone-marly flysch: sandstones, siltstones and marls with olistostromes; Late Burdigalian-Early Messinian.

2.3.1 Representative sampling and sample preparation strategy for bedrock radioelement mapping

The sampling strategy adopted for contamination studies like radioactive fallout or other contaminants is based on the choice of a regular homogeneous grid (**Fig. 2.14 a, b**) over the area under investigation. Sometimes forced by the physical conditions of the surveyed area the sampling strategy may be completely random (**Fig. 2.14 c**). This choice is based on the consideration that the contamination may have a random distribution since doesn't have any relationship with base ground information.

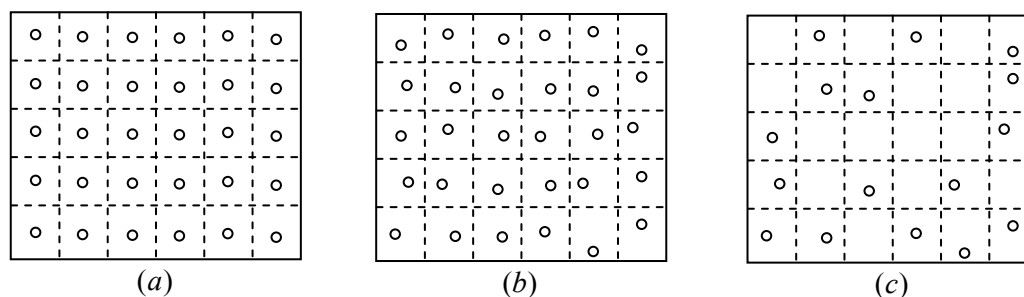


Figure 2.14: (a) aligned homogeneous grid, (b) unaligned homogeneous grid, and (c) random sampling strategies.

When dealing with natural radioelements, constituent part of the environment where we live, the sampling strategy can be done weighting the base ground information (geologically grided area). The sampling strategy was planned on geological basis characterizing them about their radioactivity content: the geological homogeneous units are recognized by low density of samples (also, because of the radioactivity concentration homogeneity), permitting to focus a high density of samples on the heterogeneous areas. Excluding the quaternary deposits when one sample per 25 km² was collected (**Fig. 2.15**).

A total of 882 samples (prevalently rocks) were collected and distributed as shown in **figure 2.15**, having an average superficial distribution of one sample per about 12 km². Samples were crushed, sieved (homogenized in less than 2 mm fine grain size) and then placed in a drying oven at temperature 60°C in order to remove the moisture. The dried bulk sample is then transferred in 200cc cylindrical polycarbonate containers, weighted and labeled with a barcode. Finally, the accurately sealed containers were stored for at least 38 days in order to reach the radioactive secular equilibrium between ²²²Rn and ²²⁶Ra, prior to be measured using high-resolution gamma-ray spectrometry MCA_Rad system following international standards of analysis (**ASTM C1402-04 2009** and **UNI 10797 1999**).

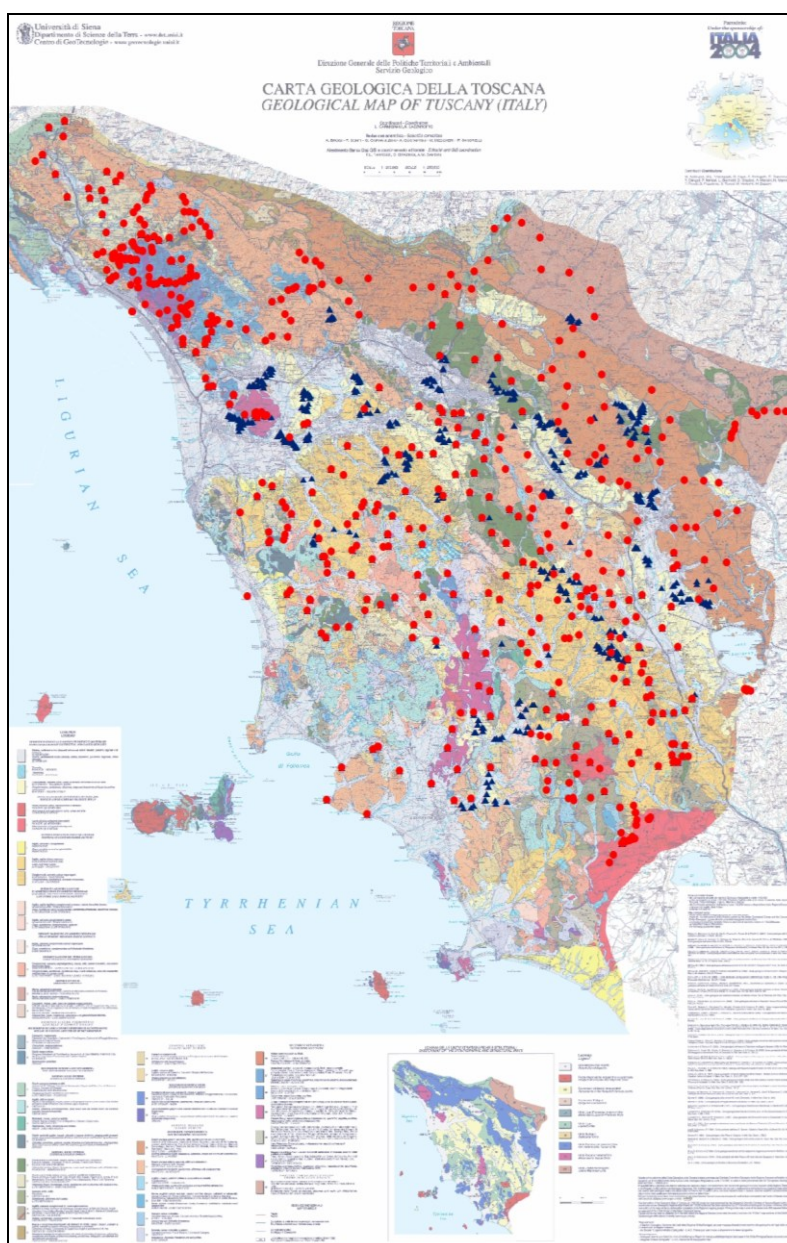


Figure 2.15: the spatial distribution of 882 samples (blue triangle soil and red circle rocks samples) collected over the territory of Tuscany Region for the realization of potential natural radioactivity concentration of bedrocks.

2.3.2 Summary of the results: bedrock radioelement mapping

High-resolution gamma-ray spectrometry measurement and spectrum analysis

As we described above, the MCA_Rad system was designed to deal with a high number of measurements, by availing to its elevated efficiency. In [Table 2.6](#) are shown the typical statistical uncertainties achieved for one hour screening measurement and using the [equation 2.25](#) over 882

samples (soil and rock). It can be shown that for typical crustal concentrations of potassium, uranium and thorium the statistical uncertainty, for one hour acquisition live time, is ranged between 5 to 10%, completely acceptable for environmental radioactivity measurements.

Table 2.6: typical statistical uncertainty for activity concentration ranges for 1h of acquisition time. The evaluation was done for 609 keV (^{214}Bi), 583 keV (^{208}Tl) considering secular equilibrium and 1460 keV (^{40}K).

Statistical unc. (%)	^{40}K (Bq/kg)	^{238}U (Bq/kg)	^{232}Th (Bq/kg)
10	60	20	30
5	220	50	70
1	4400	440	450

The activity concentration was calculated using the [equation 2.25](#) and as a good practice was reported the statistical uncertainty and checked over with the MDA calculated according to the [equation 2.2](#) with some modifications regarding the presence of a bulk mass of test sample:

$$MDA = \frac{L_D}{\varepsilon I_\gamma t m} \quad (\text{Eq. 2.27})$$

where here the L_D is calculated for the test sample, ε is the efficiency, I_γ is the gamma line intensity, t is the acquisition live time and m is the mass of the sample.

In [table 2.7](#) are summarized the results obtained from MCA_Rad system for the characterization of 42 geological formational domains. The total activity (A) in Bq/kg is calculated summing the activity concentration of the single radioelement and the uncertainty was propagated using the propagation laws ([ISO/IEC Guide 98:1993](#)). Furthermore, for radiation protection purposes the absorbed dose rate from external gamma radiation was calculated as discussed in [section 1.2.1](#).

Table 2.7: radioactivity characterization for 42 geological formation domains by MCA_Rad system for 1h acquisition time (1σ is the standard deviation) with (*) is reported the median value.

Sigla Carta	Area (km ²)	No. sample	K* (Bq/kg)	K \pm σ (Bq/kg)	U* (Bq/kg)	U \pm σ (Bq/kg)	Th* (Bq/kg)	Th \pm σ (Bq/kg)	A* (Bq/kg)	A \pm σ (Bq/kg)	D* (nGy/h)	D \pm σ (nGy/h)
1-al	4778	29	501	479 \pm 109	26	26 \pm 9	35	35 \pm 9	563	540 \pm 110	55	53 \pm 8
2-tr	122	15	26	44 \pm 45	65	51 \pm 44	4	5 \pm 4	96	101 \pm 63	34	29 \pm 21
3-VIL	1375	16	453	391 \pm 228	22	22 \pm 10	32	31 \pm 17	506	444 \pm 228	48	45 \pm 15
4-gamma	115	17	1511	1568 \pm 368	91	93 \pm 36	31	59 \pm 101	1633	1720 \pm 384	124	144 \pm 65
5-alfa	327	53	1761	1731 \pm 574	137	175 \pm 114	247	281 \pm 135	2145	2187 \pm 601	286	323 \pm 100
6-PLQ	80	62	525	519 \pm 154	27	27 \pm 7	33	32 \pm 9	585	578 \pm 154	54	54 \pm 9
7-PLIa	1666	63	522	511 \pm 165	27	27 \pm 8	33	32 \pm 10	581	570 \pm 166	54	53 \pm 10
8-PLIs	1217	25	468	408 \pm 198	29	30 \pm 15	29	27 \pm 13	525	465 \pm 199	50	47 \pm 13
9-MESp	407	26	60	179 \pm 208	25	39 \pm 37	9	14 \pm 14	94	232 \pm 211	20	34 \pm 21
10-MESg	143	10	281	274 \pm 212	16	20 \pm 12	19	20 \pm 11	316	314 \pm 212	31	33 \pm 12
11-MESa	74	2	246	246 \pm 217	17	17 \pm 4	16	16 \pm 10	278	278 \pm 217	28	28 \pm 11
12-FOS	357	1	172	172 \pm 8	36	36 \pm 2	19	19 \pm 2	228	228 \pm 9	36	36 \pm 1
13-MAN	26	2	246	246 \pm 217	17	17 \pm 4	16	16 \pm 10	278	278 \pm 217	28	28 \pm 11
14-MFU	4	2	246	246 \pm 217	17	17 \pm 4	16	16 \pm 10	278	278 \pm 217	28	28 \pm 11
15-SCI	9	2	435	435 \pm 240	22	22 \pm 19	32	32 \pm 26	488	488 \pm 242	47	47 \pm 21
16-OPR	2	10	20	36 \pm 33	3	3 \pm 1	1	2 \pm 1	25	41 \pm 33	3	4 \pm 2
17-GOT	115	4	970	792 \pm 404	32	33 \pm 19	43	43 \pm 19	1045	868 \pm 404	81	74 \pm 22
18-APA	872	4	194	226 \pm 181	12	13 \pm 9	18	18 \pm 12	224	256 \pm 182	24	26 \pm 11
19-CCL	52	9	230	231 \pm 168	8	14 \pm 19	11	21 \pm 34	249	266 \pm 173	20	29 \pm 24
20-OFIa+OFI	239	24	19	40 \pm 46	4	4 \pm 2	1	2 \pm 1	23	46 \pm 46	3	5 \pm 2
21-MOR	738	24	137	183 \pm 159	13	14 \pm 7	13	14 \pm 9	162	212 \pm 159	19	23 \pm 9
22-ELM	683	20	269	286 \pm 136	18	18 \pm 7	16	20 \pm 11	303	324 \pm 137	29	32 \pm 9
23-PTF	172	4	386	363 \pm 129	28	34 \pm 16	30	29 \pm 3	443	426 \pm 130	47	48 \pm 9
24-AVA/a-beta	1102	38	665	846 \pm 720	28	51 \pm 45	25	38 \pm 70	718	934 \pm 724	56	81 \pm 56
25-BAS	135	6	103	161 \pm 172	7	10 \pm 8	10	13 \pm 12	119	184 \pm 173	13	19 \pm 11
26-ARE	86	3	587	567 \pm 308	21	24 \pm 9	31	40 \pm 17	638	631 \pm 308	53	59 \pm 17
27-ACC	524	7	679	628 \pm 328	26	24 \pm 6	47	42 \pm 18	751	694 \pm 328	69	63 \pm 18
28-PSE	4	25	230	342 \pm 282	15	20 \pm 15	17	22 \pm 14	262	384 \pm 282	27	37 \pm 16
29-CCR	6	3	174	436 \pm 462	28	63 \pm 77	14	24 \pm 17	216	523 \pm 469	29	62 \pm 42
30-CEV	2331	57	702	688 \pm 174	36	36 \pm 9	46	45 \pm 11	784	768 \pm 174	74	72 \pm 11
31-MAC	2426	71	735	746 \pm 171	34	35 \pm 10	48	48 \pm 10	817	829 \pm 172	76	76 \pm 11
32-STO	394	23	310	430 \pm 322	12	14 \pm 8	17	27 \pm 18	338	470 \pm 322	29	41 \pm 18
33-SEL	238	34	108	198 \pm 234	9	11 \pm 11	7	13 \pm 20	124	222 \pm 235	13	21 \pm 16
34-MAS	139	18	23	38 \pm 50	10	11 \pm 7	3	4 \pm 2	36	52 \pm 50	7	9 \pm 4
35-CAV	365	11	56	71 \pm 49	8	12 \pm 10	5	5 \pm 3	69	88 \pm 50	9	12 \pm 5
36-PMG	25	6	807	806 \pm 177	42	42 \pm 8	51	52 \pm 15	900	900 \pm 178	84	84 \pm 12
37-CSC	76	38	207	292 \pm 273	9	14 \pm 13	10	20 \pm 25	226	325 \pm 275	19	30 \pm 20
38-CAR	154	40	17	37 \pm 102	5	10 \pm 9	3	4 \pm 7	26	51 \pm 103	5	9 \pm 8
39-VER	412	29	494	546 \pm 495	29	30 \pm 15	25	33 \pm 25	548	608 \pm 496	49	56 \pm 27
40-PAL	52	24	396	524 \pm 458	18	22 \pm 16	16	31 \pm 27	430	577 \pm 459	35	50 \pm 26
41-ERC	107	14	968	862 \pm 409	41	45 \pm 34	55	54 \pm 25	1064	961 \pm 411	93	89 \pm 27
42-FMA	748	11	522	478 \pm 147	30	35 \pm 15	32	29 \pm 9	584	542 \pm 148	55	54 \pm 11

The annual effective dose equivalent (AEDE) can be estimated considering the conversion coefficients from absorbed dose rate in air to effective dose received by an adult as 0.7 Sv/Gy (UNSCEAR 2000 and UNSCEAR 1993) taken for environmental exposure to gamma rays of moderate energy. The outdoor occupancy factor is taken equal to 0.2 (UNSCEAR 2000). The potential annual effective dose equivalent in outdoor ambient is given by the following equation (UNSCEAR 1988):

$$AEDE[\mu\text{Sv}/\text{y}] = D[n\text{Gy}/\text{h}] \times 10^{-3} \times 8760[\text{h}/\text{y}] \times 0.2 \times 0.7(\text{Sv}/\text{Gy})$$

In figure 2.16 the geological xxx are classified in the basis of the annual effective dose equivalent. According to Green et al. 1992 the world average annual effective dose equivalent is equal to 2.8 mSv/y with the external gamma-ray contribution of 15% (420 $\mu\text{Sv}/\text{y}$). From fig 2.16 it can be seen that the AEDE values for the geological formational domains are generally below this average value where 96.6% of the Tuscany Region territory is below 100 $\mu\text{Sv}/\text{y}$, with one particular case in which the AEDE value is slightly above ($390 \pm 120 \mu\text{Sv}$) characterizing only 1.4% of Tuscany Region area.

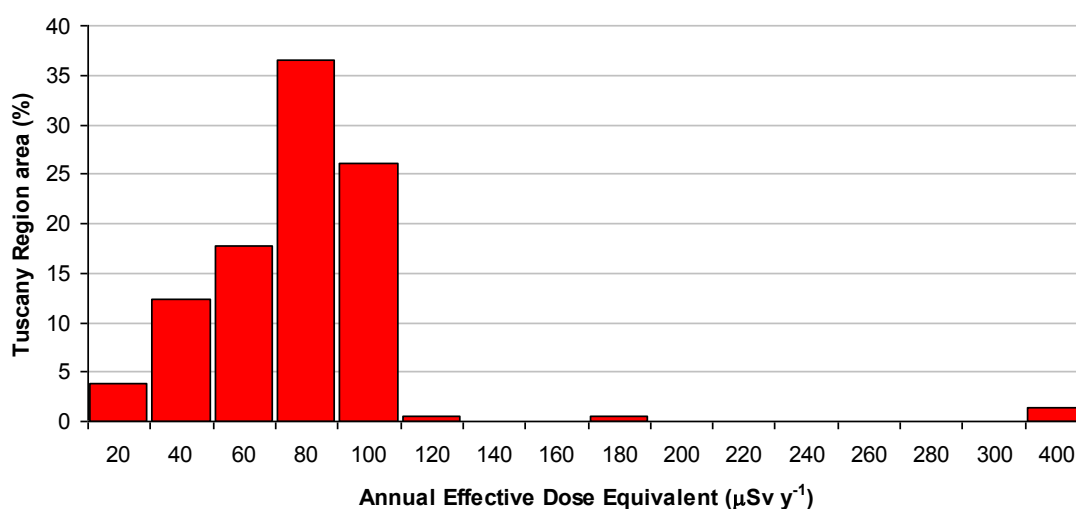


Figure 2.16: the potential annual effective dose equivalent weighted for the Tuscany Region area and calculated based on the characterisation of geological formational domains.

Radioelement mapping: geological reclassification based on radioelement concentration

The construction of the potential radioactivity concentration map of bedrocks is done by using the information obtained from the characterization of 42 geological formational domains. In figure 2.17 are represented the distribution in box-plot for the total activity concentration of the 42 geological formational domains having more than 10 samples. It is noticed from the distributions that the

geological information is an important parameter for characterizing the bedrock radioactivity concentration of natural elements. It can also be seen the different geological formational domains can be characterized within distinguishable distributions of total radioactivity (e.g. extremities with minimum 16-OPR, 20OFI/OFIa, 34-MAS, 38-CAR and maximum 4-gamma, 5-alfa and 24a-beta). However the median value characterizing a geological formational domain can be used to build-up different classes of radioactivity which width depend also on the distribution of the data.

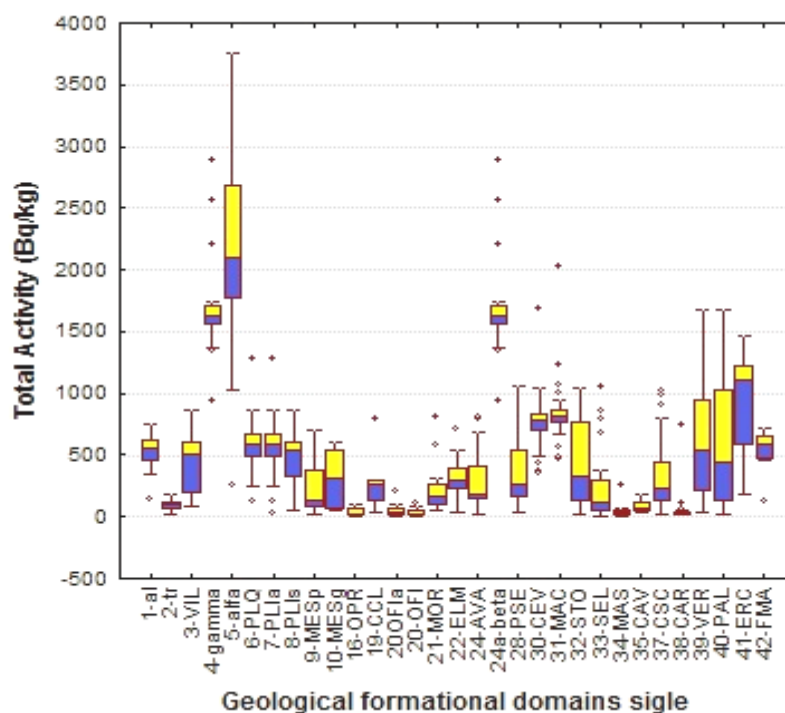


Figure 2.17: distribution of total activity (Bq/kg) in principal geological formations characterized with more than 10 samples. The box plot encloses 50% of the values while the whiskers include other 45% of them. The data exceeding this limits are the outliers and extremes.

The choice of classes of the total activity concentration was done by using the percentiles of the distribution of the total samples (**Fig. 2.18**) (as described in **Reimann 2005a** and **Reimann et al. 2005b**).

The percentile range was chosen large enough to take into account the distribution of total activity concentration for the most geological formational domains. Therefore, the total activity classes were taken equal to each percentile extremes. The extreme percentiles were chosen low enough in order to give a particular emphasize to these regions. The potential map of the total activity concentration was constructed from the reclassification of each geological formational domains according to their median values found to be within a specific percentile range. In **figure 2.19** is shown the total activity map and the percentile scale and the corresponding total activity concentration range.

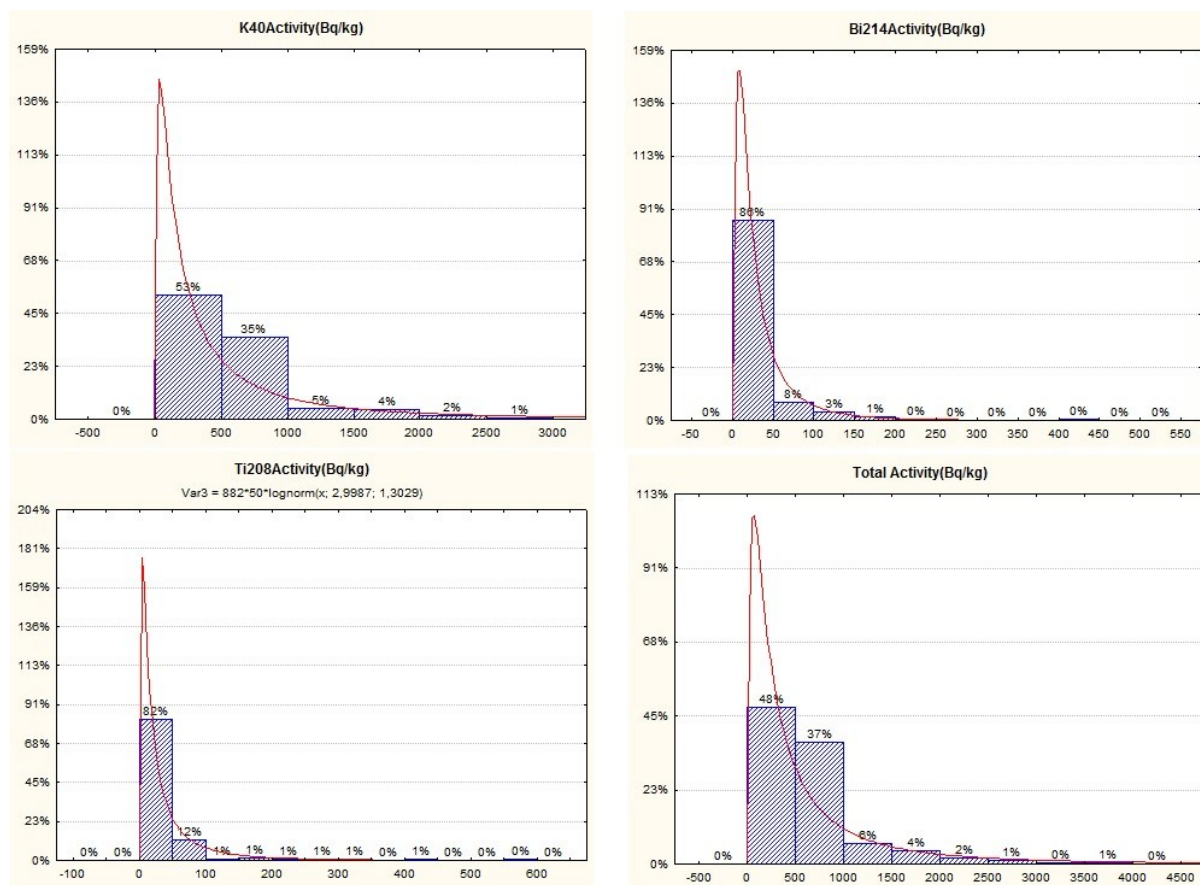


Figure 2.18: the distribution of potassium, uranium, thorium and the relative total activity concentration for 882 sample.

Map of natural radioactivity content in rocks of the Tuscany Region (Italy)

authors:

Bellotti Enrico, Bezzoni Giampaolo, Broggi Carlo, Buso Paolo, Caccioli Antonio, Calligaris Ivan, Carmignani Luigi, Colonna Tommaso, Di Carlo Giuseppe, Fantozzi Pierlorenzo, Fiorentini Giovanni, Guastaldi Enrico, Martovani Fabio, Mariani Sara, Massa Giovanni, Mei Liliana, Rossi Alvarez Carlos, Sisti Margola, Xivinha Gert.

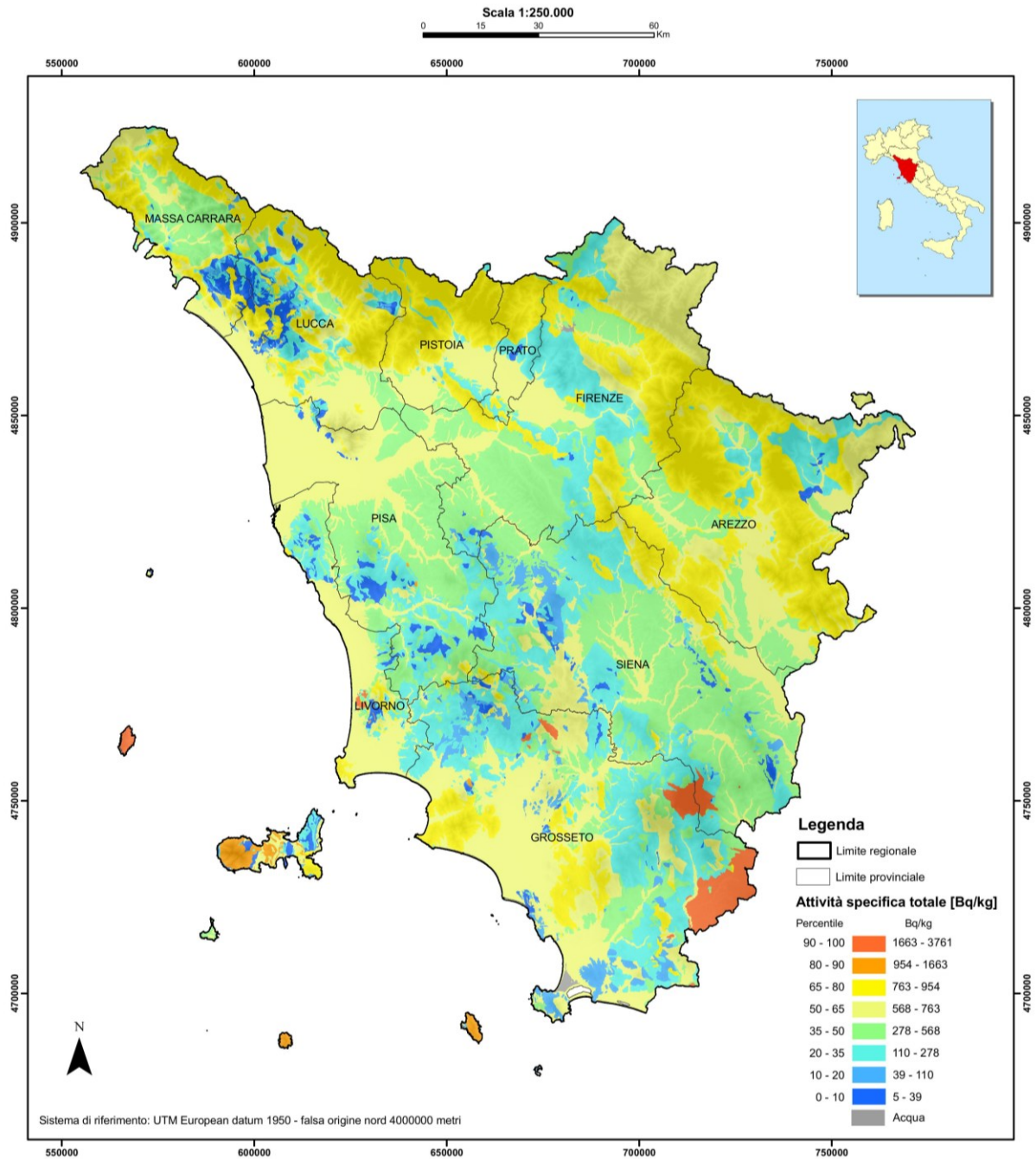


Figure 2.19: the potential total activity concentration of bedrocks in Tuscany Region realized through the utilization of 882 sample.

2.4 Appendix A: calculation of simplified coincidence summing correction factor for ^{152}Eu

As described in [section 2.2.2](#) the coincidence summing correction factor ([Eq. 2.9a](#)) can be simplified as a function of total efficiency and absolute photopeak efficiency according to the [equation 2.9b](#). The decay data necessary for this calculation are taken from [Monographie BIMP 2005](#). The simplification of coincidence summing correction factor requires the calculation of the gamma rays emission probability, $P_{\gamma(i)}$ ([Eq. 2.10](#) for gamma transition and [Eq. 2.11](#) for X ray transition) and the probability of coincident transitions $P_{\gamma(i,j)}$ as a function of transition probabilities $I_{\gamma(i)} = P_{\gamma(i)} T_{\gamma(i)}$.

^{152}Eu disintegrates 72.1% by electron capture and about 0.027% by emission of positron to ^{152}Sm and by beta minus emission (27.9%) to ^{152}Gd . In [figure A-1](#) is described the simplified decay scheme of ^{152}Eu for the most intense gamma emissions which has a contribution more than 0.005 in the coincidence summing correction factor. In [table A-1](#) are reported the calculated coefficients and a bibliographic confrontation for similar studies ([\[1\] Dryák and Kovář 2009](#); [\[2\] Schima and Hoppes 1983](#); [\[3\] Tomarchio and Rizzo 2011](#)).

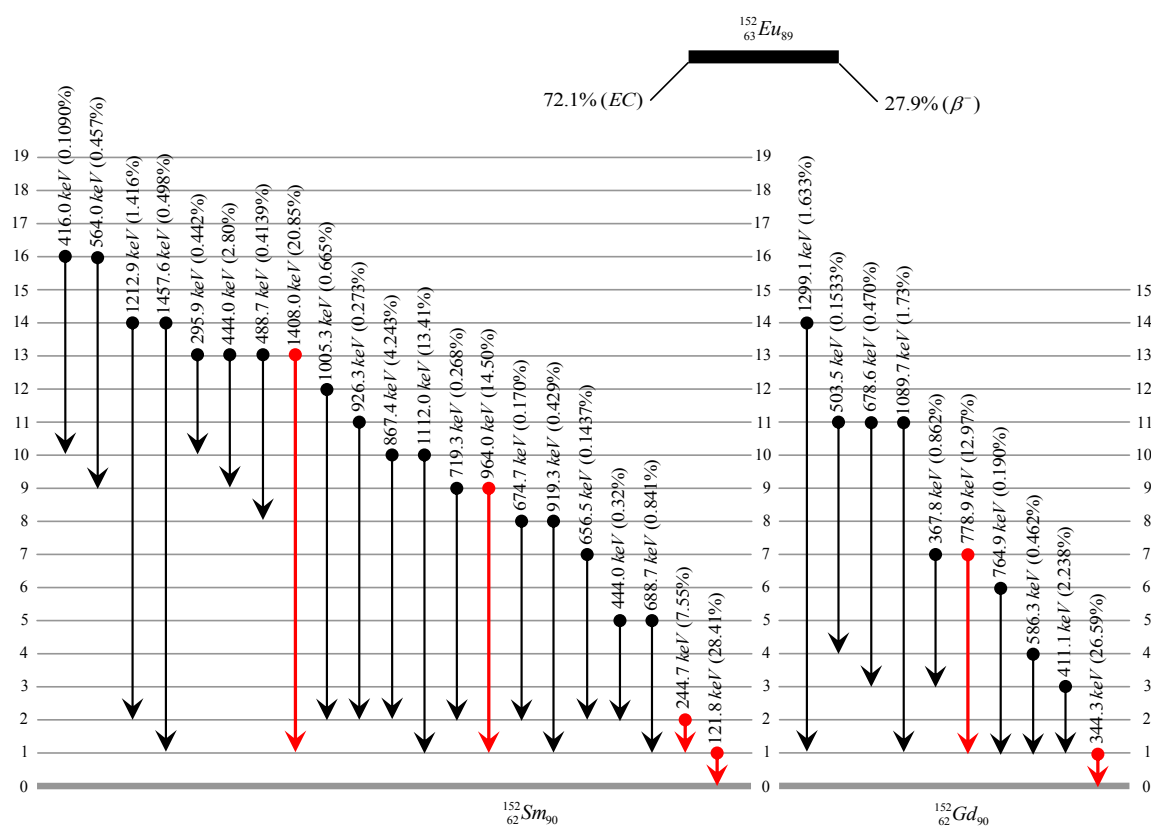


Figure A-1: simplified decay scheme for ^{152}Eu for gamma energies.

Table A-1: tables of coincidence summing coefficients calculated and compared with bibliographic values.**121.8 keV**

Eu-Sm	Energy (keV)	I (%)	Eu-Sm	I	II	III	Energy (keV)	This work	[1]	[2]	[3]
1-0	121.8	28.41	2-1	1-0			244.7	0.1227	0.1232	0.105	0.1227
			13-10	10-1	1-0						
			13-10	10-2	2-1	1-0	295.9	0.0071	-	0.008	0.0070
			13-10	10-5	5-1	1-0					
			13-10	10-9	9-1	1-0					
			5-2	2-1	1-0		444.0	0.0052	-	-	0.0052
			13-9	9-1	1-0						
			13-9	9-2	2-1	1-0	444.0	0.0270	-	-	0.0052
			13-9	9-5	5-1	1-0					
			13-8	8-1	1-0						
			13-8	8-2	2-1	1-0	488.6	0.0067	-	-	0.0062
			5-1	1-0			688.7	0.0137	0.0136	-	0.0137
			10-2	2-1	1-0		867.4	0.0690	0.0691	0.073	0.0690
			8-1	1-0			919.4	0.0070	-	-	0.0070
			9-1	1-0			964.1	0.2357	0.2337	0.247	0.2357
			12-2	2-1	1-0		1005.2	0.0108	0.0108	-	0.0108
			10-1	1-0			1112.1	0.2180	0.2183	0.235	0.2179
			14-2	2-1	1-0		1212.9	0.0230	0.0231	0.024	0.0230
			13-1	1-0			1408.0	0.3390	0.3397	0.364	0.3389
			14-1	1-0			1457.6	0.0081	-	0.009	0.0081
							XK α (Sm)	0.7727	0.6181		
							XK β (Sm)		0.1546	0.772	0.7727
							LX(Sm)	-	0.1283	-	-

244.7 keV

Eu-Sm	Energy (keV)	I (%)	Eu-Sm	I	II	III	Energy (keV)	This work	[1]	[2]	[3]
2-1	244.7	7.55	2-1	1-0			121.8	0.4619	0.4620	0.461	0.4617
			13-10	10-2	2-1		295.9	0.0124	0.0126	0.016	0.0127
			5-2	2-1			444.0	0.0383	0.0381	-	0.0383
			13-8	8-2	2-1		488.7	0.0141	0.0141	-	0.0130
			7-2	2-1			656.5	0.0172	0.0172	-	0.0172
			8-2	2-1			674.7	0.0203	0.0205	-	0.0203
			9-2	2-1			719.4	0.0320	0.0317	0.040	0.0321
			10-2	2-1			867.4	0.5072	0.5061	0.628	0.5074
			11-2	2-1			926.3	0.0326	0.0344	-	0.0326
			12-2	2-1			1005.3	0.0795	0.0793	-	0.0795
			14-2	2-1			1212.9	0.1693	0.1692	0.210	0.1693
							XK α (Sm)		0.8445		
							XK β (Sm)	1.0562	0.2112	1.060	1.0562

							LX(Sm)	-	0.1941	-	-
--	--	--	--	--	--	--	--------	---	--------	---	---

344.3 keV

Eu-Gd	Energy (keV)	I (%)	Eu-Gd	I	II	III	Energy (keV)	This work	[1]	[2]	[3]
1-0	344.3	26.59					324.8	-	-	0.001	-
			7-3	3-1	1-0		367.8	0.0312	-	0.032	0.0312
			3-1	1-0			411.1	0.0809	0.0815	0.081	0.0809
			11-4	4-1	1-0		503.5	0.0044	0.0049	-	0.0050
			-	-	-		520.3	-	0.0019	0.002	-
			4-1	1-0			586.3	0.0167	0.0169	-	0.0167
			11-3	3-1	1-0		678.6	0.0170	0.0171	0.017	0.0170
			6-1	1-0			764.9	0.0069	0.0067	0.006	0.0069
			7-1	1-0			778.9	0.4691	0.4680	0.480	0.4691
			-	-	-		930.6	-	0.003	-	-
			-	-	-		989.7	0.0011	-	-	-
			11-1	1-0			1089.7	0.0626	0.0626	0.063	0.0626
			14-1	1-0			1299.1	0.0591	0.0590	0.060	0.0591
							XK α (Gd)	0.0025	0.0031	0.003	0.0025
							XK β (Gd)	-	0.0008	-	-
							LX(Gd)	-	0.0007	-	-

778.9 keV

Eu-Gd	Energy (keV)	I (%)	Eu-Gd	I	II	III	Energy (keV)	This work	[1]	[2]	[3]
7-1	778.9	12.97	7-1	1-0			344.3	0.9616	0.9616	0.962	0.9617
							520.3	-	0.0039	0.004	-
			7-3				367.8	0.0649	0.0650	0.065	0.0650
			3-1				411.1				
							XK α (Gd)	0.0279	0.0222	0.028	0.0279
							XK β (Gd)	-	0.0057	-	-
							LX(Gd)	-	0.0054	-	-

964.1 keV

Eu-Sm	Energy (keV)	I (%)	Eu-Sm	I	II	III	Energy (keV)	This work	[1]	[2]	[3]
9-1	964.1	14.5	9-1	1-0			121.8	0.4619	0.4618	0.461	0.4617
			13-9	9-1			444.0	0.1120	0.1133	0.116	0.1132
			16-9	9-1			564.0	0.0183	0.0178	-	0.0185
			9-2				719.4	0.0167	0.0167	-	0.0167
			2-1				244.7				
							XK α (Sm)	1.0580	0.8464	1.064	1.058
							XK β (Sm)	-	0.2115	-	-
							LX(Sm)	-	0.1937	-	-

1112.1 keV

Eu-Sm	Energy (keV)	I (%)	Eu-Sm	I	II	III	Energy (keV)	This work	[1]	[2]	[3]
10-1	1112.1	13.41	10-1	1-0			121.8	0.4619	0.4619	0.461	0.4617
			13-10	10-1			295.9	0.0244	0.0249	0.025	0.0249
			16-10	10-1			416.0	0.0060	0.0059	-	0.0062
			10-2				867.4	0.2856	0.2855	0.28	0.2857
			2-1				244.7				
			10-5				423.5	0.0129	-	-	-
			5-1				688.7				
							XK α (Sm)	1.0564	0.8447	1.063	1.0564
							XK β (Sm)		0.2113		
							LX(Sm)	-	0.1936	-	-

1408.0 keV

Eu-Sm	Energy (keV)	I (%)	Eu-Sm	I	II	III	Energy (keV)	This work	[1]	[2]	[3]
13-1	1408.0	20.85	13-1	1-0			121.8	0.4619	0.4620	0.461	0.4617
			13-10	10-1			295.9	0.0157	0.0160	0.016	0.0160
							1112.1				
			13-9				444.0	0.0779	0.0780	0.079	0.0787
			9-1				964.1				
			13-8				488.7	0.0142	0.0142	-	0.0132
			8-1				919.3				
							XK α (Sm)	1.0399	0.8316	1.046	1.0399
							XK β (Sm)		0.2080		
							LX(Sm)	-	0.1933	-	-

The decay data for ^{56}Co are very poor of information in [Monographic BIMP 2005](#) and sometimes insufficient for the coefficient calculation. Therefore the ^{56}Co the coefficients are taken from [Dryák and Kovář 2009](#) and [Tomarchio and Rizzo 2011](#).

Chapter 3

In-situ γ -ray spectrometry: an alternative method on calibration and spectrum analysis



Application of ZaNaI_1.0L system in-situ using a tripod.

- 3.1 In-situ gamma-ray spectrometry using NaI(Tl) scintillation detectors**
 - 3.1.1 *ZaNaI system set-up and calibration*
 - 3.1.2 *An alternative method for calibration and spectrum analysis*

- 3.2 Extensive in-situ gamma-ray spectrometry measurements**
 - 3.2.1 *Brief geological settings: Ombrone Valley (Tuscany Region)*
 - 3.2.2 *In-situ measurements: summary of the results*

- 3.3 Study of correlation between in-situ and laboratory measurements**

Chapter 3

In-situ γ -ray spectrometry: an alternative method on calibration and spectrum analysis

3.1 In-situ gamma-ray spectrometry using portable NaI(Tl) scintillation detectors

3.1.1 ZaNaI system set-up and calibration procedure

The core of ZaNaI_1.0 system is composed by a NaI(Tl) crystal with a cubic shape of a volume of 1 liter (10.16 cm x 10.16 cm x 10.16 cm) and energy resolution of 7.3% at 662 keV (^{137}Cs), 5.2% at 1172 and 1332 keV (^{60}Co). The NaI(Tl) detector is mounted in a backpack ([Fig. 3.1](#)) and accurately folded with shock resistive materials in order to prevent it from possible damages in field. The detector is coupled with a photomultiplier (PMT) base with integrated bias supply, preamplifier and digital multichannel analyzer (MCA). The data outputs are transmitted to a portable notebook via USB communication. Auxiliary equipments like USB communication GPS antenna (54 channels and 10 m accuracy) and a humidity and temperature sensor (10% accuracy) are used for positioning and weather condition measurement, respectively. The sampling period for GPS, humidity and temperature data is of 1 second while the sampling period of gamma-ray spectra depend on the acquisition modality ranging from few seconds to few minutes.

The data logging software are commercial in correspondence to the choice of the equipments, while the analysis is based on self-programmed software based on java environment. Position and gamma-ray records are combined to a geo-referenced data log after off-line post-processing of the data. These data log formats are easily imported to GIS systems and Google Earth(R) in order to produce radiation maps or logging points.



Figure 3.1: configuration of ZaNaI_1.0 system set-up in a backpack.

An alternative approach on calibration procedure

Portable instruments are usually calibrated for natural radioactivity measurements by means of standard spectra acquired at least using three concrete pads enriched in K, U and Th and a pad free of radioactivity representing the background ([Hendriks et al. 2001](#); [Engelbrecht and Shwaiger 2008](#); [Løvborg et al. 1981](#); [Løvborg 1984](#)). Here is discussed the calibration procedure, while the spectra analysis will be described in the next section.

Table 3.1: typical concentrations of constructed pads used to calibrate in-situ gamma-ray spectrometers ([IAEA 1990](#)).

Pad	K (%)	eU (ppm)	eTh (ppm)
Background	0.5	1.1	1.4
Potassium	6.5	1.1	1.4
Uranium	0.5	50.0	1.5
Thorium	0.5	6.4	125.0

These pads (e.g. [table 3.1](#)) are usually concrete constructions of cylindrical shape, having finite dimensions of 2-3 m in diameter and 0.3-0.5 m thick (considering the result of the theoretical calculation) and for this reason it is needed a geometrical correction due to the differences from an infinite calibration sources. It is worth mentioning that the hypothesis of homogeneous distributions of the radionuclides in the pad mixture should be verified and that the cost of production, handling and storage of the pads are not negligible. In [figure 3.2](#) are represented the calibration pads facilities all over the world.

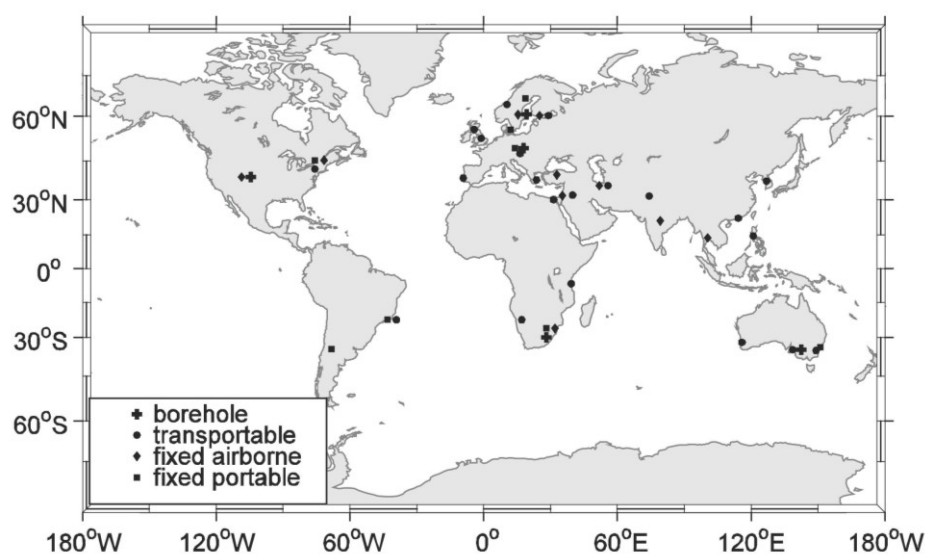


Figure 3.2: worldwide calibration facilities (pad): data source [IAEA 2010](#).

[Hendriks et al. 2001](#) proposed as an alternative of a simplified solution of building pads by not using concrete but silversand mixed with KCl for the potassium pad, monazite for the thorium pad, and slags for the uranium pad. The design of an ideal pad with one radionuclide inside and with a perfect homogeneous distribution of the radioisotope in its volume is impossible, because impurities and non-homogeneities are always present. For example, a clear contamination of uranium in thorium pads has been often seen, as reported by Hendriks and co-workers. For this reason, compromises between accuracy and applicability of the method have to be weighted.

In this section is described an alternative calibration procedure, instead of using constructed pads. It is based on the selection of sites characterized by a prevalent concentration of one of the natural radionuclides. Even if it is almost impossible to select one site which contains only one of the nuclides, the selection will be oriented toward sites with unbalanced contents. Since most of the γ -rays emanating from the earth's surface originate in the top 30 cm depending on the rock/soil density the

radioactivity characterization of each site is performed sampling at maximum 10 cm depth (**Table 3.2**).

Table 3.2: half-thickness ($\Delta x = \log(2) / \mu_l$, where μ_l (m^{-1}) is the linear mass attenuation coefficient) of the most intense gamma-energies of in-situ measurement importance.

Isotope (Energy)	²¹⁴ Bi (609 keV)	⁴⁰ K (1460 keV)	²¹⁴ Bi (1764 keV)	²⁰⁸ Tl (2614Th)
Air (SPT)	67	102	112	137
Soil (1g cm ⁻³)	0.037	0.057	0.063	0.077
Rock (2g cm ⁻³)	0.018	0.028	0.031	0.038
Rock (2.5g cm ⁻³)	0.015	0.022	0.025	0.030
Rock (3g cm ⁻³)	0.012	0.019	0.021	0.025

* mass attenuation coefficients for air in standard temperature and pressure conditions taken from XCOM 3.1 database available on-line developed by Nuclear Institute of Standards and Technology (NIST) and the mass attenuation coefficients were deduces from equation 2.23.

All calibration sites (e.g. **Fig. 3.3**) were selected using geological and geo-morphological considerations and further validated trough laboratory measurements (a list of all the sites and the concentration of each isotope are reported in **Table 3.3**). The in situ measurements can be affected by the specificity of the place, like the soil non-homogeneity, the ground morphology, the non secular equilibrium in radioactive chains, the vertical distribution of ¹³⁷Cs, the presence of vegetation, moisture, etc. Thus, the compromising on choosing s calibration sites should be done according precise prescriptions:

- relatively uniform distribution of radionuclides in secular equilibrium with their products,
- plane area without any steps and large enough to be approximated as an infinite source (maximum 10 m radius (**Grasty et al. 1979**)),
- undisturbed areas: assuring relatively low ¹³⁷Cs vertical distribution
- uniform and relatively low and homogeneous soil moisture content and vegetable coverage.



Figure 3.3: example of a natural calibration site (GC1 see [table 3.3](#)).

For each site, a variable number from 5 to 12 samples were collected in random positions within 10 m radius in order to check also the homogeneity of the site around the detector since more than 90% of γ -rays detected by the sodium iodide are produced by the 7 m radius and 0.5 m deep area around ([Grasty et al. 1979](#)). The homogeneity of the each site is assured inside the error reported in [Table 3.3](#). Soil and rock samples were dried, homogenized (less than 2 mm fine grain size) and sealed in measurement containers for at least four weeks in order to allow the ^{222}Rn growth up prior to be measured using high-resolution γ -ray spectrometry system MCA_Rad (describen in [chapter 2](#)) following international standards of analysis ([ASTM C1402-04 2009](#); [UNI 10797: 1999](#)). Only the CA1 site (discussed in the next section in details) is not a natural site, but it is made by a pad of KCl fertilizer. The concentrations reported in [Table 3.3](#) are the average of the measurements performed in the laboratory on the collected rock samples. This way the heterogeneity of each site is properly implemented by the errors which are dominated by the spread in the results of the collected samples in each calibration site. The number of calibration sites are greater than the number of investigated radioelements, as in our approach. This is mandatory in order to avoid artifacts in the sensitive spectra.

One advantage of this calibration approach is the possibility to take into account radionuclides other than ^{40}K , ^{232}Th , and ^{238}U (as we mentioned above, in general a minimum of $k+1$ sites are needed, where k is the number of nuclides we want to be sensitive to). In our case a site with a prevalent concentration of ^{137}Cs has been included and used in the calibration (the CC2 site in [Table 3.3](#)). As a matter of fact, after the Chernobyl accident, it is a mandatory to take into account the ^{137}Cs signal in the spectrum analysis. This is clearly visible in [Figure 3.4](#) where the presence of cesium is definitively not negligible (the γ -peak energy is 662 keV). If necessary, other radioisotopes due to nuclear accidents, like ^{131}I , could be added in the future.

Table 3.3: the average of the distribution of natural radioisotopes concentration. The errors correspond to one standard deviation.

ID	Site type	K (%)	eU (ppm)	eTh (ppm)	Cs* (Bq/kg)
CA1	potassium	53.9 ± 0.7	< 1.0	6.0 ± 0.5	na
CC2	cesium	0.06 ± 0.02	0.7 ± 0.3	0.6 ± 0.7	61^{+100}_{-61}
GC1	background	0.07 ± 0.04	0.27 ± 0.08	1.14 ± 0.13	0.87 ± 0.04
GV1	mix	4.9 ± 0.6	7.5 ± 1.1	7 ± 1	31 ± 18
PM2	mix	2.26 ± 0.05	2.27 ± 0.18	10.7 ± 0.8	18 ± 9
RT1	uranium	0.10 ± 0.01	6.8 ± 1.1	1.74 ± 0.16	6 ± 5
SM1	mix	1.54 ± 0.14	1.6 ± 0.3	8.6 ± 0.6	26^{+37}_{-26}
SP2	thorium	2.92 ± 0.08	7.5 ± 0.4	39 ± 2	23 ± 2
ST2	thorium	7.8 ± 0.9	36 ± 5	124 ± 16	8 ± 4

* the activity concentrations of ^{137}Cs expressed in Bq/kg correspond to the samples of soil measured in laboratory, showing as expected relatively high variability horizontal distribution but not considered for the overall characterization of the site since doesn't consider the vertical distribution.

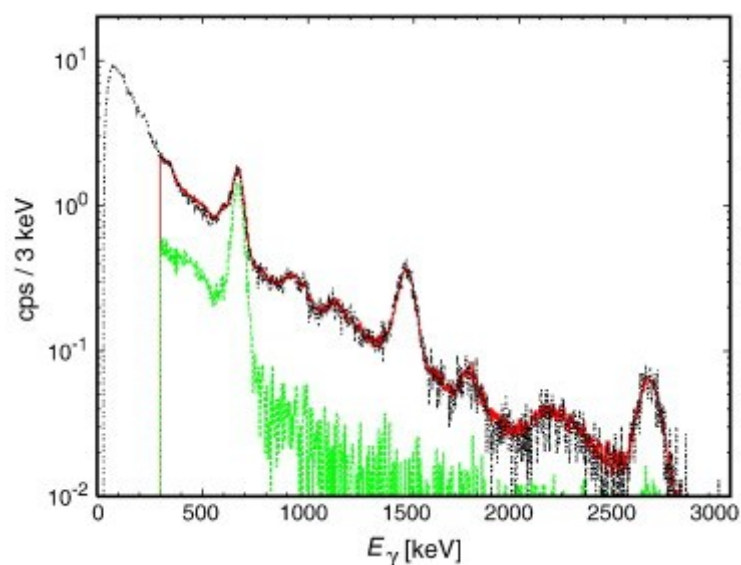


Figure 3.4: spectra acquired in-situ (black dashed line) compared with the fit (full red line) obtained by the FSA with NNLS constrain (described later). The ^{137}Cs contribution is shown alone (green dotted line) to underline the need to include this element in the analysis.

3.1.2 An alternative approach for calibration and spectrum analysis

Windows analysis method (WAM)

The conventional approach of spectra analysis recorded in-situ for studying the specific activity concentration, is to calibrate broad spectral windows during the analysis for the main natural isotopes (Verdoya et al. 2009; Desbarats and Killeen 1990). Generally, these windows are chosen around the photopeaks of ^{40}K (1460 keV), of ^{214}Bi (1765 keV), and of ^{208}Tl (2614 keV) (Table 3.4). The concentration of ^{238}U and ^{232}Th are then evaluated detecting the γ -rays produced by ^{214}Bi and ^{208}Tl respectively. The assumption of secular equilibrium of the decay chains is required in order to use this approach. In addition to the abovementioned radionuclides, the three-windows method has been extended to the measurement of ^{137}Cs by Cresswell et al. 2006 and Sanderson et al. 1989.

Table 3.4: typical energy windows used to estimate the activity concentration for in-situ measurements (IAEA 2003).

	Isotope	Energy (keV)	Window width (keV)
potassium	40K	1460	1370-1570
uranium	214Bi	1765	1660-1860
thorium	208Tl	2614	2410-2810
Total	-	-	400-2810

* this windows are accepted in order to standardize the method but some other authors used different windows and have developed other windows for the study of other isotopes (Allyson 1994)

The relationship between the background corrected count rate, R_{ij} , where $i = 1,2,3$ for the isotopes K, U, Th and $j = 1,2,3$ for the three pads of potassium, uranium and thorium, while C_{ij} are the relative concentrations, is given by:

$$R_{ij} = S_{ij}C_{ij} + S_{ij}C_{ij} + S_{ij}C_{ij} \quad (\text{Eq. 3.1})$$

where S_{ij} are the instrument sensitivities (cps per unit of concentration). This expression can be written in matrix notation:

$$[N] = [C] \times [S] \quad (\text{Eq. 3.2})$$

An example of the sensitivity constant estimated for a 7.64 cm x 7.64 cm NaI(Tl) is given at IAEA 2003 is shown in table 3.5.

Table 3.5: example of sensitivity matrix calculated for 7.64 cm x 7.64 cm NaI(Tl) detector using standard calibration pads.

[S]	Potassium window	Uranium window	Thorium window
cps / % K	3.360	0.000	0.000
cps / ppm eU	0.250	0.325	0.011
cps / ppm eTh	0.062	0.075	0.128

As a comparative example the same calculation is done for a 7.64 x 7.64 cm NaI(Tl) using the standard spectra recorded at natural sites: the sensitivity matrix is given below (see natural site concentrations [Table 3.3](#)).

Table 3.6: example of sensitivity matrix calculated for 7.64 cm x 7.64 cm NaI(Tl) detector using natural calibration pads.

[S]	Potassium window	Uranium window	Thorium window
cps / % K	3.645	-0.002	-0.001
cps / ppm eU	0.289	0.319	-0.001
cps / ppm eTh	0.079	0.069	0.142

Using the sensitivity matrix ([Table 3.5](#) and [3.6](#)) from [equation 3.3](#) are estimated unknown concentrations.

$$[C] = [N] \times [S]^{-1} \quad (\text{Eq. 3.3})$$

Where the $[S]^{-1}$ is the inverse matrix of the sensitivity ([Table 3.6](#)), $[C]$ is therefore a vector row matrix of the unknown concentrations of potassium, uranium and thorium corresponding to the counts in $[N]$ row vector matrix for the three photopeaks.

The most important limit of this method is that it is blind to any unexpected signal (atrophic isotopes). Other limitation are the low accuracy for short time acquisitions and the physical restriction of poor intrinsic energetic resolution of NaI(Tl) detector. In particular, the Compton continuum around ^{137}Cs photopeak is generally very intense compared to the intensity of 662 keV γ -line. This translates into long acquisition times and costs. Moreover, the intrinsic energetic resolution of sodium iodide detectors prevents to resolve the triplet at 583 keV (^{208}Tl), 609 keV (^{214}Bi), and 662 keV (^{137}Cs). This issue can be solved only by post processing the data. In any case as we mentioned above the windows analysis method requires a prior knowledge of the presence on site of such radioisotope.

Full spectrum analysis (FSA) method

A solution to the above mentioned limitations, comes from the utilisation of the full spectrum analysis (FSA) method. This method has been developed in different approaches (Maucec et al. 2009; Hendriks et al. 2001; Minty 1992; Crossley and Reid 1982; Smith et al. 1983) and was found to be a successful spectrum analysis tool. When applied to scintillation detectors, it enhances their potentialities for radioisotope quantitative determination. As a matter of fact, the FSA encompasses almost the full energy spectrum, reducing the time required in order to reach an acceptable statistical uncertainty of a single measurement.

The spectra acquired in situ are processed by fitting them with a linear combination of the so-called fundamental spectra (of each investigated isotope) derived from the calibration procedure. The events registered in each channel in the measured spectrum, N , is then expressed as:

$$N(i) = \sum_{j=1}^4 C_j S_j(i) + B(i) \quad (\text{Eq. 3.4})$$

where

- $N(i)$ are the counts in the channel i ,
 - C_k are the concentration of the element k ,
 - $S_k(i)$ are the associated counts to the fundamental spectrum of the element k in the channel i ,
 - $B(i)$ are the counts in the channel i due to the intrinsic background
- and the index k stays for ^{40}K , ^{232}Th , ^{238}U , and ^{137}Cs .

It has become a conventional representation for in-situ measurements, for geological purposes, to express the concentrations of natural radioisotopes in their respective abundances, where ^{40}K is given in % weight while eU and eTh are given in ppm. The ^{137}Cs is expressed as the absorbed dose by the detector (nGy/h) due to the heterogeneous distribution property of anthropic radioisotopes (described later). The activity concentrations are deduced applying the least square algorithm to rectangular matrix and minimizing the reduced χ^2 according to the following equation:

$$\chi^2 = \frac{1}{n-5} \frac{\sum_{i=1}^n \left[N(i) - \sum_{j=1}^4 C_j S_j(i) - B(i) \right]^2}{\sigma_{N(i)}^2} \quad (\text{Eq. 3.5})$$

where the $N(i)$ is considered Poisson distributed (then $\sigma_{N(i)} = \sqrt{N(i)}$) and n is the number of channels in the spectrum used in the analysis (867 in our case, for the energetic range 300-2900 keV as described below).

During the calibration of the system the fundamental spectra (the S matrix) are obtained by solving **equation 3.6** using the radionuclide concentrations (the C_k coefficients) reported in **Table 3.3**.

$$[S] = [C]^{-1} \times [N] \quad (\text{Eq. 3.6})$$

The matrix notation has dimensions $\dim N = 9 \times 867$; $\dim S = 4 \times 867$ and $\dim C = 9 \times 4$. It has to be noted that the FSA calibration method produces also the background spectra, B for ZaNaI_1.0L. Only the energy range from 300 keV up to 2900 keV is considered in the analysis. Below 300 keV there is a strong presence of the backscattering events which depends on the atomic number and density of the surrounding materials. Above 2900 keV only the cosmic ray contribution is present 1.

The solution of **Eq. 3.5** is repeated through a trimming procedure is executed by changing the site concentrations (C_k) in small steps around the measured intervals and repeating the matrix solution. This strategy has been implemented in order to correct the unavoidable differences between the sample measured concentrations and the average site values. The need of this correction is evident observing the spectra acquired at the CA1 site where the sodium iodide detector was placed on a large platform made of KCl fertilizer used as potassium calibration site. The KCl was stored inside a building and in the NaI(Tl) spectra are clearly visible the peaks due to the thorium and uranium contained inside the building walls. In the samples analyzed by the MCA_Rad system, the contribution from these two elements was not present. **Figure 3.5** shows the γ -spectrum acquired in CA1 site compared with the fit spectrum obtained by assuming only the concentrations obtained by the measurements on samples in laboratory.

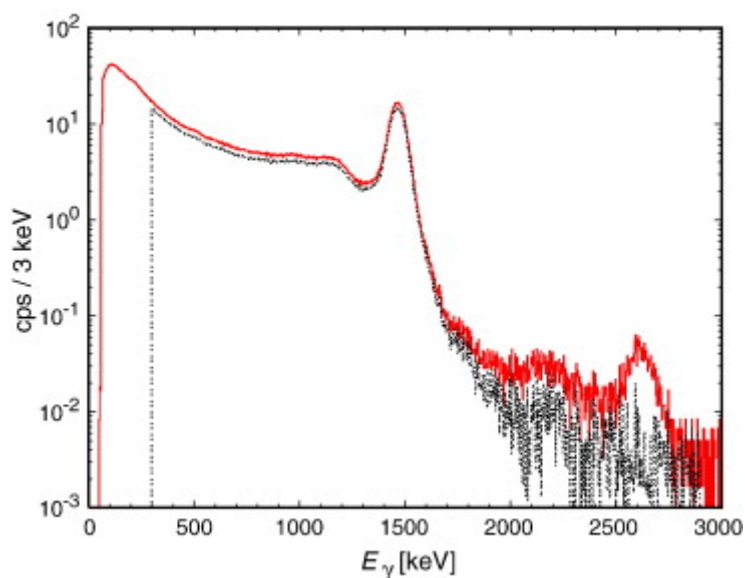


Figure 3.5: the spectra acquired in CA1 site in (red full line). The fit obtained using the concentrations measured with the MCA_Rad system is also reported (black dashed line).

Except for CA1, this procedure applied to the other sites produce a deviation from the concentrations reported in [Table 3.3](#) within 1σ which confirms the assumption of acceptable homogeneity declared in the previous section.

Improvement on FSA method: application of non-negative least square (NNLS) constrain

The χ^2 minimization without any further conditions, which is the base of the FSA method, can generate sensitive spectra having energy regions with negative events. Two evident examples of this problem are shown in [Figure 3.6](#) and [3.7](#).

The presence of these non physical results introduces crosstalk effects in the analysis, leading to systematic errors. The NNLS (Non Negative Least Square) constraint ([Lawson and Hanson 1995](#); [D'esesquelles et al. 2009](#); [Boutsidis and Drineas 2009](#)), which forces the counts on each bin to be zero or positive, has been implemented for the first time in the FSA algorithm in order to avoid this problem ([Baldoncini 2010](#)).

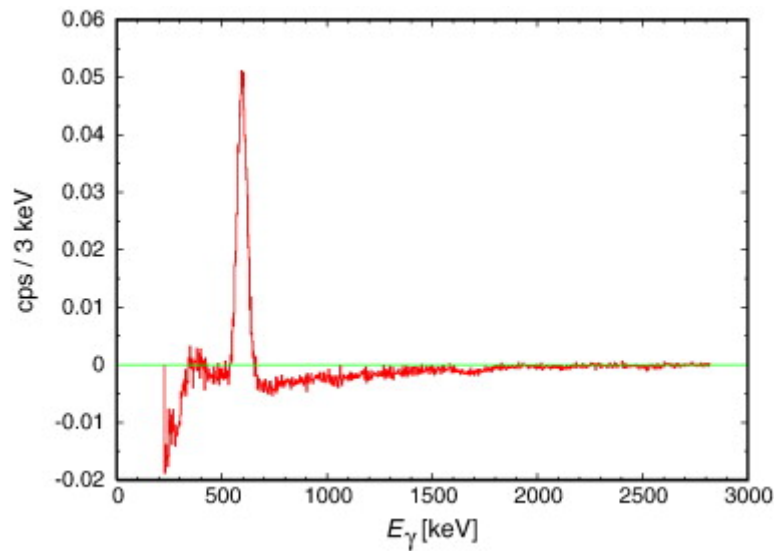


Figure 3.6: the sensitive spectra of ^{137}Cs , obtained using the standard FSA method. The green line is placed to show the zero count level.

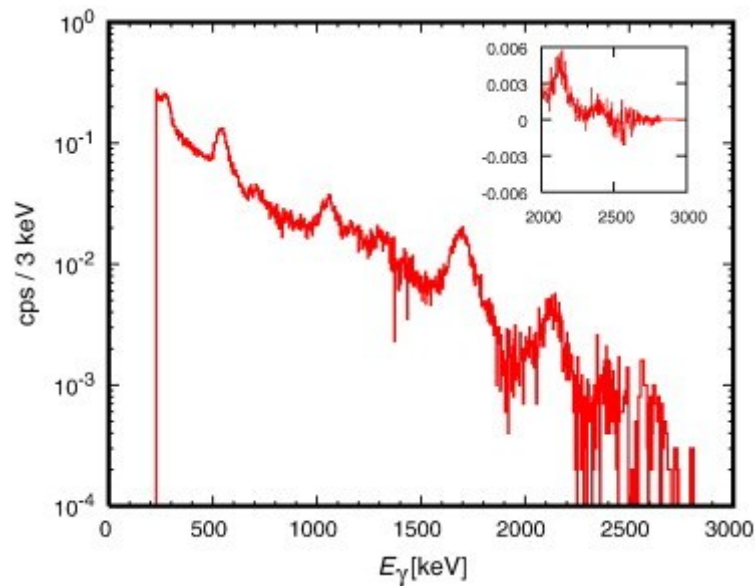


Figure 3.7: the sensitive spectra of ^{238}U , obtained using the standard FSA method. The region where there are negative counts is emphasized in the box.

The NNLS algorithm is based on the Kuhn-Tucker condition for Problem of Least Square with Linear Inequality Constraint (LSI) ([Lawson and Hanson 1995](#)). If the problem has a solution with least square minimization this theorem states that exist also a solution of the problem with non negative values. In general the least square problem of linear inequality is proposed as the problem of minimization of $\|Ex - f\|$ under the condition that $Gx \geq h$ (where h is null vector and G is the identity matrix), which in the case of non-negative least square (NNLS) is taken as $x \geq 0$. The following

theorem gives the characterization of the solution vector of the LSI problem which is the Kuhn-Tucker condition:

A vector \hat{x} having n rows is the solution of the problem LSI if and only if exist a vector \hat{y} having m rows and an internal subdivision from 1 to m in two sub values ξ and ζ in order that:

$$\hat{y} = E^T (E\hat{x} - f) \quad (\text{Eq. 3.7})$$

$$\hat{x}_i = 0 \text{ for } i \in \xi \text{ and } \hat{x}_i > 0 \text{ for } i \in \zeta \quad (\text{Eq. 3.7a})$$

$$\hat{y}_i \geq 0 \text{ for } i \in \xi \text{ and } \hat{y}_i = 0 \text{ for } i \in \zeta \quad (\text{Eq. 3.7b})$$

The NNLS algorithm is based on the solution dual problem described from [equation 3.7b](#), with \hat{y} defined from [equation 3.7](#) having solution only if the original problem has one.

The sensitive spectra calculated with the algorithm implementing the NNLS constrain are shown in [Figure 3.8](#). It can be seen directly a more comprehensive sensitivity spectra. It has to be noted that the resolution of the sensitive spectra resolution can be severely affected by gain mismatch and therefore an accurate calibration and check is always needed. Finally, residual correlations between isotopes are still present in the sensitive spectra shape, due to the presence of all the radionuclides in most of the selected sites.

As we mentioned above, ^{137}Cs has been added to the analysis since it was found having not negligible concentrations in soils and here is reported as an example of the potentiality of the FSA-NNLS method. It was deposited principally from nuclear fallout, distributed randomly from climatic events around the Europe. The profile distribution of ^{137}Cs in soil systems shows a tendency of decrease toward deeper layers ([Zhiyanski et al. 2008](#)). The ^{137}Cs distribution shows also a heterogeneous superficial distribution in soils and this is confirmed by the measurements performed on samples collected which show a large distribution of ^{137}Cs values in top-soil (see [Table 3.3](#)). As a matter of fact, the NaI(Tl) detector, which records the γ -rays produced by a wide surface area, is the best solution in order to average the cesium amount in the soil. In particular, it is possible to avoid over/under estimations due to point-like sampling. It has to be noted that the sensitive spectrum for ^{137}Cs is dominated by the CC2 site which contain low concentrations of natural radioisotopes and with an high value of ^{137}Cs . In this way the cesium sensitive spectrum is free from correlations with the other radioisotopes. The dose absorbed by the detector, D , which takes into account the heterogeneity

of the isotope in soils, is calculated summing the counts in each channel of the sensitive spectrum $S_{Cs(i)}$ weighted with the channel's energy $E(i)$ and detector mass, m . This is multiplied by the C_{Cs} coefficient derived by the FSA+NNLS algorithm as in the following equation:

$$D = \frac{1}{m} C_{Cs} \sum_i^n S_{Cs(i)} E_{(i)} \quad (\text{Eq. 3.8})$$

As described in above, the sensitive spectra are calculated in a range of energy from 300 keV up to 2900 keV, while the contribution to the dose due to energies below 300 keV has been extended a posteriori.

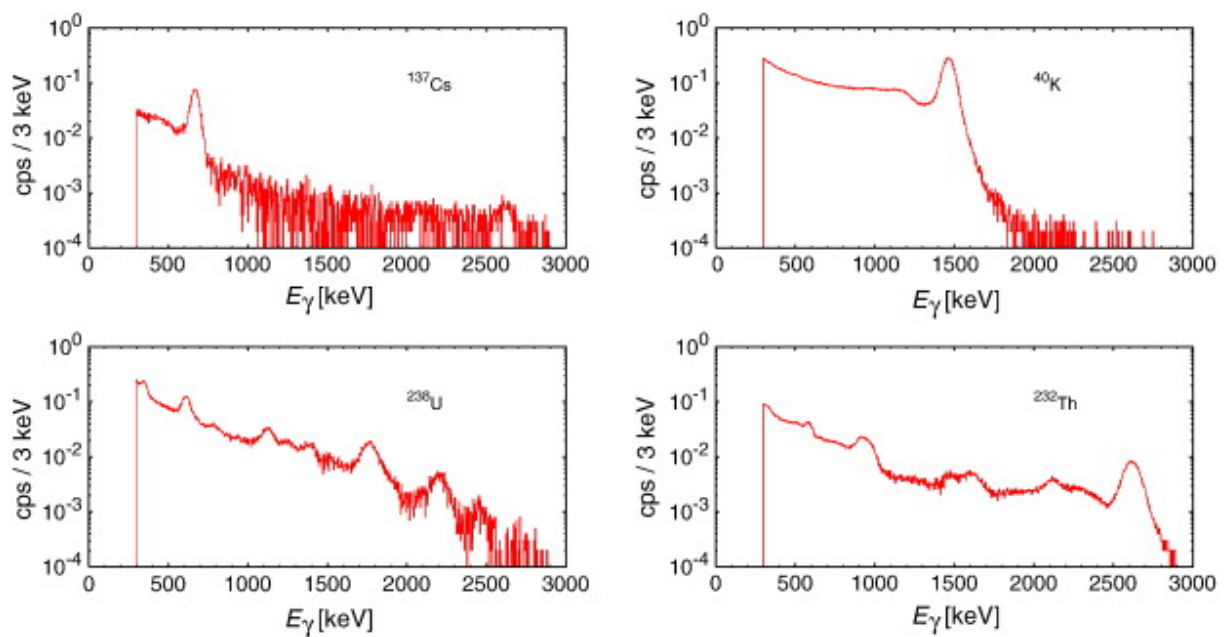


Figure 3.8: the sensitive spectra obtained through the FSA method with NNLS constrain.

3.2 Extensive in-situ gamma-ray spectrometry measurements

3.2.1 Brief geological settings: Ombrone Valley (Tuscany Region)

This chapter is devoted to a brief geological description of the Ombrone Valley, located in southern Tuscany, which area were chosen for natural radioactivity measurements. An hydrographic basin is the topographic area collecting waters flowing on the topsoil surface and merge into a specific hydric body that gives the name to the basin itself. Each hydrographic basin is separated by the contiguous

ones by the so called 'watershed line'. The greatest part of major hydrographic basins is formed by the sum of more sub-basins represented by hydrographic basins of every single affluent of the main river. The hydrographic basin differentiates from the hydrogeologic basin, because the latter considers the draining of superficial waters, as well as the flow of those present in the subsoil.

The regional basin of Ombrone Valley (southern Tuscany) is divided in 4 hydrographic sub-basins: Ombrone, Albegna, Bruna and Osa. It extends for 3.494 km². The main river of the valley is the Ombrone, which springs from the south-eastern part of Chianti Mountains in S. Gusmé and flows for 160 km up to the Tyrrhenian Sea, in the south-west area of Grosseto. 3/5 of the Ombrone hydrographic basin are in the province of Siena, whereas 2/5 belong to Grosseto area.

The Ombrone Valley is formed by structural alignments (dorsals) and by Neogenic-Quaternary basins.

The Dorsals are the following:

- Medium Tuscan Dorsal: formed by Montagnola Senese and by Monticiano-Roccasarda dorsal. Crop formations are composed by Carbonatic-clay-siliceous lithologies of the Palaeozoic and Mesozoic ages.
- The Rapolano Terme-M. Cetona dorsal: formed by a reversed anticlinal ripple. Cropping formations are lithologically common to the Falda Toscana and to the Ligurian Units.
- The Monte Amiata dorsal: constituted by the Murlo-Montalcino dorsal, the volcanic complex of M. Amiata and the nucleus of Castell'Azzara; crop formations belong (from the most recent) to the Neoauctonous Complex, the Ligurian Units, the Austroalpine Units and to the Tuscan aquifer.

The Neogenic-Quaternary basins are:

- The Graben of Siena, which is eastern confined by the Rapolano Terme- M. Cetona dorsal, western by Montagnola Senese, northern by Monteriggioni and by Chianti Mountains, and southern by Pienza. The Graben of Siena is filled by marine deposits of inferior-medium Pliocenes, which are composed by clays, sand clays, and sands with lenses of conglomerates.
- The Chiusdino basin: in which neoauctonous deposits crop out, such as clays, sands and conglomerates, as well as lacustrine formations (Pian di Feccia).
- The Radicofani basin: which is north-bounded by Pienza Threshold (the latter divides it by the Graben of Siena), and western bounded by the Amiata dorsal, eastern by the Rapolano Terme-M. Cetona dorsal, and southern by the vulcanites of the volcanic complex of Latera. The lithology that crops out is composed by clays deposits broken up by sand levels and pebbles.

In **fig. 3.9** the geological map of Ombrone Valley is shown together with 80 highlighted points in which natural radioactivity measurements have been performed.

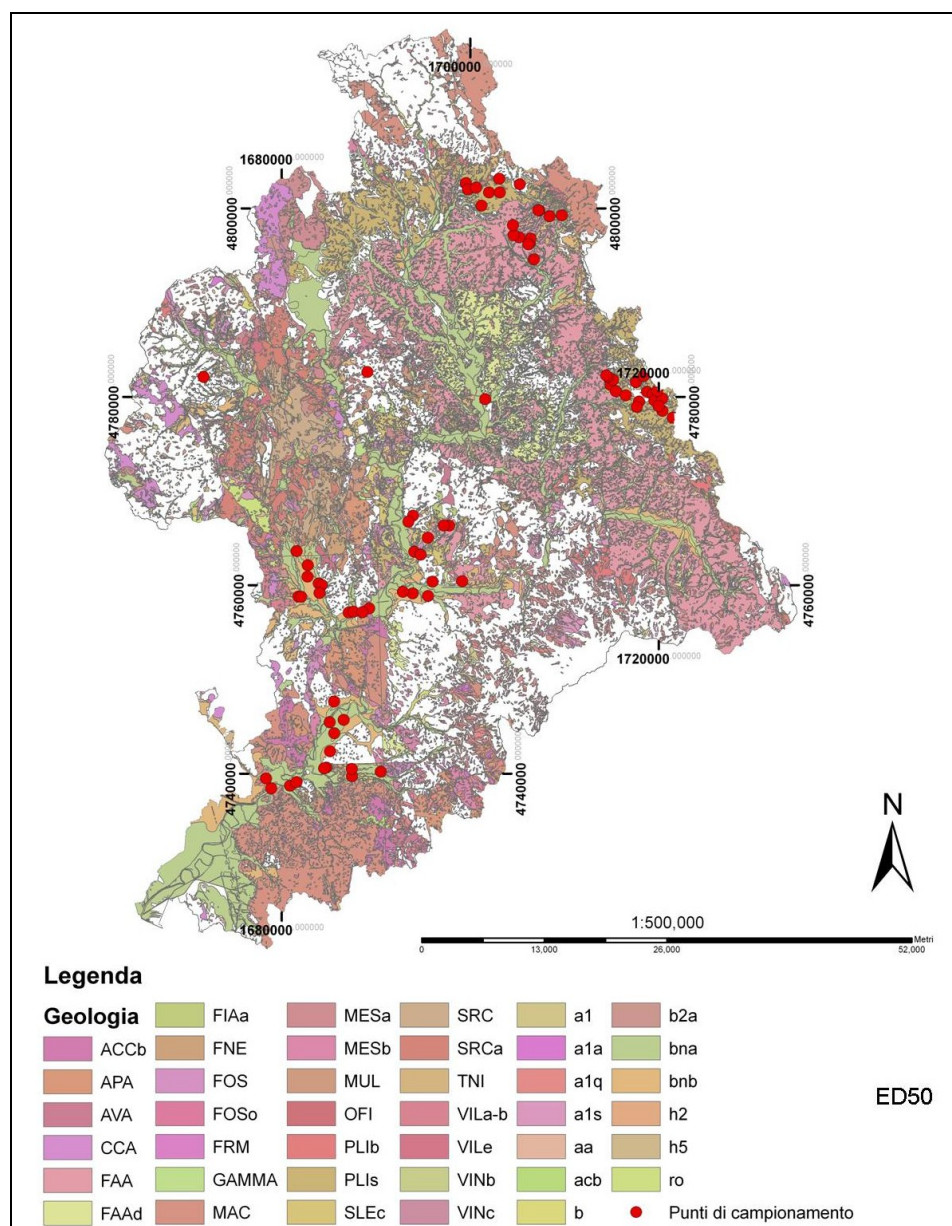


Figure 3.9: the geological map 1:50,000 of Ombrone basin showing the distribution of in-situ gamma-ray spectrometry measurement points. The detailed legend is available from data source: <http://www.geotecnologie.unisi.it/>.

3.2.2 In-situ measurements: summary of the results

Recently an intense campaign of measurements was dedicated to the geological study of the soil in Tuscany region. The survey is situated between the regions of Siena and Grosseto in Ombrone river

basin (see [Figure 3.10](#)). This territory is characterized by a highly diversified geological structure (as described above) and it is studied by measuring different aspects and characteristics of the soil.

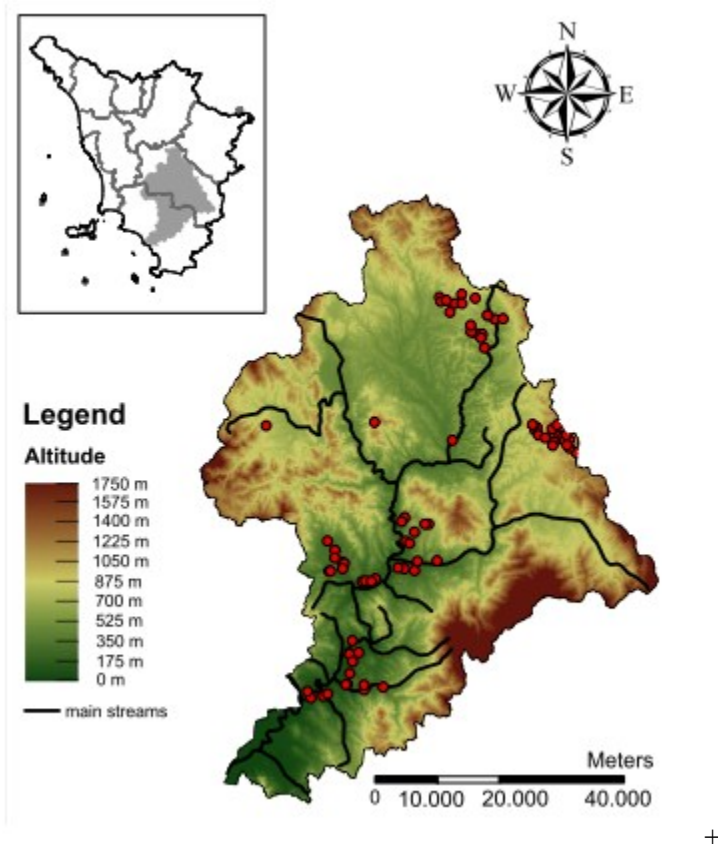


Figure 3.10: the digital terrain model of position of Ombrone basin and the 80 sites investigated in the area.

In situ gamma-ray spectrometry with sodium iodide scintillators is a consolidated method for radioactive survey ([Løvborg et al., 1979](#); [Miller and Shebell 1993](#); [Tyler, 2007](#)) with a wide range of applications from mineral exploration to environmental radiation monitoring. The natural radioactivity is investigated at 80 different sites in relatively similar terrain morphological conditions. Both in-situ measurements with portable NaI(Tl) detector (ZaNaI_1.0L) and by collecting samples for laboratory measurements with the MCA_Rad system (described later in details) were done. The sites selection for field measurements fulfilled the same criteria chosen for the calibration procedure, in particular for the topology of the site. For each site the NaI(Tl) detector was used to perform 5 minutes in-situ ground measurements: the acquisition time was chosen in order to have enough statistics for a comparison with the windows analysis method.

Each spectra was analyzed using FSA method with NNLS constrain (based on the new calibration approach described above). Before analysis is accurately performed an energetic recalibration and

rebinding by taking 3 keV per channel. The analysis protocols are implemented in a self constructed software called jRadView (not discussed here) based on [ANSI NO.42.14 1999](#) standard for common analysis protocols.

In [Figure 3.11](#) are reported the distribution of measurements in-situ and the calculate absorbed dose rates (discussed in [section 1.2.1](#)). From 80 in-situ measurements was observed an average of specific activity concentration of ^{40}K , ^{238}U and ^{232}Th are $518\pm 146 \text{ Bq kg}^{-1}$, $29\pm 7 \text{ Bq kg}^{-1}$ and $33\pm 8 \text{ Bq kg}^{-1}$ respectively. The average absorbed dose rate for external gamma radiation of Ombrone basin of $55\pm 12 \text{ nGy h}^{-1}$, compared with the world wide reported typical range of variability from 10 to 200 nGy h^{-1} ([UNSCEAR 2000](#)). According to [UNSCEAR 2000](#) the population-weighted values give an average absorbed dose rate in air outdoors from terrestrial gamma radiation of 60 nGy h^{-1} .

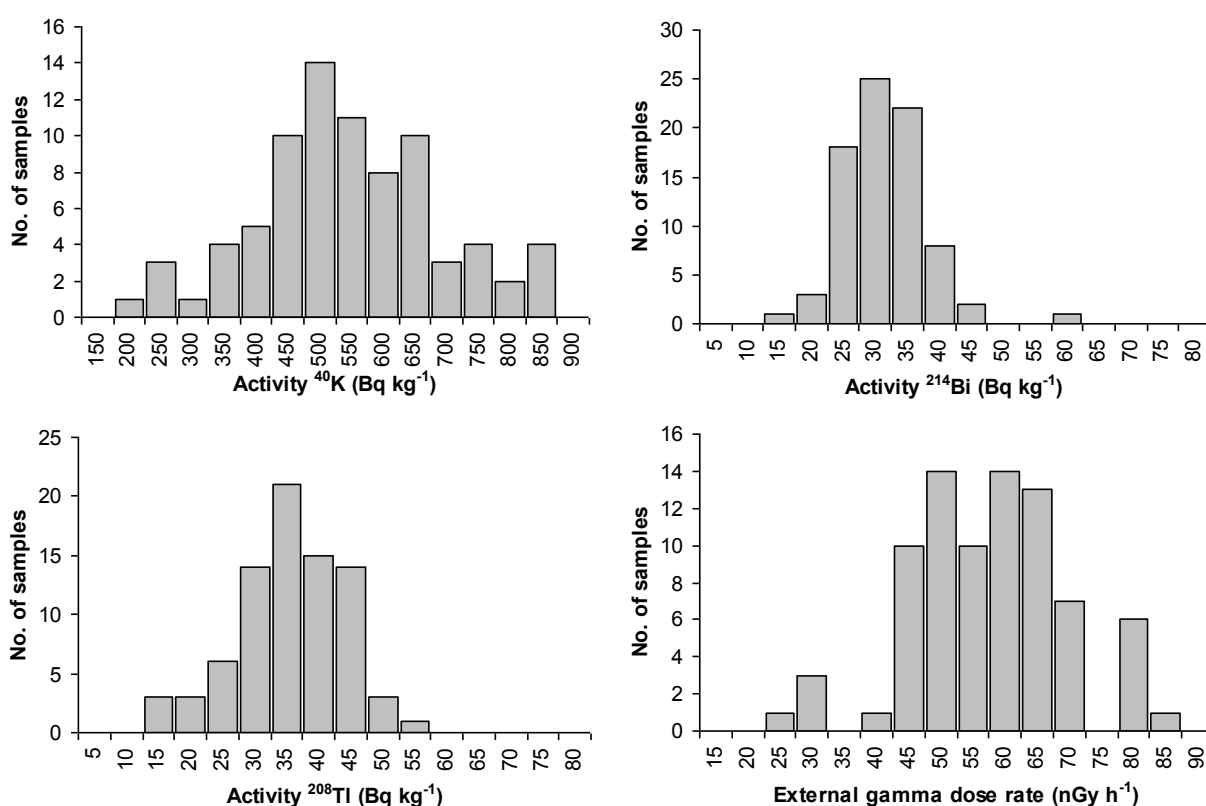


Figure 3.11: the distributions specific activity concentration and external gamma absorbed dose rates for 80 in-situ measurements.

The $\text{ZaNaI}_{1.0\text{L}}$ is designed in order to be freely used in different modalities, for those different from the calibration configuration some necessary correction are needed. In order to investigate larger areas measurements at 1m height above the ground using tripods are common practice. Furthermore, $\text{ZaNaI}_{1.0\text{L}}$ is configured in order to perform dynamic surveys, holding it on a backpack ([Fig. 3.12](#)). Therefore, in order to estimate the correction factor due to change in geometry configuration like using

a tripod (1m height) and backpack (about 1 m height) a series of measurement were done in such conditions. The confrontation of the different measurement geometries show a good correlation ([table 3.7](#)), therefore the correction factors are estimated from the slope coefficients ([table 3.7](#)).



Figure 3.12: the tripod (static) and human back (dynamic) modalities of in-situ measurements.

Table 3.7: the correction factors applied to in-situ measurement at different measurement geometries (1m height tripod and holding on back bag at about 1m height).

Correction factor expressed in %				
	Regression coefficient (R ²)	Tripod (1m height)	Regression coefficient (R ²)	Backpack (1m height)
⁴⁰ K	0.999	5.7 ± 0.4	0.999	17 ± 1
²³⁸ U	0.986	na	0.985	na
²³² Th	0.998	5.2 ± 0.5	0.999	15 ± 1

In the case of ²³⁸U the correction factor is rather negligible at 1m height, since the signal in ²³⁸U spectra is altered by the increasing signal due to radon gas present in surface air.

3.3 Study of correlation between in-situ and laboratory measurements

There are several sources of background radiation and environmental factors that interfere with in-situ measurements of the radiation emitted from potassium, uranium and thorium in the soil.

- Cosmic rays (described in [chapter 1](#)) such as high energy gamma rays of cosmic origin interact with particles in the upper atmosphere causing a spectrum of background gamma rays in the detector. Furthermore, the choice of the site can influence to this contribution due to the effect of doubling the cosmic radiation of every 1.5 - 2 km of height above sea level.
- Another important parameter is radon (^{222}Rn) gas, which diffuses out of the soil and rocks and accumulates in the atmosphere, where in particular its daughters ^{214}Bi and ^{214}Pb , attaching to airborne aerosols and dust and at times can cause significant interference in the uranium signal, particularly when atmospheric inversion traps them close to the ground ([Gold et al., 1964](#); [Charbonneau and Darnley, 1970](#); [Darnley and Grasty, 1970](#); [Grasty, 1979b](#)).
- Furthermore, rain and soil moisture increases the attenuation of gamma rays and cause the fluence rate of potassium and thorium to be decreased, generally by 10% for every 10% increase in soil moisture ([Kogan et al., 1969](#)). For uranium the effect is more complicated because radon escapes more readily from drier soils ([Megumi and Mamuro, 1973](#)). In wetter soils the lower escape rate can result in a build-up of radon in the near surface and an apparent increase in uranium content ([Tanner, 1964](#); [Lovborg, 1984](#); [Grasty, 1997](#)). During rainfall the uranium signal can also increase rapidly, because daughter products of radon disintegration, attach to airborne aerosols and dust and can precipitate with the rain drops ([Charbonneau and Darnley, 1970](#)).
- Atmospheric effects such as pressure, temperature and humidity affect the density of air between source and detector and hence the attenuation of the signal. Temperature inversion can act to concentrate radon daughter particles close to the ground.
- Vegetation having dense composition can cause some shielding of radiation and may also contribute to the gamma ray flux through radioisotopes within the biomass. In heavily forested areas, tree trunks can collimate the flux of gamma rays ([Kogan et al., 1969](#); [Travassos and Pires, 1994](#)).

In order to make a general estimation of the interference sources during in-situ measurements together with the acquired spectra in situ with the NaI(Tl) and by collecting samples for measurements with the MCA_Rad system. For each site the NaI(Tl) detector was used to perform 5 minutes ground measurements in-situ. In the position where the detector was grounded one sample was collected and four more samples were collected on the side bisectors of a 2 m side square centered at the grounded position of the detector. Each sample is treated in the same way as the one collected for the efficiency calibration of the system (described in [section 3.1.1](#)). The averages of the results obtained from measurements in laboratory for each site was used as reference to be compared with the outputs of the two spectrum analysis methods.

In **Table 3.8** the correlation factor, Ω , which minimize the relative dispersion is obtained by using the following equation:

$$r = \sum_{i=1}^{80} \frac{([ZaNaI]_i - \Omega[MCA_Rad]_i)^2}{([MCA_Rad]_i)^2} \quad (\text{Eq. 3.9})$$

where, MCA_Rad and ZaNaI are referred to the radioisotopes concentrations calculated in laboratory and in situ. There is an agreement within the uncertainties between the FSA/FSA with NNLS and the window method, but it seems that the window method usually overestimates the concentration while both FSA versions go in the opposite direction. For the FSA method three different algorithms have been compared and the results are reported in **Table 3.8**: the standard FSA described in literature, the data obtained implementing the NNLS constrain in the algorithm, and the FSA with NNLS with the optimization procedure introduced in the calibration method. This way, it is possible to understand the effect on the resulting isotope concentrations for each step by using the reduced chi square, χ^2 , as reference. All results reported in **Table 3.8** agree with a factor Ω very close to 1, which guaranties the reliability of the method for all elements. The correlation for the uranium element is strongly affected by the atmospheric radon concentration at the time of the in situ measurement, although this discrepancy is within the uncertainties.

Table 3.8: the Ω coefficients averaged for all the data samples. For the WAM results the χ^2 is not shown due to absence of a fitting procedure.

	Ω (K)	Ω (U)	Ω (Th)	χ^2
WAM	1.12 ± 0.07	1.11 ± 0.10	1.00 ± 0.09	-
FSA	0.99 ± 0.06	0.78 ± 0.14	0.86 ± 0.07	1.22 ± 0.08
FSA with NNLS	1.00 ± 0.06	0.82 ± 0.13	0.92 ± 0.07	1.08 ± 0.08
FSA with NNLS opt.	1.06 ± 0.06	0.87 ± 0.12	0.94 ± 0.07	1.06 ± 0.05

The energy calibration adjustment has been included in the analysis of the measured spectra in order to correct for possible gain mismatching between the measured spectrum and the sensitive one. This problem is minimized implementing this post process correction as proven by the reduction of the χ^2 reported in **Table 3.8**. As an example, in **Figure 3.13** the measured ^{137}Cs concentrations, determined using both the standard FSA and in the FSA with NNLS methods, are reported. When the cesium abundances are low, the standard FSA algorithm introduces negative concentrations in order to have a

better fit of the spectrum shape (corresponding to the ^{137}Cs line there is also the 609 keV peak due to the ^{214}Bi).

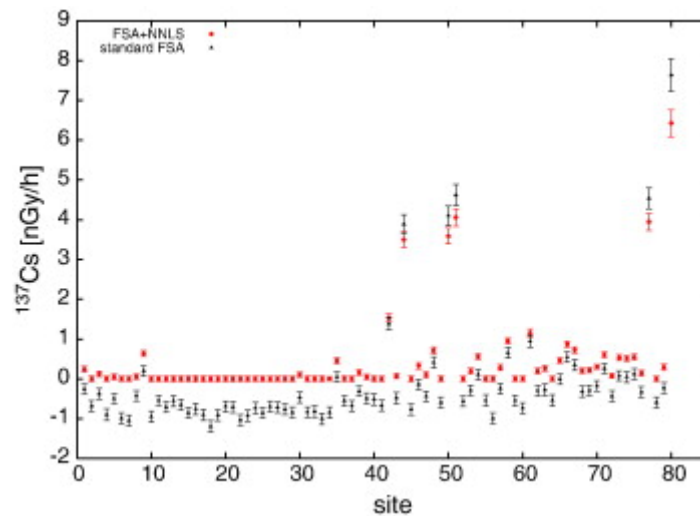


Figure 3.13: the absorbed dose in detector due to ^{137}Cs in the 80 sites, determined with the new FSA with NNLS constrain (red circles) and with the standard FSA method (black triangles). The new algorithm avoids the negative counting and it reduces at the same time the uncertainties.

Introducing the NNLS and the gain drift, the quality of fits is improved by 10% in average as shown in **Table 3.8**. The correlation between the in situ measurements, analyzed by the FSA+NNLS, and the MCA_Rad measurements for all 80 sites are reported in **Figure 3.14**, **3.15**, and **3.16**. The uncertainty reported on the MCA_Rad is the standard deviation of the average calculated over the five collected samples.

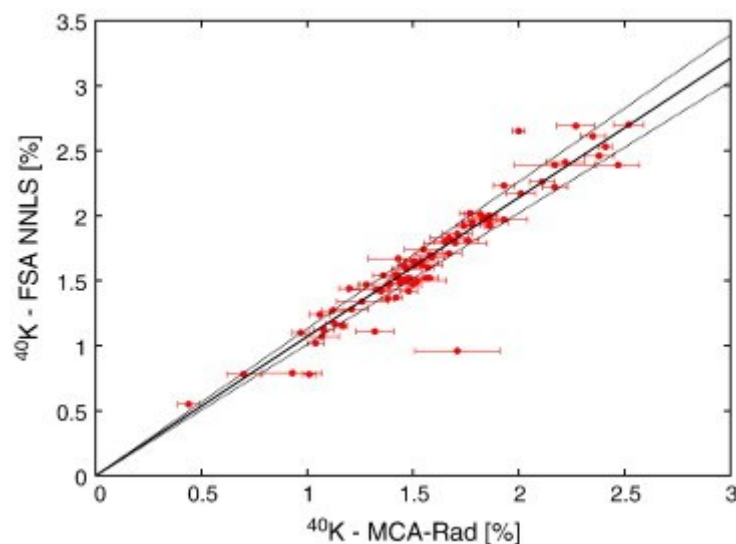


Figure 3.14: the potassium concentration measured with MCA_Rad system (HPGe) and with ZnNaI system (using FSA with NNLS method) are plotted together. The average of five soil samples with relative uncertainty is plotted for the MCA_Rad

analysis. No errors are associated with the ZnAI data. The linear correlation line associated with the Ω value is shown (full line) with 1σ error (dashed line).

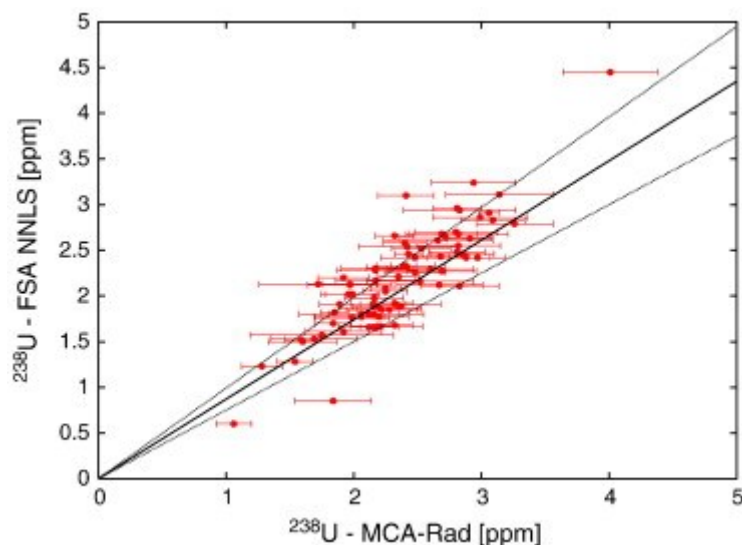


Figure 3.15: the uranium concentration measured with MCA_Rad system (HPGe) and with ZnAI system (using FSA with NNLS method) are plotted together. The average of five soil samples with relative uncertainty is plotted for the MCA_Rad analysis. No errors are associated with the ZnAI data. The linear correlation line associated with the Ω value is shown (full line) with 1σ error (dashed line).

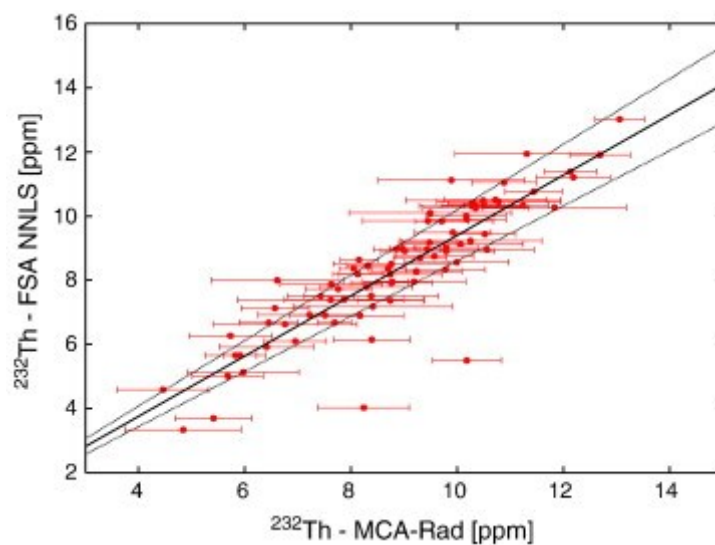


Figure 3.16: the thorium concentration measured with MCA_Rad system (HPGe) and with ZnAI system (using FSA with NNLS method) are plotted together. The average of five soil samples with relative uncertainty is plotted for the MCA_Rad analysis. No errors are associated with the ZnAI data. The linear correlation line associated with the Ω value is shown (full line) with 1σ error (dashed line).

The uncertainties on the Ω factors are used as systematic uncertainties on the concentration measurements with the sodium iodide, since they contain both the contribution from the non

homogeneity of soil ground and the systematic due to the analysis algorithm. The uncertainties found in this way are: 5% for the potassium, 14% for the uranium and 7% for thorium, which are smaller than the ones requested for outdoor in situ studies, for civil and also geological purposes.

Chapter 4

Airborne γ -ray spectrometry: a geostatistical interpolation method based on geological constrain for radioelement mapping



Survey using AGRS_16.0L airborne gamma-ray spectrometer in Tuscany Region.

- 4.1 **A self-made airborne gamma-ray spectrometer**
 - 4.1.1 *AGRS system: set-up*
 - 4.1.2 *Calibration and radiometric data processing*
- 4.2 **The first airborne gamma-ray survey in Italy: case of study Elba island**
 - 4.2.1 *Brief geological settings*
 - 4.2.2 *Airborne survey: summary of the results*
- 4.3 **Radioelement mapping using geostatistical approach**

Chapter 4

Airborne γ -ray spectrometry: a geostatistical interpolation method based on geological constrain for radioelement mapping

4.1 A self-made airborne gamma-ray spectrometer

4.1.1 AGRS system: set-up

The AGRS_16.0L is a modular scintillation gamma-ray spectrometry system composed by four sodium iodide detectors (dimensions 10 cm x 10 cm x 40 cm) and a total volume of about 16L. The detectors are coupled with photomultiplier tube (PMT) base which manage also the HV bias supply. The four individual signals are processed by an integrated electronic card, TNT2 CAEN N1728B (4 channel, 100MHz, 2 FPGA) which permits the acquisition in "list mode" (event by event). The system is further equipped with an addition scintillation gamma-ray spectrometer NaI(Tl) (dimensions 10 cm x 10 cm x 10 cm) placed on top of the other four (**Fig. 4.1**). This additional detector called also "radon monitor" is considered following IAEA guidelines ([IAEA TRS No.323, 1991](#)) for the monitoring and correction during flights of radon gas in atmosphere using the "upward looking method" (described later). The radon monitor is coupled with a PMT base with integrated bias supply, preamplifier and digital multichannel analyzer. The output signal is recorded in pulse height spectra integrated within the defined time interval.

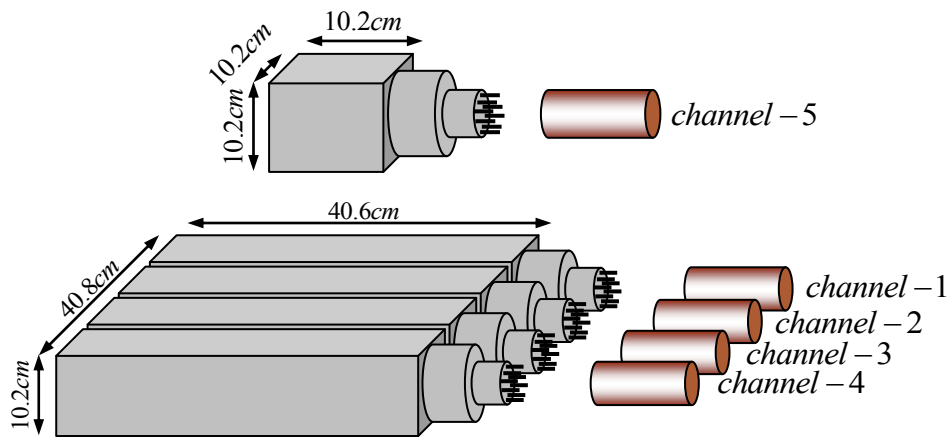


Figure 4.1: schematic design of AGRS_16.0L composed by four scintillation NaI(Tl) detectors of dimensions 10 cm x 10 cm x 40 cm each and one scintillation NaI(Tl) detectors of dimension 10 cm x 10 cm x 10 cm.

The system is also equipped by other auxiliary instruments like GPS antenna (GARMIN GPSmap 60C) and Pressure and Temperature sensors (DeltaOhm HD 9022 devices). The GPS antenna (54 channel) reaches 10 m spatial accuracy on global positioning and is used in flight to record the position of the AGRS_16.0L system (in WGRS-84 coordinates) during radiometric data acquisition. The real time altitude above ground of the AGRS_16.0L system is calculated combining in the barometric (Laplace) formula the atmospheric pressure (in mbar) and temperature (in °C) measured with two sensors having an accuracy of 0.2 mbar and 0.1°C, respectively. The GPS data, together with temperature and pressure data are recorded every seconds. The power supply needed by the system is provided by set of four batteries (12 V each). All the acquisition is controlled by a netbook which also provides the flight information to the pilot (in terms of direction, velocity and altitude), allowing to follow the scheduled flight plan.



Figure 4.2: final configuration of AGRS_16.0L system.

The system is mounted on a ultra light vehicle, called autogiro (**Figure 4.2**), which consist in a convenient compromise between transportable weight and flight costs. The cruise speed of about 100

km/h of this vehicle are well comparable with the nominal speed commonly required for airborne gamma-ray spectrometry surveys. In [figure 4.3](#) are described the hardware/software and output for the AGRS_16.0L system.

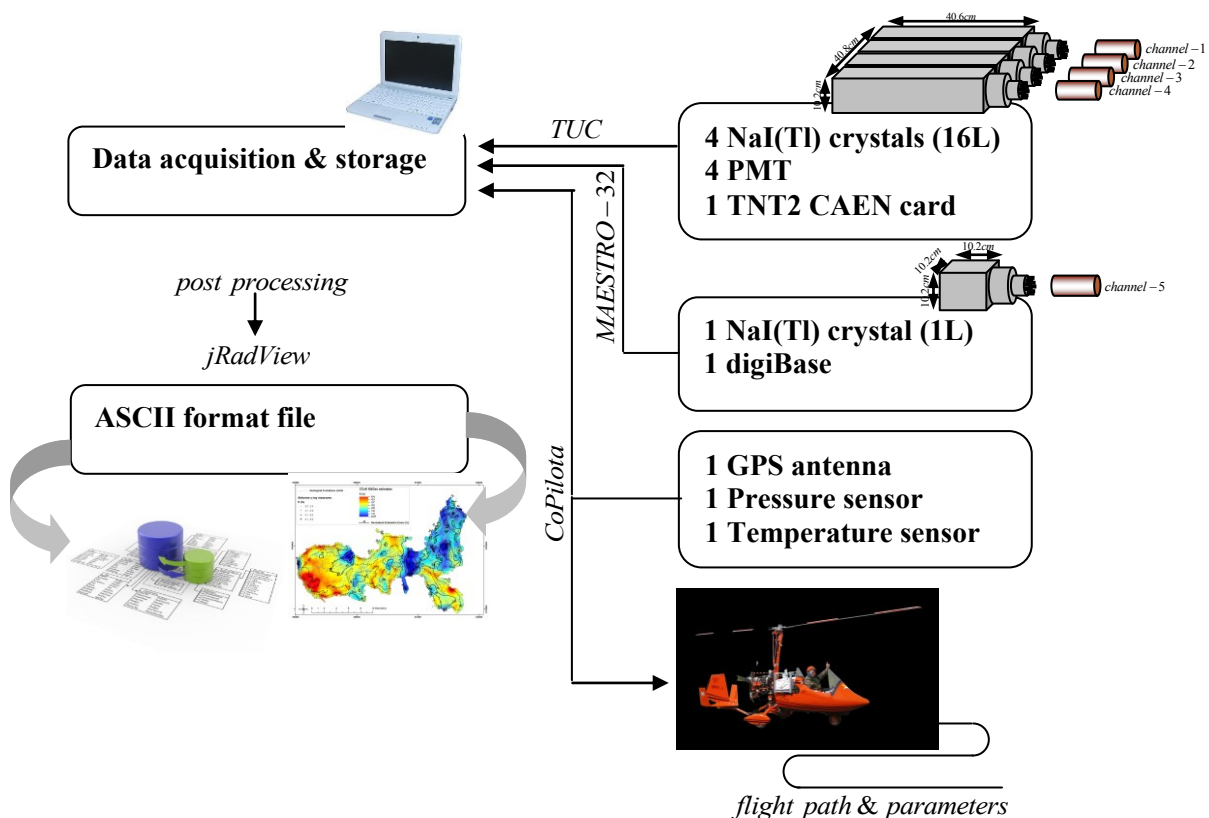


Figure 4.3: schematic design of hardware/software and output for AGRS_16.0L system.

4.1.2 Calibration and radiometric data processing

The full spectrum analysis (FSA) method with non-negative least square (NNLS) constrain described in [chapter three](#) was extended also for airborne spectrum analysis. According to the calibration method (described in [chapter three](#)) the same of naturally occurring sites used to calibrate the ZaNaI_1.0L is used for the calibration of the AGRS_16.0L. Remember that each site is accurately characterized for the radioactivity distribution of the area compatible with the field of view of the system (about 10 m of radius). The system was systematically placed on ground (for example see [Fig. 4.4](#)) where field measurements are done. Differently from the procedure described previously here is of relevant implication the distortion introduced by the air in the spectra shape acquired at the calibration process and those recorded during airborne survey at different altitudes. Here is not discussed again the mathematical approach for the calibration procedure, since similar with that discussed in [chapter three](#), while radiometric data processing is described in details. In [figure 4.5](#) are

reported the sensitivity spectra obtained for the AGRS_16.0L system. The only difference comparing to the sensitivity spectra obtained for ZaNaI_1.0L is that they are reconstructed in the energetic range between 450 - 2900 keV, cleaning the spectra from scattered gamma-rays recorded in the low energy range.



Figure 4.4: example of a natural calibration site (GC1 see [table 3.3](#))

The radiometric data registered with AGRS_16L system consist of recorded events from the main detector (four NaI(Tl) detector pack of 16 L volume) and recorded spectra from radon monitor (1L NaI(Tl) detector). Auxiliary instruments (GPS antenna and Pressure and Temperature sensors) register the flight parameter (position, height and velocity) synchronized with radiometric data using the time stamp.

Firstly, the radiometric data acquired in list mode are subject to spectra reconstruction. The events registered in each of four NaI(Tl) detectors recorded separately in individual channels are calibrated energetically and the spectra are reconstructed within the chosen time interval. The energy calibration is cross-checked by measuring a portable gamma-ray source at the start and at the end of each flight. Finally, the single spectra are summed and analyzed by the Full Spectrum Analysis (FSA) with NNLS constrain approach as described by [Cacioli et al. 2012](#). The results obtained are subject to three corrections (1) subtraction of cosmic and aircraft background, (2) atmospheric radon subtraction for uranium (3) attenuation due to different variations from nominal flying height, before the conversion of counts to ground concentrations using sensitivities.

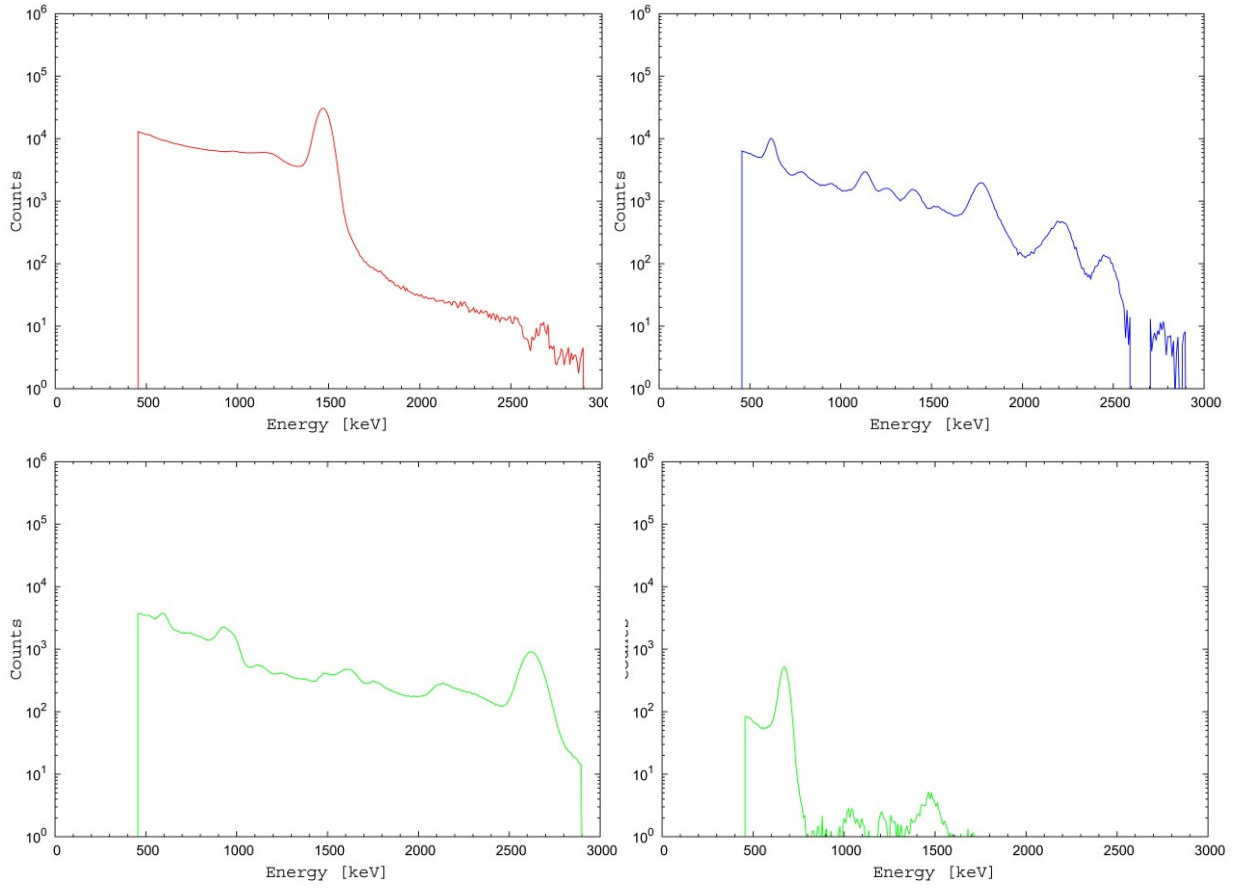


Figure 4.5: Sensitivity spectra obtained using FSA with NNLS constrain method for the AGRS_16.0L system.: potassium sensitivity spectra (up-left), uranium sensitivity spectra (up-right), thorium sensitivity spectra (down-left) and cesium sensitivity spectra (down-right).

Following IAEA guidelines ([IAEA TECDOC 1636, 2003](#), [IAEA TRS No.323, 1991](#)) the correction due to cosmic and aircraft background is done by performing flight over large water surfaces where there is a low atmospheric radon for different flying heights from 1 - 3.5 km (recommended). The measured spectra are each the sum of the aircraft component (constant) and the cosmic component. Also, the count rate in the 3-6 MeV cosmic window is linearly related to the count rate in the i 'th energy channel. Thus, a linear regression of the cosmic window count rate on any other particular channel yields the cosmic sensitivity (slope of regression line) and aircraft background (zero intercept) for that channel as follows.

$$n_i = a_i + b_i n_{\text{cosmic}} \quad (\text{Eq. 4.1})$$

where n_i is the aircraft and cosmic background count rate in the i 'th channel, n_{cosmic} is the cosmic window count rate, a_i is the aircraft background in the i 'th channel and b_i is the background in the i 'th

channel normalized to unit counts in the cosmic window. In our case, the correction due to cosmic and aircraft background is performed to full spectrum by averaging both contributions with the background spectra obtained during the calibration process.

The flight parameters are characterized by the height and speed of the aircraft determining the line space of the survey pattern. Even the flight speed and height of 100 km/h and 100 m respectively are conventionally chosen as nominal flight parameters for radioactivity monitoring (for a line space distance of 500 m) the vehicle does not always flight at this altitude. The real time position recorded through GPS antenna and pressure and temperature recorded through the respective sensors are integrated together and used to extract from the digital elevation model (DEM) the altitude above ground during flight. Knowing the elevation over the sea at the starting flight position (SFP) the real time (current flight position, CFP) altitude is calculated using the barometric (Laplace) formula, where aircraft (measure) altitude is deduced from the height difference, dH between the SFP and CFP is given by:

$$dH = \log_{10} \left(\frac{P_{SFP}}{P_{CFP}} \right) \times 18400 \times 1.00157 + 0.001835 \times (T_{SFP} + T_{CFP}) \quad (\text{Eq. 4.2})$$

where P and T are the values of pressure and temperature during survey related with the start and current flight positions measured in mbar and °C respectively. Furthermore, in order to consider the weather variations during survey, at the start flight position (SFP) are continuously monitored the pressure and temperature. The linear interpolation of this records is used to correct the altitude above ground.

The well determination of the aircraft (measurements) altitude play an important role on association of the radioactivity concentration to the investigated area and for the correction of the topography effect following the method described by [Schwarz et al. 1992](#). In this method the digital elevated model (DEM) is used. Firstly the data are leveled at nominal altitude (100 m), where for one second time interval the algorithm calculates the ratio of the fluence integral at the real flight altitude and that at 100 m nominal altitude. The calculated ratio is averaged over the chosen investigation time interval (if higher than one second) and than used to corrected for flying altitude. The algorithm takes into account also the fraction of water surfaces in calculating the fluence integral: this procedure is important when assigning the radioactivity concentration to close/over to sea or lake shore surveys. Finally, the data leveled at nominal altitude (100 m), $C_i^{nominal}$ for the radioelement i (when i equal to ^{40}K , eU, eTh and ^{137}Cs) are reported to ground level, C_i^{ground} using the following relationship:

$$C_i^{ground} = \left[0.75 \exp\left(-\frac{H_{nominal}}{2H_i}\right) + 0.25 \sqrt[3]{H_{nominal}} \right] C_i^{nominal} \quad (\text{Eq. 4.3})$$

where $H_{nominal}$ is the nominal altitude (taken equal to 100 m) and H_i is the altitude when the signal decrease as $1/e$ with respect to the ground level (this parameter is different for each radioelement).

It is well known that radon (^{222}Rn) gas diffused out from soil or rocks can accumulate in the atmosphere when its daughter, particularly ^{214}Bi and ^{214}Pb can attach to airborne aerosols and dust which can cause a significant interference in the uranium signal. This situation can be critical in particular weather conditions which favor the lowering of the atmospheric inversion traps (like temperature inversion layer) close to ground significantly increasing in this way the concentration of radon gas ([Darnley and Grasty, 1970](#); [Grasty, 1979b](#)). Furthermore, rain and soil moisture can affect significantly the signal of uranium since in wetter soils the lower escape rate can result in a build-up of radon in the near surface and an apparent increase in uranium content ([Lovborg, 1984](#); [Grasty, 1997](#)).

As described in [section 4.1.1](#) the AGRS_16.0L is equipped with a 1L scintillation gamma-ray spectrometer partially shielded from ground and used to monitor the variation of the signal coming from the atmosphere: the "up-warding detector" method is adopted following IAEA guidelines ([IAEA TECDOC 1636, 2003](#), [IAEA TRS No.323, 1991](#)). According to this method the count rate recorded from radon monitor (during flight) can be expressed as following:

$$CR = \alpha K + \beta(U + Rn_{16L}) + \gamma Th + \delta Rn + BG \quad (\text{Eq. 4.4})$$

where K , U , Th are the ground radioelement concentrations recorded by the main detector (16L NaI(Tl) detector) and α , β , γ are the respective efficiency factors which consider their contribution in radon monitor (1L NaI(Tl) detector) spectrum. Although the radon monitor is shielded by the main detectors and the battery pack, part of the signal coming from the gamma-rays emitted from ground natural radioelements contribute to the recorded spectrum. While Rn is the radon concentration in air and δ is the efficiency and BG is the intrinsic background of the monitor detector. Finally, Rn_{16L} is introduced to take into account the radon signal detected from the main detector.

According to IAEA guidelines the efficiency coefficients can be determined by performing an accurate calibration procedure near to extended water surfaces: flight lines are designed perpendicular to the shore passing from ground to water in order to valuate the contribution from ground and from

atmospheric radon. In our case the survey of Elba island was used as self calibration survey for atmospheric radon survey. The δ coefficient is extracted from the fraction of flight over sea water realized during the flight from peninsula to the island and in return. While the ground contribution (α , β , γ coefficients) were determined by fitting over 1000 ground measurements considering δ as constant (during flight) and knowing the intrinsic background contribution, BG. This consideration is cross-checked and resulting reasonable through the data obtained from peninsula to the island and in return. The contribution of atmospheric radon gas calculated from this equation (Eq. 4.4) is subtracted to the uranium concentration obtained from the analysis with FSA with NNLS constrain. The ground leveling described above is performed after this correction, only.

In **Table 4.1** are summarized the uncertainty sources for the radiometric data processing method.

Table 4.1: uncertainty sources associated to radiometric data measured using AGRS_16.0L system.

Uncertainty source		Relative uncertainty
altitude distortion of sensitivity spectra		< 10%
cosmic and background correction		2%
altitude correction (data leveling)		< 8%
atmospheric radon gas correction		5% ^a
spectrum analysis method (FSA with NNLS constrain)	⁴⁰ K	5%
	eU	15%
	eTh	7%
acquiring statistics		< 20% ^b

^a applied only to eU concentrations

^b average uncertainty estimated from over 1000 spectra measured in Elba island

4.2 The first airborne gamma-ray spectrometry survey in Italy: case of study Elba island

4.2.1 Brief geological setting

Elba is the biggest island of the Tuscan Archipelago and is located in the northern part of the Tyrrhenian Sea between Italy and Corsica Island (France). It is the westernmost outcrop of the Northern Apennines mountains chain (**Figure 4.6**).

The geological distinctive features of this island (**Figure 4.7**) are linked to its complex tectonic pile of nappes and to the well-known Fe-rich ores, as well as to the well-exposed interactions between

Neogene magmatic intrusions and tectonics (Trevisan, 1950, 1951; Barberi et al., 1969; Keller and Piali, 1990; Bortolotti et al., 2001; Tanelli et al., 2001). The structure of Elba Island consists of thrust sheets stacked during an earlier late Cretaceous to early Miocene Apennine compressional phase. These thrust sheets are cross-cut by later mid-Miocene to early Pliocene extensional faults (Jolivet et al., 1998; Bartole, 1995; Bartole et al., 1991; Keller and Piali, 1990; Trevisan, 1950).

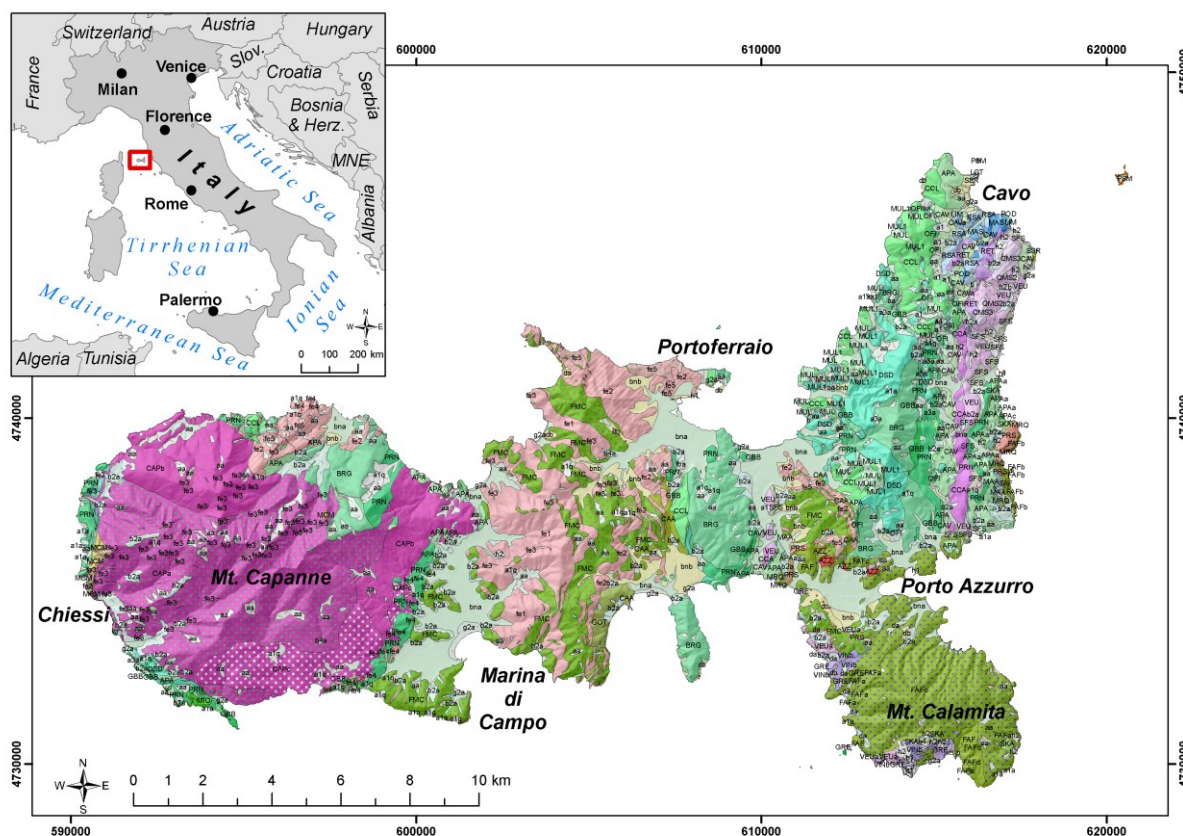


Figure 4.6: geological map of Elba Island (taken from the new Geological Map of Tuscany region realized at 1:10,000 scale, see CGT, 2011): the western sector is mainly characterized by intrusive igneous rocks (magenta), the central and eastern parts of the island are characterized by a wide lithological variation (green, purple and pink), while the southeastern outcrop almost exclusively consists of metamorphic rocks (Mt. Calamita). For the official legend of all the geological formations see <http://www.geologiatoscana.unisi.it>. Coordinate system is UTM WGS84 Zone 32 North.

The tectonic building of Elba Island is composed of a structural pile of at least five main units called "Complexes" of Trevisan" (TC), Trevisan (1950): the lowermost of them belong to the three Tuscan Domain, while the uppermost two relate to the Ligurian Domain. Bortolotti et al. (2001) performed 1:10,000 mapping of central-eastern Elba and proposed a new stratigraphic and tectonic model in which the five TC were reinterpreted and renamed (Figure 4.7). TC will be shortly described below.

The Porto Azzurro Unit (TC I) consists of Paleozoic micaschists, phyllites and quartzites with local amphibolitic horizons, as well as Triassic-Hettangian metasiliciclastics and metacarbonates. Particularly, in the Porto Azzurro area and in the eastern side of Mt. Calamita the micaschists are typically cross-cut by the aplitic and microgranitic dykes that swarm from La Serra-Porto Azzurro monzogranitic pluton (5.1-6.2 Ma).

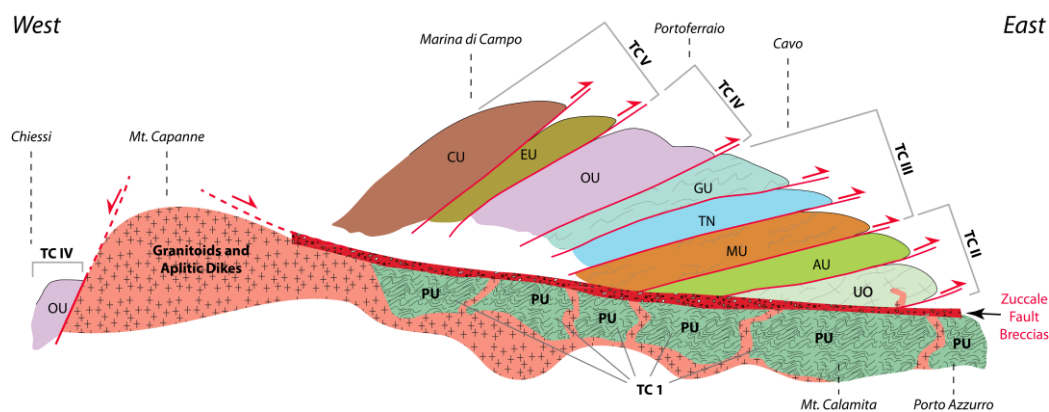


Figure 4.7: Elba tectonic vertical sketch from western to eastern coastline. This scheme shows TC structural pile, and toponyms are roughly located in the corresponding tectonics units where they lay: PU - Porto Azzurro Unit, UO - Ortano Unit, AU - Acquadolce Unit, MU - Monticiano-Roccastrada Unit, TN - Tuscan Nappe, GU - Grassera Unit, OU - Ophiolitic Unit, EU - Palaeogene Flysch Unit, CU - Cretaceous Flysch Unit. Modified from [Bortolotti et al. \(2001\)](#).

The Ortano Unit (lower part of TC II) includes phyllites and quartzites porphyroids and porphyritic schists, and phyllites, with quartzitic metasandstones and metaconglomerates on the top. Also this unit suffered of thermometamorphic recrystallization due to the Serra Porto Azzurro intrusion. The Acquadolce Unit (upper part of TC II) is made of locally dolomitic massive marbles, grading upwards to calcschists. This lithology is capped by a thick siliciclastic succession. The Mio-Pliocene thermometamorphic imprint is also evident.

The Monticiano-Roccastrada Unit (lower part of TC III) includes basal fossiliferous graphitic metasediments of Late Carboniferous-Early Permian age, unconformably overlain by the detrital Verrucano succession (Middle-Late Triassic). The Tuscan Nappe Unit (central part of TC III) is represented by calcareous-dolomitic breccias, northwards the overlying carbonatic outcrops. Most of Grassera Unit (upper part of TC III) is made of varicolored slates and siltstones with rare metalimestone or meta-chert intercalations, basal calcschists also occur.

The Ophiolitic Unit (TC IV) is composed by several minor thrust sheets or tectonic sub-units, which are characterized by serpentinites, opihalcites, Mg-gabbros, and by the Jurassic-Lower Cretaceous sedimentary cover ([Bortolotti et al., 2001](#)).

The Paleogene Flysch Unit (lower part of TC V) mainly consists of shales, marls with limestone, sandstone and ophiolitic breccia intercalations including fossils of the Paleocene-Eocene age. Lower-Upper Cretaceous Flysch Unit (upper part of TC V) consists of basal shales and varicoloured shales. These lithologies vertically pass to turbiditic siliciclastic sandstones and conglomerates, which in turn alternate with marlstones and marly limestones. Both Flysch Units were intruded by aplitic and porphyritic dykes and laccoliths about 7-8 Ma ([Dini et al., 2002](#)) ago.

The geological structure of the island allows a nearly complete representation of lithologies present in the whole Northern Apennines mountains chain ([Figure 4.6](#)). This feature makes Elba Island quite varied and complex in terms of both geological formations and lithologies. Therefore, it can be considered as a formidable research site for studying interactions between lithologies possessing different radioactive content and the AGRS method.

4.2.2 Airborne survey: summary of the results

Airborne gamma-ray spectrometry (AGRS) method is widely considered as an important tool for mapping environmental radioactivity both in geosciences studies and for purposes of emergency response ([Grasty, 1975](#); [Sanderson et al., 2004](#); [Scheib and Bemish 2010](#); [Minty, 2011](#)). By using a typical cluster of the airborne scintillation gamma-ray spectrometer, AGRS_16.0L system was used for the natural radioactivity monitoring of Elba island. According to IAEA guidelines ([IAEA TECDOC No.1363, 2003](#)) the survey strategy was planned to be as perpendicular as possible to the geological structure of the area ([Figure 4.6](#)), in which a nord-to-south orientation occurs. Therefore, flight lines were designed in a helicoidally form, constrained by the morphological structure of the terrain (elevations going from 0 to 1010 m a.m.s.l.), starting from the shore line and following the heights of the mountain in counter clock direction. The unique region not properly covered by the airborne gamma-ray survey is the top of Monte Capanne, because of the cloudily weather conditions. For radioactivity monitoring purpose the survey parameters can be properly chosen to have a nominal altitude of 100 m and a cruiser speed of about 100 km/h with space lines at maximum 500 m distant from each-other. The measured altitude during flight record values within 140 ± 50 m (from minimum 40 m to maximum 400 m), considered satisfactory for the morphology of the island. For these flight conditions the AGRS_16.0L system is able to measure the 97% of the signal coming from a ground

area of about less than 600 m of radius (640 ± 110 m), even if the major contribution (90%) comes from half of this area.

The signal is acquired in list mode (event by event) using an integrated electronic module with four independent signal processing channels (TNT2 CAEN Module) and then analyzed off-line in 10 seconds time slices. The time interval is chosen in order to reduce the statistical uncertainty to less than 10%. The gamma-spectra are calibrated and analyzed by using the FSA approach with NNLS constrain as described in [Cacioli et al. 2012](#). Several corrections described above are applied to the measured signal at different flight altitudes in order to determine the concentration at the ground. The topology of the ground surface has been taken into account, by using the Digital Elevation Model of Tuscany, which has a 10m spatial resolution. The effects of topography are corrected following the method described by [Schwarz et al. 1992](#). Finally, this signal is corrected through the [equation. 4.3](#) in order to obtain the concentration on the ground surface. The altitude and topography corrections introduce a total systematic uncertainty of the order of 8% in the final results.

Further corrections are required for equivalent uranium concentration, eU, since the signal coming from ground uranium is affected by the presence of radon gas in the air: it is evaluated by using the "upward looking" detector method, following the procedure described in [IAEA TRS No.323, 1991](#). The atmospheric radon concentration is estimated by analyzing the whole spectrum acquired with the "upward looking" detector which is calibrated by flying over the Tyrrhenian sea at the beginning and at the end of the survey. The radon concentration has been calculated for each time interval and it has been found almost constant during the entire flight (0.2 ± 0.1 ppm). Since the ground abundance of eU varies from 0.1 ppm up to 30.0 ppm over the entire Elba island, the relative uncertainty concerning the radon subtraction for each single measurement varies from 2% up to 75% with an average value of 23%.

As described in [Cacioli et al. 2012](#), the calibration method is based on the ground acquisition of standard spectra. Therefore a distortion is expected in the spectra acquired at different altitude because of the air. This effect has been estimated by Monte Carlo (GEANT4) simulation and it introduces a systematic uncertainty of about 10%.

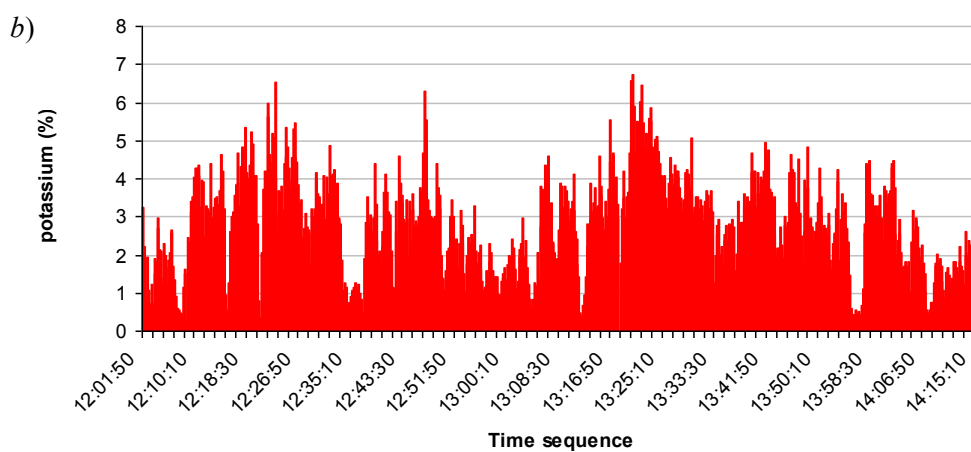
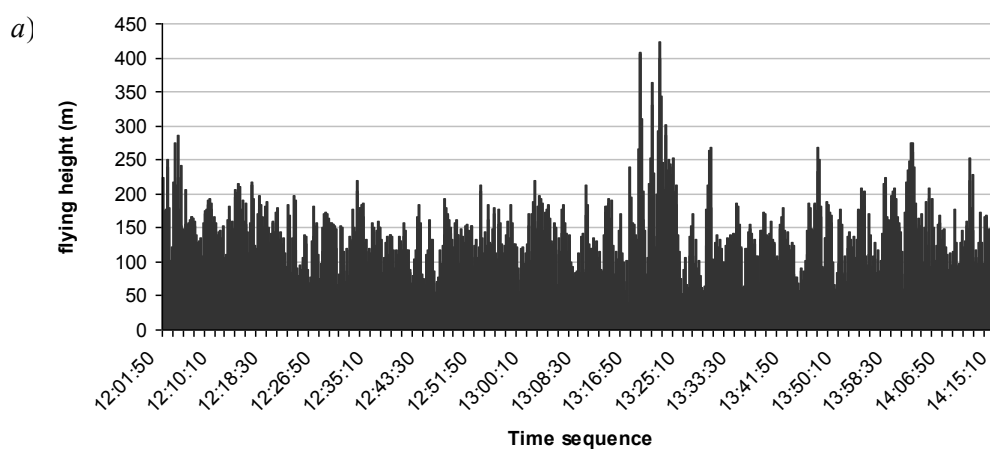
Uncertainties of the final results are reported in [Table 4.2](#). However, we emphasize that data used as input in the geostatistical interpolators are taken into account without experimental uncertainties and that their position is related to the centre of the investigated area.

Table 4.2: experimental uncertainties for the measured radioelement concentrations.

Radioelement	Average statistical uncertainty	Average systematic uncertainty
^{40}K	7%	14%
eU	15%	20% ^a
eTh	20%	15%

^a includes the uncertainty related to correction due to atmospheric radon gas.

About 800 radiometric data (^{40}K , eU and eTh abundances) are recorded over Elba island distributed in irregular grids. In **figure 4.8 a, b, c** and **d** are shown detailed profiles of altitude recorded during flight and respective potassium, uranium and thorium abundances.



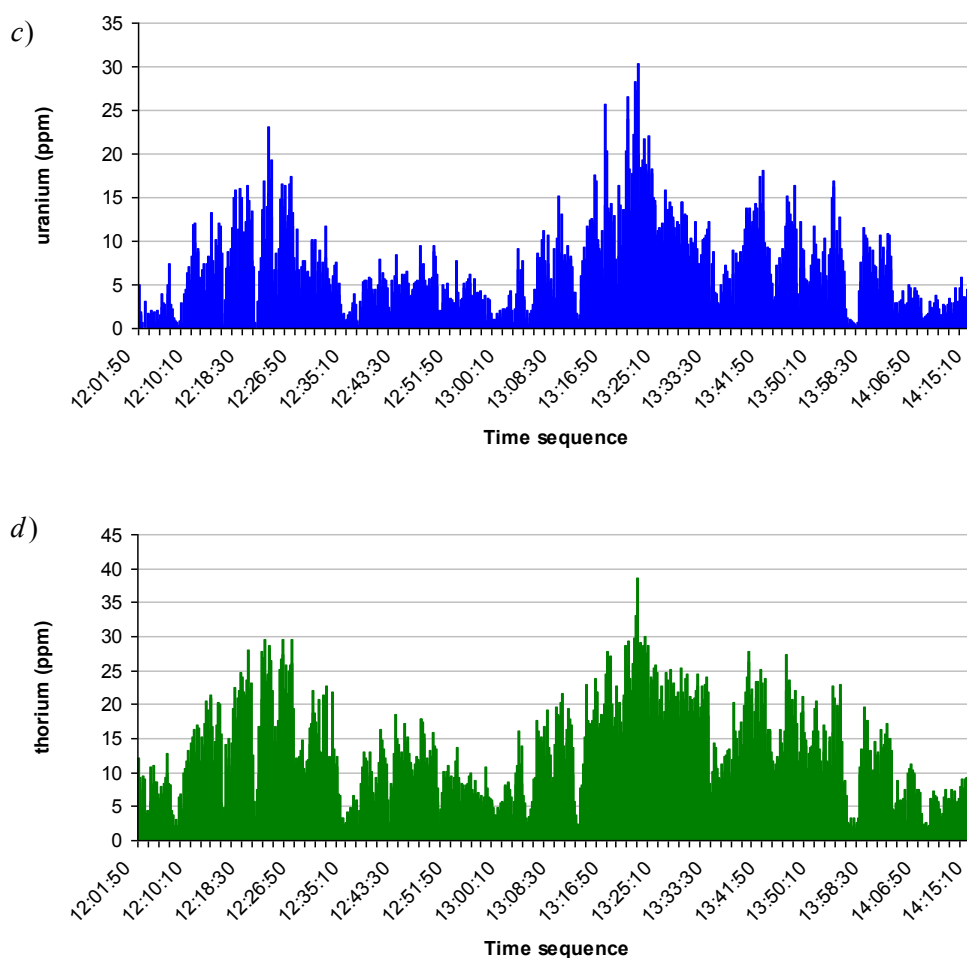


Figure 4.8: a) altitude profile recorded during flight, b) potassium abundances profile, c) uranium abundance profile and d) thorium abundance profile.

4.3 Radioelement mapping using geostatistical methods

Geostatistics deals with spatial datasets predicting distributions that characterize the coregionalization between the variables. Collocated cokriging is a special case of cokriging, where a secondary variable available at all prediction locations is used to estimate a primary under-sampled variable, restricting the secondary variable search in a local neighborhood. Frequently, primary and ancillary (secondary) variables are sampled by different supports, measured at dissimilar scales, organized in unlike sampling schemes making the spatial prediction more complex. The integration of data which can be different in terms of types, reliability, scales, has been studied in several works. In (Babak and Deutsch, 2009), for instance, this approach is adopted by using dense 3D seismic data and test data for an improved characterization of reservoir heterogeneities. This approach is also used for mapping soil organic matter (Pei et al., 2010), rainfall or temperature over a territory (Goovaerts, 1999; Hudson

and Wackernagel, 1994), , for estimating environmental variables like pollutants or water table (Guastaldi and Del Frate, 2011; Pardo-Iguzquiza and Dowd, 2005; Desbarats et al., 2002; Hoeksema et al., 1989), as well as for mapping geogenic radon gas in soil (Buttafuoco et al., 2010). Currently, there is a lack of applications of this method to airborne gamma-ray measures integrated with geological information. Besides, both fieldwork and laboratory measures of natural radioactivity in rocks and soils suggest a tight correlation between gamma-ray abundances and geological formations (Cacioli et al., 2012). Hence, a multivariate technique for interpolating airborne gamma-ray data on the basis of the geological map information is desirable.

We used the collocated cokriging as multivariate estimation method for the interpolation of primary under-sampled airborne gamma-ray data using the constrain based on the secondary well-sampled geological information. In this section is briefly described the theoretical background of collocated cokriging interpolation method and its application to airborne gamma-ray data using the geological constrain.

Collocated cokriging: theoretical background

Geostatistical interpolation algorithms build up probability distributions that characterize the present uncertainty by means of coregionalization between the variables (Wackernagel, 2003). Collocated cokriging is an interpolation method for dealing with a primary under sampled variable $Z_1(x)$ and a secondary widely sampled variable $Z_2(x)$, maybe continuously known at all grid nodes (Goovaerts, 1997).

Xu et al. (1992) advanced a definition strategy in which the neighborhood of the auxiliary variable $Z_2(x)$ is arbitrarily reduced to the target estimation location x_0 only (Wackernagel, 2003). They formulated CCoK as a simple cokriging linked to the covariance structure (Chiles and Delfiner, 1999):

$$\rho_{12}(h) = \rho_{12}(0)\rho_{11}(h) \quad (\text{Eq. 4.5})$$

where $\rho_{11}(h)$ is the correlogram of the primary variable Z_1 and $\rho_{12}(h)$ is the cross-correlogram of Z_1 and Z_2 , which is the spatial correlation between the primary and the secondary data at a distance h .

By assuming $Z_1(x)$ to be known, the value of the primary Z_1 at target location x_0 is independent of the value of the secondary variable Z_2 , if Z_1 and Z_2 have the mean equal to zero and the variance equal to

one. In this case, called "Markov-type" model, the cross covariance functions are proportional to the covariance structure of the primary variable (Xu et al., 1992; Almeida and Journel, 1994). The CCoK estimator Z_{1CCoK}^{**} at target location x_0 depends on both linear regression of the primary variable Z_1 with Z_1 and Z_2 and the simple kriging variance σ_{SK}^2 , for $\rho = \rho_{12}(0)$ as follows (Chiles and Delfiner, 1999):

$$Z_{1CCoK}^{**}(x_0) = \frac{(1-\rho^2)Z_1^*(x_0) + \sigma_{SK}^2 \rho Z_2(x_0)}{(1-\rho^2) + \rho^2 \sigma_{SK}^2} \quad (\text{Eq. 4.6})$$

where Z_1^* is the kriging estimation of Z_1 at the target location x_0 , and the accuracy of the CCoK estimation is given by:

$$\sigma_{CCoK}^2 = \sigma_{SK}^2 \frac{(1-\rho^2)}{(1-\rho^2) + \rho^2 \sigma_{SK}^2} \quad (\text{Eq. 4.7})$$

Interpolating airborne gamma-ray data on geological constraints

In our study, we used the collocated cokriging (CCoK) as multivariate estimation method for the interpolation of airborne gamma-ray data on the basis of the geological map information. The primary variable $Z_1(x)$ refers to the discrete distribution of natural abundances of K, eTh, or eU measured via airborne gamma-ray spectrometry, while the secondary variable $Z_2(x)$ refers to the continuous distribution of the geological formation. In this work, these two sets of information are independent of each other.

Data gained through airborne gamma-ray spectrometry define a radiometric spatial dataset integrating sample points position with natural abundances of potassium (%), uranium (ppm) and thorium (ppm), together with their respective uncertainties. While the geological map at 1:10,000 scale (CGT, 2011) covers the whole area in details, based on geological field survey. Moreover, the detailed geological map used lists 73 different geological formations defining in this way a categorical variable. For such a large number of variables, the approach based on categorical variables (indicator kriging) (Hengl et al., 2007; Pardo-Iguzquiza and Dowd, 2005; Goovaerts, 1997; Bierkens and Burrough, 1993; Journel, 1986) requires a long time for processing and interpretations. Therefore, we had to consider the geological qualitative (categorical) map as a quasi-quantitative constraining variable. Indeed, we randomly assigned a progressive number to each category of geological map by sorting geological

formations in alphabetic ascending order without any stratigraphic meaning. As we show in the following section, this choice does not affect the final interpolation results. Thereby, we spatially conjoined the airborne gamma-ray measures to the geological map. This migration of geological data from the continuous grid (the geological map) to the sample points (the airborne gamma-ray measuring locations) aims to get a multivariate point data set to be interpolated by means of collocated cokriging.

As shown in (Table 4.3), K (%) abundances have a quasi-Gaussian distribution, while eTh (ppm) and eU (ppm) abundances distributions tend to be positively skewed. Linear correlation is high between pairs of abundance variables. On the ground of the previous assumptions, the linear correlation coefficient between radioactivity measures and values randomly assigned to geological formations is meaningless (Figure 4.9).

Table 4.3: descriptive statistical parameters of airborne radiometric values.

Variable	K (%)	eU (ppm)	eTh (ppm)
Count	799	799	799
Minimum	0.1	0.1	0.70
Maximum	6.73	30.30	38.52
Mean	2.74	6.87	13.01
Std. Dev.	1.27	4.87	6.87
Variance	1.63	23.72	47.15
Variat.C	0.47	0.71	0.53
Skewness	0.14	1.12	0.46
Kurtosis	2.64	4.67	2.54

The CCoK interpolation models, both for the direct spatial correlation and the cross-correlation of these regionalized variables were obtained by calculating experimental semi-variograms (ESV) and experimental cross-semivariograms (X-ESV), and interpreting the models by taking into account factors conditioning the spatial distribution of these regionalized variables. Analysis was performed on raw data, even if they do not have exactly Gaussian distribution (Figure 4.9). The substantial absence of outliers in abundance distributions, as well as non-erratic ESVs and X-ESVs styles allowed us to keep original raw data without transforming them in Gaussian space. In the case of eU, we observed a moderately skewed distribution, probably due to the high experimental uncertainties (Table 4.3): the effect of these outliers are not critical and they are weakened by high statistics.

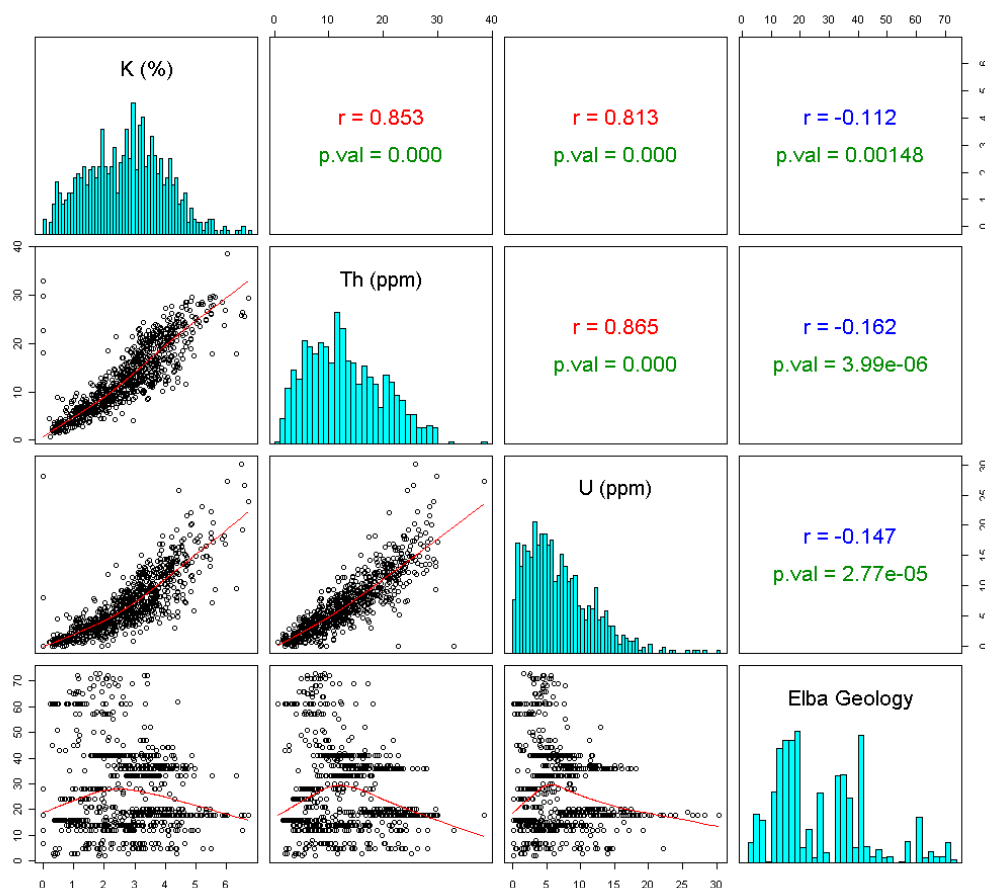


Figure 4.9: correlation matrix for group PPP variables: the lower panel shows the joint frequencies diagrams for each couple of variables and the robust locally weighted regression (Cleveland, 1979); cells on the matrix diagonal show the univariate distributions; the upper panel shows both correlation coefficient value for each bivariate distribution (blue low linear correlation, green small correlation, red high correlation), and the statistical significance testing scores for each correlation test.

Generally, ESVs show both good omnidirectional and directional structures, as well as X-ESVs even if the directional variograms of abundance variables do not show the same main anisotropy direction as the geological formations. Therefore we modelled the experimental co-variability as isotropic and an omnidirectional linear model of coregionalization has been fitted by means of trials and errors procedure (Figure 4.10). As shown in Table 4.4, Gaussian distribution has zero mean of standardized errors and unit variance of standardized errors. It allowed us to use a cross-validation method. Thereby we double-checked the quality of the model (see for instance: Clark and Harper, 2000; Goovaerts, 1997; Isaaks and Srivastava, 1989), by comparing errors, made in estimating airborne gamma-ray measures at sample locations, with the theoretical standard Gaussian distribution.

Table 4.4: parameters of ESVs and X-ESVs, omnidirectional linear coregionalization models (parametric geology has not measure units), and cross-validation results of primary variables (expressed through the mean of standardized errors (MSE) and the variance of standardized errors (VSE)) for all groups of variables.

Group of variables	ESV and X-ESV		Linear Coregionalization Model					
	lag		structures of variability	range (m)	coregionalization matrices		cross-validation	
	#	dist. (m)					MSE	VSE
K & Geology	8	200	nugget	-	0.09613% ²	-	0.00187	0.89497
			spherical	1500	-0.3912% ²	107.9		
U & Geology	10	500	nugget	-	3.098ppm ²	-	0.00056	0.81531
			spherical	2500	-4.3ppm ²	107.9		
Th & Geology	10	500	nugget	-	9.779ppm ²	-	-0.00102	1.02729
			spherical	2800	-10.99ppm ²	107.9		
					24ppm ²	-		
					-8.56ppm ²	108.3		

Each group of variables shows the same values of spatial variability of the geology in the coregionalization matrices. This is due to the fact that the same parametric variable is still used for all models in the estimation of abundance distribution maps of radioactive elements (**Table 4.4**). It shows a well-structured spherical variability except for six negligible pairs of measured points in the first lag (**Figure 4.10**).

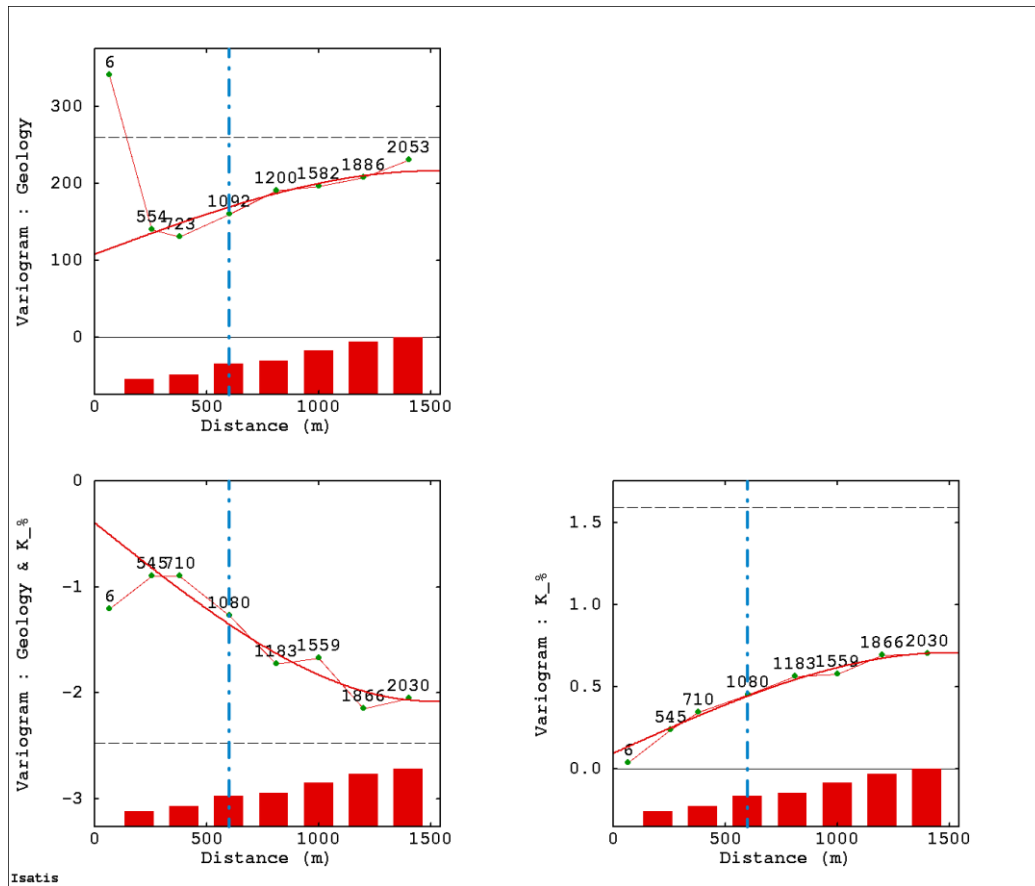


Figure 4.10: omnidirectional linear coregionalization model for K (%) abundance and parametric geology: experimental semi-variograms (diagonal of the matrix) and cross semivariograms (lower left corner); variograms and cross-variograms model with same geostatistical range; numerical and graphical (histogram) indications of the number of pairs participating in the semi-variance calculation for each lag distance (green dots with labels); distance between two consecutive airborne gamma-ray measurements along one route (vertical dashed and dotted blue line).

Finally in [Figures 4.11](#); [4.12](#) and [4.13](#) are shown the resulting estimated maps of potassium, uranium and thorium abundances obtained using CCoK interpolator with geological constrain.

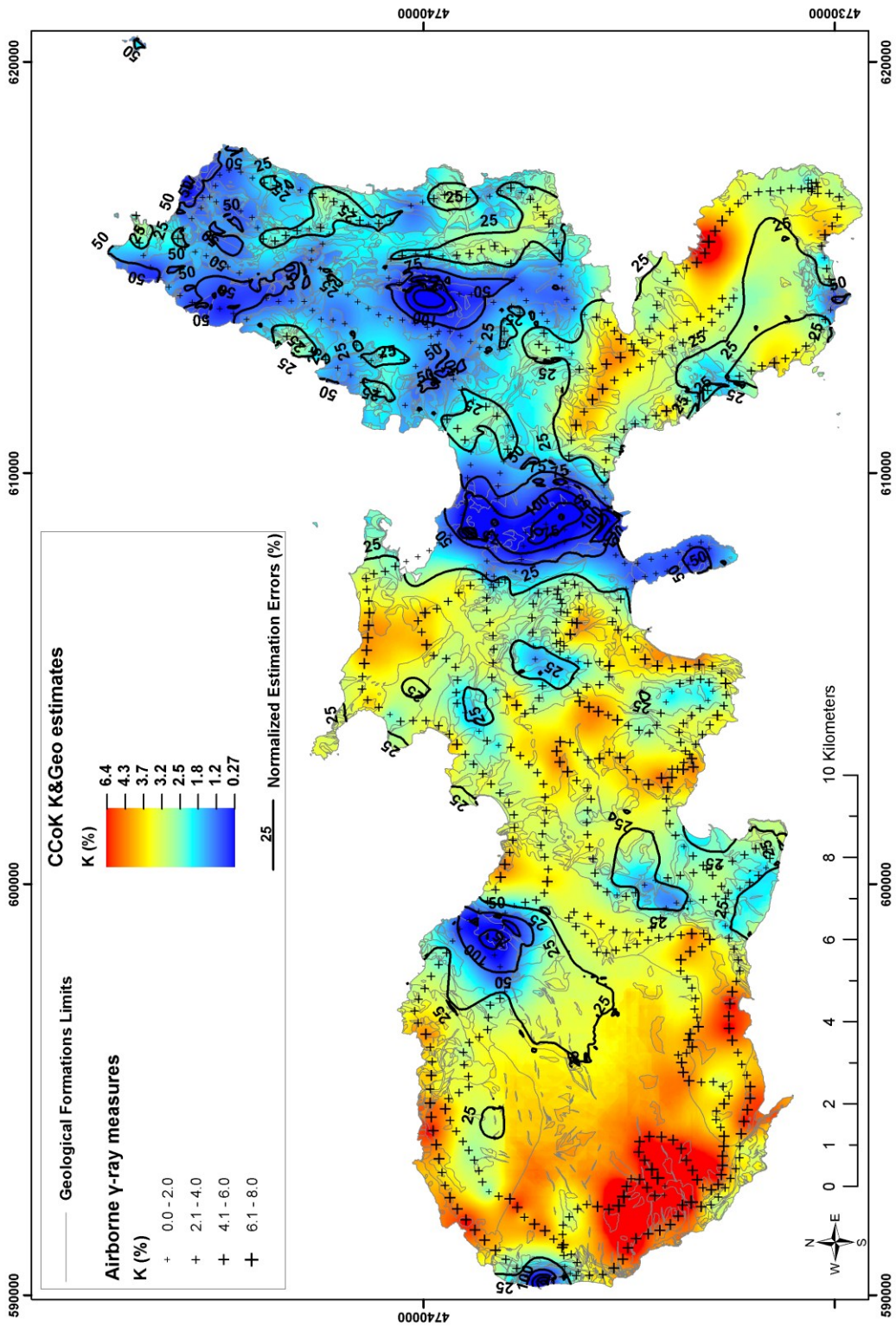


Figure 4.11: estimation map of K (%) abundance and normalized estimation errors.

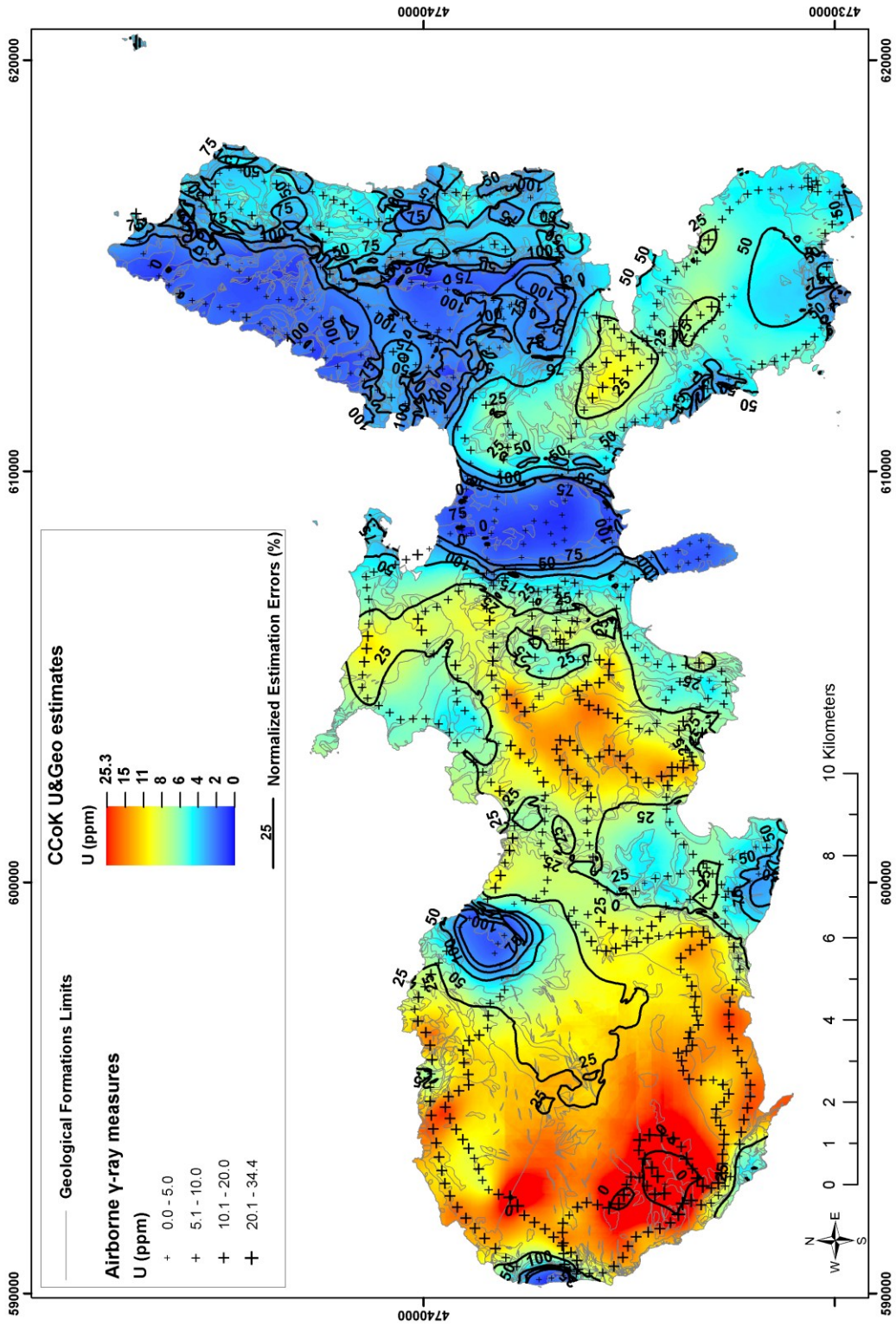


Figure 4.12: estimation map of equivalent uranium (eU) abundance in ppm and normalized estimation errors.

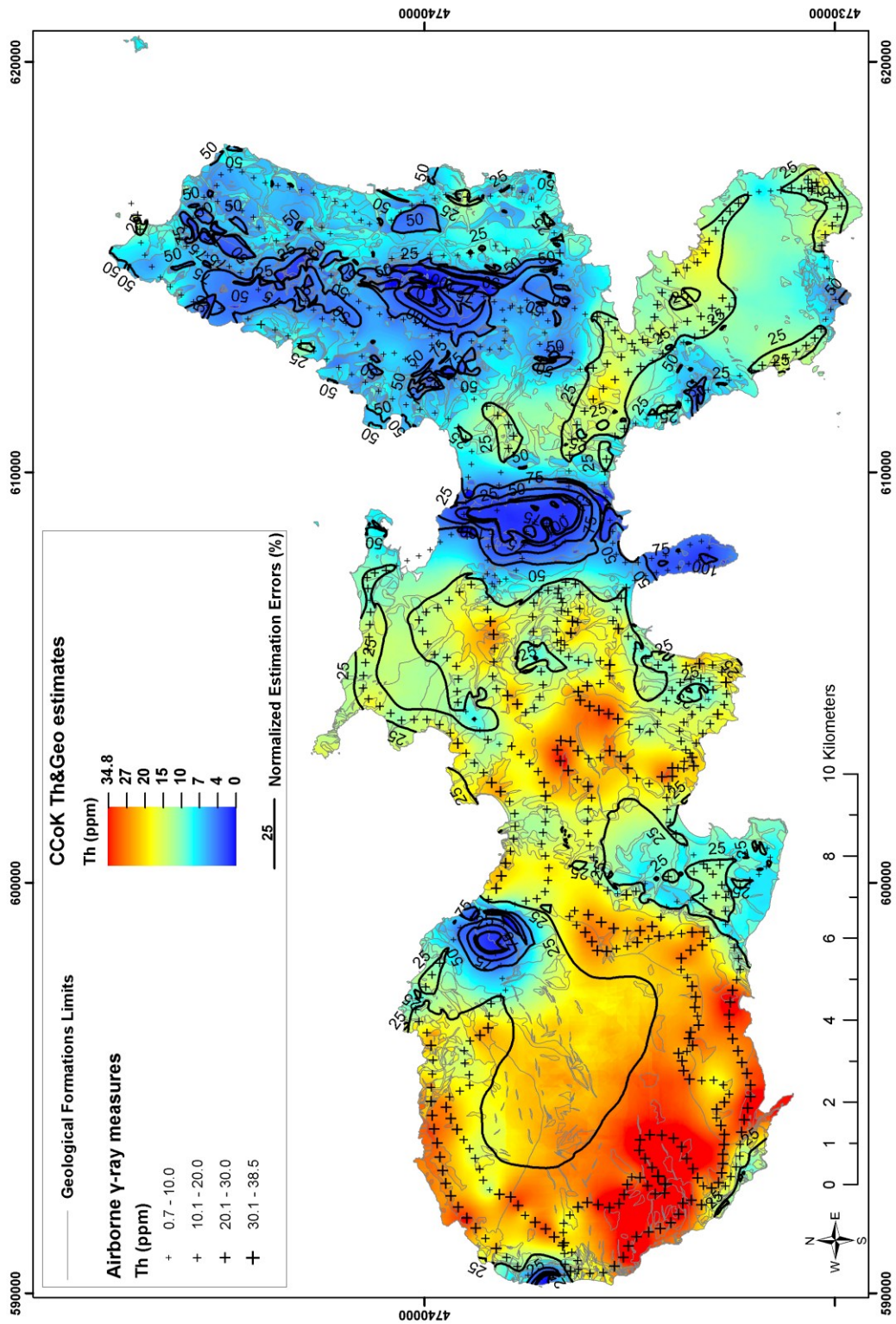


Figure 4.13: estimation map of equivalent thorium (eTh) abundance in ppm and normalized estimation errors.

Discussion of results

Elba Island (224 km²) was monitored in about 2 hours of flight using the ARGES_16.0L system collecting 803 spectra referred to an averaged spot area of the order of 0.25 km² (90% of the signal comes from an are of radius of about 300m). At the average flying height (140 ± 50 m) the most gamma radiation is originated at about 20 cm of topsoil depending on physical parameters of the soil. Performing the post-processing described in previously, we associated homogenous K, eU and eTh abundances to each spot area. Taking into account that only 25% of the total area of Elba island consist of geological polygons having an area less than 0.25 km², we observe that a large fraction of airborne gamma-ray measures refers to the contributions coming from several geological formations with different lithological compositions. Moreover, the geodatabase described in above is referred only to geological formations, therefore pedogenesis processes could alter the radioactivity content of the topsoil respect to the underlying bedrocks.

Despite of the mentioned geological and physical factors, which affect the airborne measures, the high density of radioactivity data and the highly refined geological map allowed to construct a well tested linear coregionalization model: its cross-validation procedure gives us satisfactory results (**Tab. 4.4**). On the ground of this consistent framework, the multivariate analysis produced data characterized by good assessment of spatial co-variability (**fig. 4.10**).

According to the flight plan, the autogyro crossed its own route (referring to two measurements of the same spot area) resulting in a very low variability shown in the first lags of the omnidirectional coregionalization model (as an example see the ESV of K in **fig. 4.10**).

The ESVs models built up for the AGRS measurements show regular structures having low variabilities at small distances and generally higher at the spherical parts. Indeed, the nugget effect of K abundance contributes with almost 16% to the total amount of spatial variability, denoting the evidence of autocorrelation. The same features are found for eTh and eU abundances, whose variances at small distances contribute respectively with 13% and 30% to the total spatial variability. Moreover, we notice a low spatial variability also below 600 m (corresponding to spot area radius, indicated by the blue dashed line in **fig. 5**), which corresponds to data obtained by partially overlapped spot areas. The distance of autocorrelation for K, eU and eTh are 1500 m, 2800 m and 2500 m respectively. These features reconstruct the spatial resolution of AGRS survey confirming the consistency of the model and the AGRS data.

For what concerns geology, the variability of parametric geology variogram at small distances shows a variability discontinuity at lag $h = 0$, i.e. nugget effect (Wackernagel 2003). This contributes to almost 50% of the total spatial variability. This is due to the random values assigned to the “categories” of the geological map where significant difference can be found between sample values of two adjacent geological formations.

X-ESVs constructed for isotope-geology couples generally show well defined co-variability structures. However, the variability discontinuity in the first lag is a consequence of large spatial variability of the values assigned to two contiguous geological formations, which are investigated by two overlapped spot areas with a small spatial variability of abundances (fig. 5). On the ground of the previous considerations the spatial covariance in the first lag can be neglected since it is strongly related to the random geological parameters. Therefore, we conclude that these choices ensure the consistency of the results achieved by using the CCoK multivariate interpolator.

As we emphasized in the previous section, we did not consider the experimental uncertainties of airborne gamma-ray measures in CCoK estimations for all groups of variables. The estimated maps of K, eTh, and eU abundances are shown in Figures 4.11, 4.12, and 4.13. These maps are calculated with a high spatial resolution (pixel size 10 m x 10 m) in accordance with the choice of the geological map at 1:10,000 scale. We also report the accuracy of estimations by adopting the variance, normalized respect to the estimated values of the abundances (normalized standard deviation, NSD). The percentage uncertainties of the abundances are higher where the absolute measures are smaller for K, eU, eTh respectively.

In the geostatistical approach described we faced the problem of correlating a quantitative variable (radioactivity content) to a typical categorical extensive variable (geology). As a tentative solution, we assigned a progressive number to each geological category of geodatabase first sorted in alphabetic ascending order (Geo1). The results obtained albeit satisfactory, were tested for possible bias. Therefore, we constructed two new casual arrays referred to categories of the geological map: Geo2 and Geo3 are obtained by randomly assigning series from 1 to 100 and from 1 to 100000 respectively.

The main results of this test are summarized in table 4.5: for the sake of simplicity, we only discuss the comparison of estimated maps of K abundance. However, the whole procedure has been performed for every radioisotopes combined with geological parametrical map. Frequency distributions of the three estimation maps are similar in terms of histograms (Figure 4.14a and Figure 4.15a) and main

and descriptive statistics slightly differ each other (**Table 4.5**), as well as the NSD maps (**Figure 4.14b** and **Figure 4.15b**).

Table 4.5: Descriptive statistics of estimation maps of K abundances (CCoK estimation) and the respective estimation errors (NSD), and their map differences. Column G (± 0.1): percentage of two maps' pixels that differ each other less than $\pm 0.1\%$ of K abundance. Column H ($\pm 1&2\sigma$): percentage of two maps' pixels that differ each other between 1 and 2 standard deviation from the mean of the difference map, which is close to 1% of K abundance.

A	B	C	D	E	F	G	H
Type	Map	Min (%K)	Max (%K)	Mean (%K)	St. Dev. (%K)	± 0.1 (%pixel)	$\pm 1&2\sigma$ (%pixel)
CCoK estim.	K&Geo1	0.041	6.468	2.815	1.081	-	-
	K&Geo2	0.299	6.408	2.806	1.071	-	-
	K&Geo3	0.273	6.402	2.811	1.077	-	-
Differ. CCoK	K&Geo1 - K&Geo2	-0.812	0.795	0.004	0.124	71	19
	K&Geo1 - K&Geo3	-0.908	0.833	-0.001	0.147	65	20
	K&Geo2 - K&Geo3	-0.454	0.486	-0.005	0.086	82	16
NSD	K&Geo1	5	193	21.6	17.1	-	-
	K&Geo2	6	158	25.8	16	-	-
	K&Geo3	6	185	25.5	15.7	-	-
Differ. NSD	K&Geo1 - K&Geo2	-38	131	-4.17	4.28	97.5	1.87
	K&Geo1 - K&Geo3	-77	132	-3.92	5.08	96.62	6.61
	K&Geo2 - K&Geo3	-61	44	0.25	2.67	98.62	1.15

A simple map algebra algorithm, i.e. difference between two raster maps of CCoK estimations, allowed to spatially quantify the actual dissimilarity in K abundance estimation on the basis of three different parametric geological maps. The most part of pixels of three K abundances estimated maps are alike, about 71% of pixels point out a difference of $\leq 0.1\%$ of K abundance between maps estimated with secondary variable Geo1 and Geo2, a dissimilarity that is almost 1/10 of the average standard deviation of all three estimation maps (column G in **Table 4.5**). Moreover, less than 19% of pixels lays between one and two standard deviations of distance from the average values of difference maps. We achieved almost the same scores by comparing other K abundance estimation maps (column H in **Table 4.5**). From this descends that independently from which random geological classification criterion we use, we find a strong similitude among estimation maps.

The larger differences between CCoK estimation of K abundances are to be ascribed to the pixels close to the contact line between two geological formations. This could be due to the fact that smooth changing of airborne gamma-ray measures in passing from a geological formation to the neighboring one, where there is the mutual influence of different abundances in two formations, actually affects the measured spot area.

The main features of the resulting radiometric maps of abundances for the natural radioelements overlay the prominent geological formations of Elba island. Indeed, relevant geological structures occupied by Trevisan complex (TC), described above, can be easily identified among them by comparing similar abundances of natural radioelements, other than those guaranteed by the geological constrain used in the CCoK interpolator.

The radiometric maps of K, eTh and eU abundances (**Figures 4.11, 4.12 and 4.13**, respectively) show relatively high values of abundances in the western sector of the island, corresponding to the intrusive granitic complex of Mt. Capanne (indicated as "CAPa" and "CAPb" geological formations in **Fig. 4.6**). Furthermore, we underline relatively high values of the three abundances in the Central part of the Island (in between Portoferraio and Marina di Campo): in the aplitic and porphyritic dykes and laccoliths with monzogranitic composition (indicated as "fe1" geological formation, **Fig. 4.6**). However, evidences of relatively high K abundances are shown also in the South-eastern sector, especially on Mt. Calamita promontory (**Fig. 4.11**): the latter is characterized as homogeneous geological formation (indicated as "FAFc", metamorphic geological formation in **Fig. 4.6**, composed by cornubianitic mychacistes belonging to TC I, **Fig. 4.7**). Emphasis must be given to the fact that in other sectors of Elba island characterized by the same geological formation the K abundances show relatively moderated values. This anomaly can be due to two different albeit related factors. The first one concerns the intense tectonization and following fracturation of this sector, which allowed a significative circulation of magmatic fluids related to the emplacement of granitic plutons of La Serra-Porto Azzurro. The second factor concerns the presence of a high number of aplitic intrusions (which had been undergone to an intense magmatic evolution) whose dimensions are out of the spatial resolution of 1:10,000 scale. These intrusions, due to their chemical properties, show high K abundance.

On the other hand, in geological formations belonging to TC II and TC III, described above, low values of natural radioelement abundances (**Figures 4.11, 4.12 and 4.13**) occur. These geological formations essentially crop out in the north-eastern sector, between Porto Azzurro and Cavo, in the southern part of Portoferraio where we find peridotites (profound mantel rocks) and pillow lavas (which are volcanic rocks cooled in subaqueous environments, indicated as "PRN" and "BRG", **Fig. 4.6**). Finally, low abundance values occur in the area of Punta Nera at the western edge of the Island, where lithologies belonging to the Ortano Unit crop out (TC II, **Fig. 4.7**).

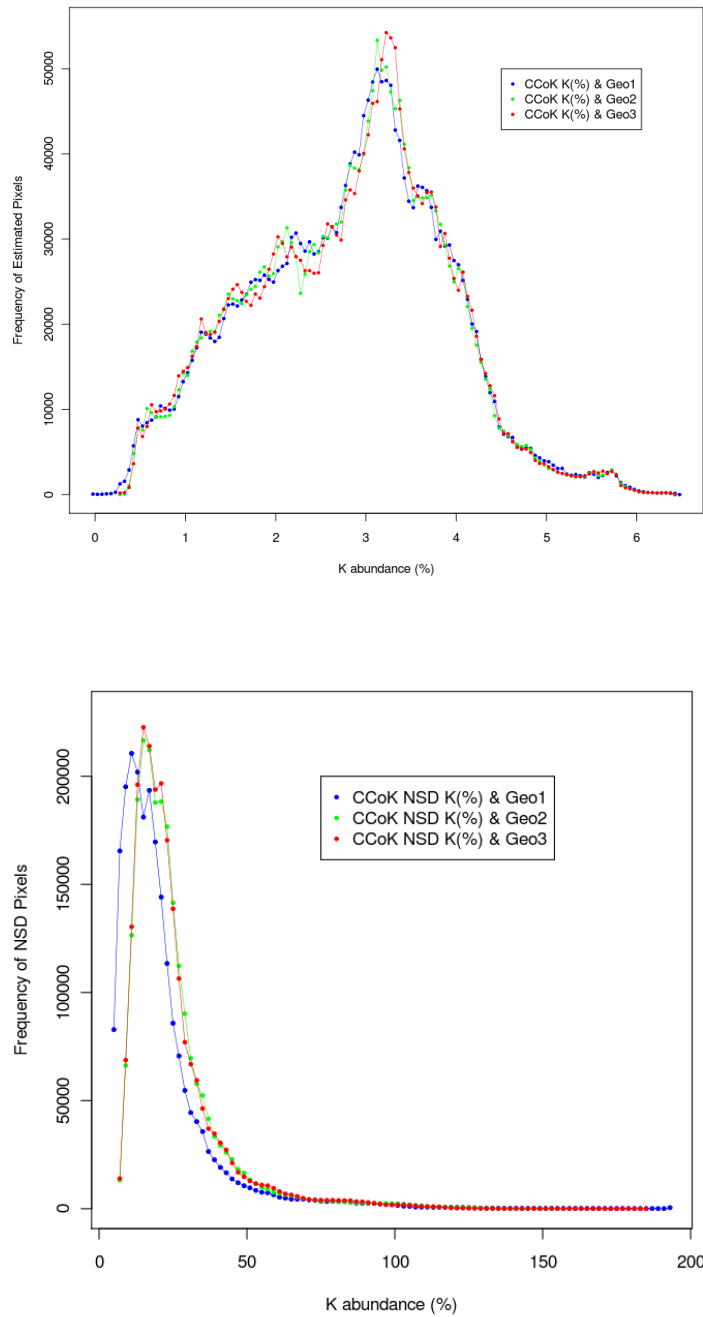


Figure 4.14: a) frequency distributions of kriged maps of K abundances estimated by CCoK through three different reclassification of geological map of Elba Island; b) frequency distributions of Normalized Standard Deviations maps (the accuracy of CCoK estimations).

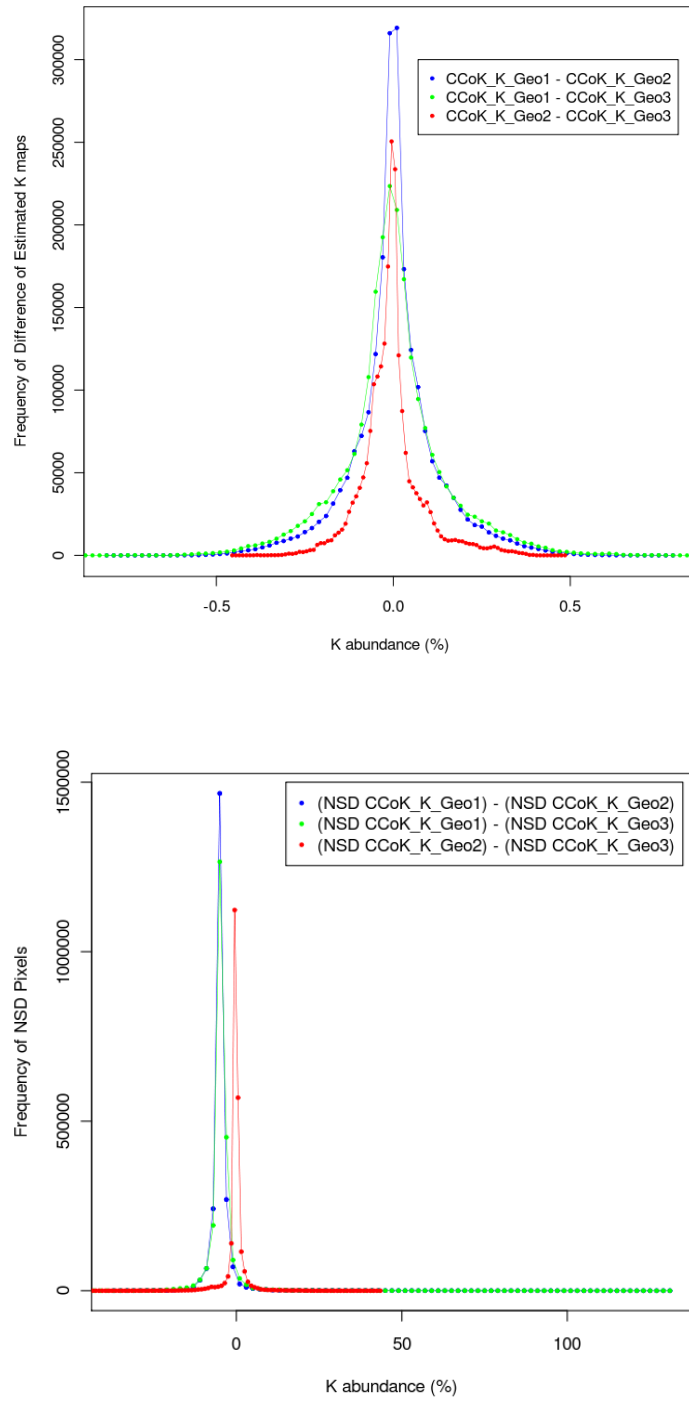


Figure 4.15: a) frequency distributions of differences between pairs of kriged maps of K abundances estimated by CCoK through three different reclassification of geological map of Elba Island; b) frequency distributions of differences between pairs of Normalized Standard Deviations maps.

Chapter 5

Conclusions

The environmental radioactivity monitoring programs start in the late 1950s of the 20th century following the global fallout from testing of nuclear weapons in the atmosphere, becoming a cause of concern regarding health effects. Furthermore, world wide exploration for fuel minerals (uranium exploration) was particularly developed in USA, Canada (Grasty 1975) and former USSR and in 1951 in Australia (Minty 2011) with respective national plans: these plans were related with the necessity of world industrialization for new energy sources led to develop national plans on electricity production from nuclear technology. Nowadays the nuclear emergency preparedness of a large number of states give rise to joint European monitoring plans (like Radioactivity Environmental Monitoring (REM) data bank and European Radiological Data Exchange Platform (EURDEP) (Szegvary et al., 2007)). In the first chapter I give a general description for the common radionuclides having a particular interest for monitoring programs, classified in three categories according to their origin as cosmogenic, primordial and man-made and present in the environment. Gamma-ray spectroscopy technique, widely used in environmental monitoring programs, is considered here as a potential technique approaching three different intervention levels; in laboratory (Chapter 2), in-situ (Chapter 3) and airborne (Chapter 4) measurements. For each of these methods, an advanced handling of gamma-ray spectrometry technique is developed by improving the performances of instruments and realizing and testing dedicated equipments able to deal with practical problems of radioactivity monitoring. Furthermore, for each gamma-ray spectrometry methods are faced also the problems of calibration, designing of monitoring plans and data analyzing and processing.

In chapter two we describe the developments reached for the laboratory gamma-ray spectrometry method using HPGe detectors, which is a widely used analysis method performed on sample for a refined estimation of radioactivity concentrations of ^{226}Ra (^{238}U), ^{228}Ac (^{232}Th) and ^{40}K . For this purpose, we developed a fully automated low-background high-resolution gamma-ray spectrometer system using two coupled HPGe detectors (MCA_Rad system), which is a well known method used to increase the detection efficiency: confronting the minimum detection activity (MDA) of the system with typical environmental measurements on relatively small sample volumes up to 180 cc, it can be deduced that measurements in less than one hour are realized with uncertainties of less than 5%. An alternative approach on shielding design and sample changer automation was realized. The new shielding design of 10 cm thick of lead and of 5 cm thick copper configuration allowed to reach a background reduction of two order of magnitude respect to laboratory radioactivity. Furthermore, a severe reduction of manpower cost is obtained by a fully automation system which permits to measure

up to 24 samples without any human attendance. This followed by a user-friendly software, developed in order to automatically analyze a high number of spectra and easily customized the output.

An empirical efficiency calibration method using multi-gamma standard point sources is discussed. The correction factors affecting the measured spectra (coincidence summing, sample shape, sample gamma-ray self-attenuation) are given with respective procedures. As a result of this procedure the absolute efficiency is estimated to have an overall uncertainty of less than 5%. A test of the applicability of the instrument as well as the method quality control using certified reference materials showed an overall relative discrepancy of less than 5% among certified central values within the reported uncertainty.

The MCA_Rad system was used in the characterization of the natural radioactivity concentration of bed-rocks in Tuscany Region, Italy. An extended sampling campaign was realized in guided by the geological structure (geological map at 1:250,000 scale) of the area in order to characterize the natural radioelement content. Up to 42 geological formational domains are well characterised for their radioactivity content with more than 800 samples measured using the MCA_Rad system. For each of this geological formational domains are reported the radioactivity concentration distributions and the corresponding external gamma radiation dose rates ([Table 2.7](#)). Finally, the potential radioactivity concentration map of the bed-rocks in Tuscany Region was realized through the radiological reclassification of the investigated geological formational domains.

In the third chapter is described the application of portable scintillation gamma-ray spectrometers with NaI(Tl) detectors for in-situ monitoring programs. We realized a portable instrument using a 10 cm x 10 cm x 10 cm NaI(Tl) detector configured in a back-pack and equipped with GPS antenna and environmental parameters control (pressure, humidity and temperature), ZaNaI_1.0L. In this context we focused on the development of calibration and spectrum analysis method. Conventionally, a series of self-constructed calibration pads prevalently enriched with one of the radioelements is used to calibrate this portable instrument. This procedure was further developed by introducing the stripping (or window analysis) method, described in International Atomic Energy Agency (IAEA) guidelines ([IAEA 2003](#), [IAEA 2010](#)) as a standard methods for natural radioelement exploration and mapping. We developed an alternative calibration procedure using instead well-characterized natural sites, which show a prevalent concentration of one of the radioelements. Furthermore, the full spectrum analysis (FSA) method was further developed by implementing for the first time the non-negative least square (NNLS) constrain in the calibration and in the spectrum analysis algorithms. This new approach permits to avoid artifacts and non physical results in the FSA analysis related with the χ^2

minimization process. The FSA-NNLS analysis method permits reduces of measurement live time (by considering the full spectrum statistics reduces the related statistical uncertainty) and allows to easily analyze more radioisotopes other than the natural ones. Indeed, as an example of the potentialities of such a method ^{137}Cs isotopes has been implemented in the analysis, which is an important radioisotope for environmental studies and monitoring.

Finally, $\text{ZaNaI}_{1.0\text{L}}$ equipment is used for extensive in-situ measurements in Ombrone Valley (Tuscany Region, Italy), which extend an area of about 3500 km^2 . Over 80 different sites are successfully characterised through in-situ measurements for potassium, uranium and thorium concentrations and the corresponding external gamma radiation dose rates. The method was validated by studying the correlation between in-situ ($\text{ZaNaI}_{1.0\text{L}}$) and laboratory (MCA_Rad) measurements. In particular the concentrations have been obtained with a 5% error on ^{40}K , 7% error on ^{232}Th , and 15% error on ^{238}U concentration. The FSA-NNLS analysis method was also applied in airborne radiometric data analysis (Chapter 4), where the need of advantage of working with reduced statistics allows to reduced equipment weight and flying costs.

In the fourth chapter is discussed the airborne gamma-ray spectrometry (AGRS) method as a widely considered an important tool for mapping environmental radioactivity both for geosciences studies and for purposes of radiological emergency response in potentially contaminated sites. Indeed, they have been used in several countries since the second half of the twentieth century, like USA and Canada, Australia, Russia, Czech Republic, and Switzerland. We self-constructed airborne gamma-ray spectrometer, $\text{AGRS}_{16.0\text{L}}$, realized as a modular system composed by four $10 \text{ cm} \times 10 \text{ cm} \times 40 \text{ cm}$ NaI(Tl) crystals equipped with a radon monitor (1L NaI(Tl) detector), GPS antenna and Altimeter (based on pressure and temperature data). We applied the new calibration procedure described in chapter three using well-characterized natural sites and implemented for the first time in radiometric data analysis FSA analysis method with NNLS constrain. This method permits to decrease the statistical uncertainty and consequently reduce the minimum acquisition time (which depend also on AGRS system and on the flight parameters), by increasing in this way the spatial resolution. Radiometric data processing is described in detail for the cosmic and aircraft background correction, atmospheric radon correction and flying height and topography correction.

The $\text{AGRS}_{16.0\text{L}}$ was used for radioelement mapping survey over Elba Island (Tuscany Region, Italy): an area of about 225 km^2 was surveyed for about two hours of flight gathering more than 800 spectra (for 10 seconds sampling). The statistical accuracies of 7%, 15% and 20% for ^{40}K , eU and eTh

abundances respectively, obtained through airborne gamma-ray spectrometry, are satisfactory and well accepted for such measurements. A particular attention is focused to the problem of spatial distribution of airborne radiometric data using spatial interpolators. It is well known that the natural radioactivity is strictly connected to the geological structure of the bedrocks and this information has been taken into account for the analysis and maps construction. A multivariate analysis approach was considered in the geostatistical interpolation of radiometric data, by putting them in relation with the geology (geological map at 1:10,000 scale) through the Collocated Cokriging (CCoK) interpolator. As a result of this study, was realized the first detailed map of potassium, uranium and thorium of Elba island at 1:10,000 scale (spatial resolution 10 m x 10 m) by combining smoothing effects of probabilistic interpolators, such as CCoK, and the abrupt characteristics of the geological map.

References

A

- Åkerblom G., 1986. Investigation and mapping of radon risk areas. Paper presented at the International Symposium on Geological Mapping in the Service of Environmental Planning Commission for the Geological Map of the World, Trondheim, Norway, 6–9 May, 1986. In: *Geology for Environmental Planning* (Ed. F.C. Wolff), Geological Survey of Norway, Special Papers, 96–106.
- Allyson J.D., 1994. Environmental gamma-ray spectrometry :simulation of absolute calibration of in-situ and airborne spectrometers for natural and anthropogenic sources. PhD thesis.
- Almeida A., Journel A., 1994. Joint simulation of multiple variables with a markov-type coregionalization model, *Mathematical Geology* 26, 565-588.
- ANSI NO.42.14 1999. American national standard for calibration and use of germanium spectrometers for the measurement of gamma-ray emission rates of radionuclides.
- ASTM C1402-04 2009. Standard guide for high-resolution gamma-ray spectrometry of soil samples.

B

- Babak O., Deutsch C.V., 2009. Improved spatial modeling by merging multiple secondary data for intrinsic collocated cokriging, *Journal of Petroleum Science and Engineering* 69, 93-99.
- Baldoncini M., 2010. Applicazione del metodo Non Negative Least Square alla Full Spectrum Analysis nel processo di calibrazione di uno spettrometro di raggi gamma portatile. graduate thesis, University of Ferrara.
- Barberi F., Dallan L., Franzini M., Giglia G., Innocenti F., Marinelli G., Raggi R., Squarci P., Taffi L., Trevisan L., 1969. Note illustrative della Carta Geologica d'Italia alla scala 1:100.000, Foglio 126 (Isola d'Elba), *Serv. Geol. d'It.*
- Bartlett D.T., 2004. Radiation protection aspects of the cosmic radiation exposure of aircraft crew. *Radiation Protection Dosimetry* 4, 349–355.
- Bartole R., Torelli L., Mattei G., Peis D., Branciolini G., 1991. Assetto stratigrafico-strutturale del tirreno settentrionale: Stato dell Oarte, *Studi Geologici Camerti*, Vol. Spec. 1, 115-126.
- Bartole R., 1995. The north tyrrhenian- northern apennines postcollisional system: Constains for a geodynamic model, *Terranova* 7, 7-24.
- Beck, H. L., DeCampo, J., Gogolak, C. 1972. In situ Ge(Li) and NaI(Tl) gamma-ray spectrometry. Report HASL-258, USAEC, New York, NY: Health and Safety Laboratory.
- Beck H.L., 1972. The physics of environmental gamma radiation fields. In: *The Natural Radiation Environment II* (Ed J.A.S. Adams, W.M. Lowder, and T.F. Gesell), US Energy Research and Development Administration (USERDA) Report CONF-720805-P2, pp. 101–134.
- Bierkens M.F.P., Burrough P., 1993. The indicator approach to categorical soil data: Theory, *Journal of Soil Science* 44, 361-368.

- Boccaletti M., Elter P., Guazzone G., 1971. Plate tectonic model for the development of the Western Alps and Northern Apennines. *Nature* 234: 108-110.
- Bolivar J.P., Garcia-Leon M., Garcia-Tenorio R., 1997. On Self-attenuation Corrections in Gamma-ray Spectrometry. *Appl. Radiat. Isot.* 48, 1125-1126.
- Boltneva L.I., Nazarov I.M., and Fridman SH.D., 1974, The cosmic radiation dose at the earth's surface: *Izvestiya (English edition)* 4, 250-255.
- Bortolotti V., Fazzuoli M., Pandeli E., Principi G., Babbini A., Corti S., 2001. Geology of central and eastern elba island, italy, *Ofioliti* 26, 97-150.
- Bossew P., 2005. A very long-term HPGe-background gamma spectrum. *Applied Radiation and Isotopes* 62, 635–644.
- Bouville A., and Lowder W.M., 1988. Human population exposure to cosmic radiation. *Radiation Protection Dosimetry* 24, 293.
- Boutsidis C., Drineas P., 2009. Random projections for the nonnegative least-squares problem. *Linear Algebra Appl* 431, 760-12.
- Buttafuoco G., Tallarico A., Falcone G., Guagliardi I., 2010. A geostatistical approach for mapping and uncertainty assessment of geogenic radon gas in soil in an area of southern italy, *Environmental Earth Sciences* 61, 491-505.

C

- Caciolli A., Baldoncini M., Bezzon G., Broggin C., Buso G., Callegari I., Colonna T., Fiorentini G., Guastaldi E., Mantovani F., Massa G., Menegazzo R., Mou L., Rossi Alvarez C., Shyti M., Xhixha G., Zhanon A., 2012. A new fsa approach for in situ gamma-ray spectroscopy, *Science of The Total Environment* 414, 639-645.
- Cesana A., Terrani M., 1989. An empirical method for peak-to-total ratio computation of a gamma-ray detector. *Nuclear Instruments and Methods in Physics Research A* 281, 172–175.
- CGT, Accordo di Programma Quadro Ricerca e Trasferimento Tecnologico per il Sistema Produttivo - C.I. Geologia e Radioattività Naturale - Sottoprogetto A: Geologia (Regional Framework Program for research and technological transfer to industry, C.I. Geology and Natural Radioactivity, Sub-Project A: Geology), Technical Report, CGT Center for GeoTechnologies, University of Siena; Tuscany Region: Italian Ministry of Education, University and Research., 2011.
- Charbonneau B. W., and Darnley A. G., 1970. Radioactive precipitation and its significance to high sensitivity gamma-ray spectrometer surveys: Geological Survey of Canada, Paper 70-1, B, 32-36.
- Chiles J.-P., Delfiner P., 1999. *Geostatistics: modeling spatial uncertainty*, Probability and Statistics Series, John Wiley and Sons, New York; Chichester.
- Chiozzi P, De Felice P, Fazio A, Pasquale V, Verdoya M. 2000. Laboratory application of NaI(Tl) γ -ray spectrometry to studies of natural radioactivity in geophysics. *Appl Radiat Isot* 53, 127–32.
- Clark I., Harper W.V., 2000. *Practical Geostatistics 2000*, volume 1, Ecosse North America Llc., Columbus, Ohio, U.S.A.
- Cleveland W. S., 1979. Robust locally weighted regression and smoothing scatter-plots, *J. Amer. Statist. Assoc.* 74, 829-836.

- Cresswell A.J., Sanderson D.C.W., White D.C., 2006. ^{137}Cs measurement uncertainties and detection limits for airborne gamma spectrometry (AGS) data analysed using a spectral windows method. *Appl Radiat Isot* 64, 247–53.
- Crossley D.J., Reid A.B., 1982. Inversion of gamma ray data for element abundances. *Geophysics* 47, 117–10.
- Currie L. A., 1986. Limits for Qualitative Detection and Quantitative Determination Application to Radiochemistry. *Analytical Chemistry* 40, 586–593.
- Cutshall N. H., Larsen I. L., Olsen C. R., 1983. Direct analysis of Pb-210 in sediment samples: self-absorption corrections. *Nuclear Instruments and Methods* 206, 309–312.

D

- Darnley A. G. and Grasty R. L., 1970. Mapping from the air by gamma-ray spectrometry: Proceedings Third International Symposium, Toronto, Can. Inst. Min. Met. Spec., 11, 485-500. Darnley, A. G., Bristow, Q. and Donhoffer, D. K., 1968. Airborne gamma-ray spectromet.
- Désésquelles P., Ha T.M.H., Korichi A., Le Blanc F., Petrache C.M., 2009. NNLC: non-negative least chi-square minimization and application to HPGe detectors. *J Phys G: Nucl Part Phys* 36, 037001–7.
- Debertin K. and Helmer R.G., 1988. Gamma- and X-ray spectrometry with semiconductor detectors. North-Holland, Amsterdam.
- Desbarats A.J., Killeen P.G., 1990. A least-squares inversion approach to stripping in gamma-ray spectral logging. *Nucl Geophys* 4(3), 343-410.
- Desbarats A.J., Logan C.E., Hinton M.J., Sharpe D.R., 2002. On the kriging of water table elevations using collateral information from a digital elevation model, *Journal of Hydrology* 255, 25-38.
- De Felice P., Angelini P., Fazio A., Biagini R., 2000. Fast procedures for coincidence-summing correction in gamma-ray spectrometry. *Applied Radiation and Isotopes* 52, 745–752.
- DeFelice P., Fazio A., Vidmar T., Korun M., 2006. Close-geometry efficiency calibration of p-type HPGe detectors with a Cs-134 point source. *Applied Radiation and Isotopes* 64, 1303–1306.
- Dini A., F. Innocenti, S. Rocchi, S. Tonarini, D. Westerman, The magmatic evolution of the late miocene laccolth-pluton-dyke granitic complex of elba island, italy, *Geological Magazine* 139 (2002) 257-279.
- Dryák P., and Kovář P., 2009. Table for true summation effect in gamma-ray spectrometry. *Journal of Radioanalytical and Nuclear Chemistry* 279, 385–394.

E

- Eckerman K.F., and Ryman J.C., 1993. External Exposure to Radionulides in Air, Water, and Soil. Federal Guidance Report No. 12. EPA 402-R-93-081.
- Engelbrecht R., Shwaiger M., 2008. State of the art of standard methods used for environmental radioactivity monitoring. *Applied Radiation and Isotopes* 66, 1604–6.

G

- Gesell T.F., 1983. Background atmospheric turn concentrations outdoors and indoors: a review. *Health Physics* 45(2), 289-302.
- Gehrke R.J., and Davidson J.R., 2005. Acquisition of quality g-ray spectra with HPGe spectrometers. *Applied Radiation and Isotopes* 62, 479–499.
- Gold S., Barkham H. W., Shlien B. and Kahn B., 1964. Measurement of naturally occurring radionuclides in air, in Adams, J. A. S. and Lowder, W. M., Eds., *The natural radiation environment*: University of Chicago Press, 369-382.
- Goovaerts P., 1997. *Geostatistics for natural resources evaluation*, Applied geostatistics series., Oxford University Press, New York ; Oxford, Geology Statistical methods.
- Goovaerts P., 1999. Using elevation to aid the geostatistical mapping of rain-fall erosivity, *Catena* 34, 227-242.
- Grasty R. L., 1975. Uranium measurement by airborne gamma-ray spectrometry *Geophysics* 40, 503-519.
- Grasty .L., Kosanke K.L., Foote R.S., 1979a, Fields of view of airborne gamma-ray detectors. *Geophysics* 44, 1447-11.
- Grasty R. L., 1979b. Gamma ray spectrometric methods in uranium exploration - theory and operational procedures, in Hood, P. J., Ed., *Geophysics and geochemistry in the search for metallic ores*: Geological Survey Canada, Economic Geology Report 31, 147-161.
- Grasty R. L., 1997. Radon emanation and soil moisture effects on airborne gamma-ray measurements: *Geophys.*, 62, 1379-1385.
- Green B.M.R., Hughes J.S., Lomas P.R., Janssens A., 1992. *Natural Radiation Atlas of Europe*. *Radiation Protection Dosimetry* 45, 491-493.
- Guastaldi E., Del Frate A.A., 2011. Risk analysis for remediation of contaminated sites: the geostatistical approach, *Environmental Earth Sciences*, 1-20.
- Guo Q., Cheng J., and Chen Y., 2005. Dose evaluation of indoor thoron progeny in some areas in China. In: *The Natural Radiation Environment VII. Proceedings of an International Symposium*, Rhodes, Greece, 20–24 May 2002 (Ed. J.P. McLaughlin, S.E. Simopoulos, and F. Steinhäusler), Elsevier, Amsterdam, 506–511.

H

- Hendriks P.H.G.M., Limburg J., de Meijer R.J., 2001. Full-spectrum analysis of natural γ -ray spectra. *J Environ Radioact* 53, 365-16.
- Hengl T., Toomanian N., Reuter H. I., Malakouti M. J., 2007. Methods to interpolate soil categorical variables from profile observations: Lessons from iran, *Geoderma* 140, 417-427.
- Hess V.F., 1912a. Über Beobachtungen der durchdringenden Strahlung bei sieben Freiballonfahrten. *Physikalische Zeitschrift* 13, 1084.
- Hess V.F., 1912b. Messungen der durchdringenden Strahlung bei zwei Freiballonfahrten (Measurements of penetrating radiation during two free balloon flights). *Wiener Sitzungsberichte Berichte* 120, 1575–1585.

Hoeksema R., R. Clapp, A. Thomas, A. Hunley, N. Farrow, K. Dearstone, Cokriging model for estimation of water table elevation, *Water Resour. Res.* 25 (1989) 429-438.

Hudson G., Wackernagel H., 1994. Mapping temperature using kriging with external drift: theory and an example from Scotland, *International Journal of Climatology* 14, 77-91.

I

International Atomic Energy Agency (IAEA), 1990. Use of gamma ray data to define the natural radiation environment, IAEA-TECDOC-566, Vienna.

International Atomic Energy Agency (IAEA), 1991. Airborne gamma-ray spectrometry surveying., Technical Report Series 323, International Atomic Energy Agency, Vienna.

International Atomic Energy Agency (IAEA), 2003. IAEA TECDOC No.1363 - Guidelines for radioelement mapping using gamma ray spectrometry data. Vienna.

International Atomic Energy Agency (IAEA), 2008. INES, The International Nuclear and Radiological Event Scale, User's Manual, Vienna.

International Atomic Energy Agency (IAEA), 2010. Radioelement mapping. Nuclear Energy Series. IAEA NES No.NF-T-13, Vienna.

International Atomic Energy Agency (IAEA), 2011. Nuclear Power Reactors In The World, Reference Data Series No. 2, Vienna.

International Commission on Radiation Units and Measurements (ICRU), 1994. Gamma-Ray Spectrometry in the Environment. ICRU Report 53.

Isaaks E. H., R. M. Srivastava, Applied Geostatistics, Oxford University Press, New York, Oxford, 1989.

ISO/IEC Guide 98:1993. Guide to the expression of uncertainty in measurement (GUM). International Organization and Standardization, Geneva, Switzerland.

J

Jolivet L., Faccenna C., Goffe' B., Mattei M., Rossetti F., Brunet C., Storti F., Funicello R., Cadet J., D'Agostino N., Parra T., 1998. Midcrustal shear zones in postorogenic extension: example from the northern tyrrhenian sea, *J. Geoph. Res.* 103, 1212-12160.

Journel A., 1986. Constrained interpolation and qualitative information, *Mathematical Geology* 18, 269-286.

K

Keller J., Pialli G., 1990. Tectonics of the island of elba: A reappraisal, *Boll. Soc. Geol. It.* 109, 413.

Knoll G.F., 1999. Radiation Detection and Measurements, Third Edition, John Wiley & Sons.

Kogan R. M., Nazarov I. M., Fridman Sh. D., 1969. Gamma spectrometry of natural environments and formations: *Israel Prog. for Sci. Trans.*, no. 5778.

Kozak K., Swakon J., Paszkowski M., Gradzinski R., Loskiewicz J., Janik M., Mazur J., Bogacz J., Horwacik T., and Olko P., 2005. Correlation between radon concentration and geological structure of the Kraków area. In: *The Natural Radiation Environment VII. Proceedings of an International Symposium, Rhodes, Greece, 20–24 May 2002* (Ed. J.P. McLaughlin, S.E. Simopoulos, and F. Steinhäusler) Elsevier, Amsterdam, 464–469.

L

Langmuir D., 1978. Uranium solution-mineral equilibria at low temperatures with applications to sedimentary ore deposits: *Geochim. Cosmochim. Acta*, 42, 547-569.

Langmuir D. and Herman J.S., 1980. The mobility of thorium in natural waters at low temperatures: *Geochim. Cosmochim. Acta*, 44, 1753-1766.

Lawson C.L., Hanson R.J., 1995. *Solving Least Square Problems*. Philadelphia.

Løvborg L., Bøtter-Jensen L., Kirkegaard P., Christiansen E.M., 1979. Monitoring of natural soil radioactivity with portable gamma-ray spectrometers. *Nuclear Instruments and Methods* 167, 341–348.

Løvborg L., Christiansen E.M., Bøtter-Jensen L., Kirkegaard P., 1981. Pad Facility for the Calibration of Gamma-Ray Measurements on Rocks. Risø-R-454.

Løvborg L., 1984. The calibration of airborne and portable gamma ray spectrometers - theory, problems and facilities: Danish Atomic Energy Commission, RISO report M-2456.

M

Mahesh H.M., Avadhani D.N., and Siddappa K., 2005. Concentration, distribution and transportation of ²²²Rn and its decay products in the environment of coastal Karnataka and Kaiga in southwest India. In: *The Natural Radiation Environment VII. Proceedings of an International Symposium, Rhodes, Greece, 20–24 May 2002* (Ed. J.P. McLaughlin, S.E. Simopoulos, and F. Steinhäusler), Elsevier, Amsterdam, 542–553.

Maučec M., Hendriks P.H.G.M., Limburg J., de Meijer R.J., 2009. Determination of correction factors for borehole natural gamma-ray measurements by Monte Carlo simulations. *Nucl Instrum Methods A* 609, 1094-11.

Megumi K. and Mamuro T., 1973. Radon and thoron exhalation from the ground: *J. Geophys. Res.*, 78, 1804-1808.

Miller K.M., Shebell P., 1993. *In situ Gamma-ray Spectrometry. A Tutorial for environmental radiation scientists*. Report EML-557. Department of Energy, New York.

Minty B.R.S., 1992. Airborne gamma-ray spectrometric background estimation using full spectrum analysis. *Geophysics* 57, 279.

Minty B.R.S., 2011. Airborne geophysical mapping of the Australian continent. *Geophysics* 76, A27; doi:10.1190/geo2011-0056.1.

Moens L., De Donder J., Xi-lei L., De Corte F., De Wespelaere A., Simonits A., Hoste J., 1981. Calculation of the absolute peak efficiency of gamma-ray detectors for different counting geometries. *Nuclear Instruments and Methods* 187, 451–472.

Monographie BIPM-5, 2004. Table of Radionuclides Vol-2. Bureau International des Poids et Measure, ISBN 92-822-2207-1.

Murith C., and Gurtner A., 1994. Mesures in situ et irradiation externe. In: BAG, Environmental radioactivity and radiation exposure in Switzerland 1993. Swiss Federal Office of Public Health, Berne.

N

National Academy of Sciences – National Research Council (NAS NRC), 1999. Evaluation of Guidelines for Exposures to Technologically Enhanced Naturally Occurring Radioactive Materials. National Academy Press, Washington, D.C., 281.

Nuccetelli C., 2008. In situ gamma spectroscopy in environmental research and monitoring. *Appl Radiat Isot* 66, 1615-4.

P

Pardo-Iguzquiza E., Dowd P.A., 2005. Multiple indicator cokriging with application to optimal sampling for environmental monitoring. *Computers and Geosciences* 31, 1-13.

Paschoa A.S., Steinhudler F., 2010. Technologically Enhanced Natural Radiation. Elsevier, ISBN: 978-0-08-044936-4.

Pei T., Qin C.-Z., Zhu A.-X., Yang L., Luo M., Li B., Zhou C., 2010. Mapping soil organic matter using the topographic wetness index: A comparative study based on different flow-direction algorithms and kriging methods, *Ecological Indicators* 10, 610-619.

R

Reimann C., 2005a. Geochemical mapping: technique or art? *Geochemistry: Exploration, Environment, Analysis* 5, 359-370.

Reimann C., Filzmoser P., Garrett R.G., 2005b. Background and threshold: critical comparison of methods of determination. *Science of the Total Environment* 346, 1– 16.

Reitz G., 1993. Radiation Environment in the Stratosphere. *Health Physics* 48, 5.

Rudnick R.L., and Gao S., 2003. Composition of the Continental Crust In: *Treatise On Geochemistry Volume 3*, ISBN: 0-08-044338-9, 1–64.

Rybach L., Bachler D., Bucher B., Schwarz G., 2002. Radiation doses of Swiss population from external sources. *Journal of Environmental Radioactivity* 62, 277–286.

S

Saito K., and Jacob P., 1995. Gamma ray fields in the air due to sources in the ground. *Radiation Protection Dosimetry*, 58, 29–45.

Saito K., Petoussi-Hens N., and Zankl M., 1998. Calculation of the effective dose and its variation from environmental gamma ray sources. *Health Physics*, 74, 698–706.

Sanderson D.C.W., Baxter M.S., Scott E.M., 1989. COGER, Lancaster Conference.

- Sanderson D., A. Cresswell, F. Hardeman, A. Debauche, An airborne gamma-ray spectrometry survey of nuclear sites in Belgium, *J. Env. Radioat.* 72 (2004) 213-12.
- Scandone P. 1979. Origin of the Tyrrhenian sea and Calabrian arc. *Boll. Soc. Geol. It.*, 98, 27-34.
- Schima F.J., and Hoppes D. D., 1983. Tables For Cascade-Summing Corrections In Gamma-Ray Spectrometry. *Int. J. Appl. Radiat. Isot.* 34:8, 1109-1114.
- Scheib C., D. Beamish, 2011. High spatial resolution observations of ^{137}Cs in northern Britain and Ireland from airborne geophysical survey, *J. Env. Radioat.* 101, 670-11.
- Schwarz G., E. Klingele, L. Rybach, How to handle rugged topography in airborne gamma-ray spectrometry surveys, *First Break* 10 (1992) 11-17.
- Semkow T.M., Mehmood G., Parekh P.P., Virgil M., 1990. Coincidence Summing In Gamma-Ray Spectroscopy. *Nuclear Instruments and Methods in Physics Research A290*, 437-444.
- Smith H.D., Robbins C.A., Arnold D.V., Gadokan L.L., Cealon J.G., 1983. A multi-function compensated spectral natural gamma ray logging system. *Soc Petrol Eng SPE* 12050.
- Stampfli, G.M., Marcoux, J. and Baud, A. 1991. Tethyan margins in space and time. In: J.E.T. Channell, E.L. Winterer and L.F. Jansa (Eds.), *Paleogeography and paleoceanography of Tethys. Palaeogeography, Palaeoclimatology, Palaeoecology. Palaeogeography, Palaeoclimatology, Palaeoecology* 87, 373-410.
- Stampfli, G.M., Mosar, J., Favre, P., Pillecuit, A. and Vannay, J.C. 2001. Permo-Mesozoic evolution of the western Tethyan realm: the Neotethys/East- Mediterranean connection. In: P.A. Ziegler, W. Cavazza, A.H.F. Robertson and S. Crasquin Soleau (Eds.), *PeriTethys memoir 6: Peritethyan rift/wrench basins and passive margins*, IGCP 369. *Mém. Museum Nat. Hist. Nat Paris* 186, 51-108.
- Szegvary T., Conen F., U. Stöhlker, G. Dubois, P. Bossew, G. de Vries, 2007. Mapping terrestrial α -dose rate in Europe based on routine monitoring data. *Radiation Measurements* 42, 1561 – 1572.

T

- Tanelli G., Benvenuti M., Costagliola P., Dini A., Lattanzi P., Manieri C., 2001. The iron mineral deposits of elba island: State of the art, *Ofioliti* 26, 239-249.
- Tanner A.B., 1964. Radon migration in the ground: a review, in Adams J.A.S. and Lowder W.M., Ed. *The natural radiation environment: University of Chicago Press*, 161-190.
- Tanner A.B., 1980. Radon migration in the ground: a supplementary review. In: Gesell T.F., Lowder W.M. (ed.), *Proceedings of The Natural Radiation Environment III. CONF-780422*. Springfield, VA: National Technical Information Service, 5-56.
- Tanner A.B., 1992. *Bibliography of Radon in the Outdoor Environment and Selected References on Gas Mobility in the Ground*. Geological Survey Open-File 92-351. Denver, CO: US Geological Survey.
- Travassos J. M. and Pires A. C. B., 1994. The screening effect of a tropical forest on airborne gamma- ray spectrometry: *Nucl. Geophys.*, 8, 461-471.

Tomarchio E., and Rizzo S., 2011. Coincidence-summing correction equations in gamma-ray spectrometry with p-type HPGe detectors. *Radiation Physics and Chemistry* 80, 318–323.

Trevisan L., 1950. L'elba orientale e la sua tettonica di scivolamento per gravita', *Mem. Ist. Geol. Univ. Padova* 16, 5-35.

Trevisan L., 1951. La 55a riunione estiva della societa' geologica italiana. isola d'elba, 18-23 settembre 1951, *Boll. Serv. Geol. It.* 70, 435-438.

Tyler A.N., 2007. Situ and airborne gamma-ray spectrometry. Analysis of Environmental Radionuclides. In: Povinec PP, editor. *Radioactivity in the Environment* 11, 532.

U

United Nations Scientific Committee on the Effects of Atomic Radiation (UNSCEAR), 1977. Report to the General Assembly, with Annexes. Sources and Effects of Ionizing Radiation, United Nation, New York, 725.

United Nations Scientific Committee on the Effects of Atomic Radiation (UNSCEAR), 1988. The United Nation Scientific Committee on the Effects of Atomic Radiation Sources to the General Assembly with Annexes, Effects and Risks of Ionizing Radiation. United Nations publication, New York.

United Nations Scientific Committee on the Effects of Atomic Radiation (UNSCEAR), 1993. Report. Sources and effects of ionizing radiation. United Nations, New York

United Nations Scientific Committee on the Effects of Atomic Radiation (UNSCEAR), 2000. United Nations Scientific Committee on the Effects of Atomic Radiation Report to the General Assembly, with Annexes. Sources and Effects of Ionizing Radiation, Vol. I: Sources, United Nation, New York, 654.

United Nations Scientific Committee on the Effects of Atomic Radiation (UNSCEAR), 2008. Sources and Effects of Ionizing Radiation, Report to the General Assembly, with scientific annexes. United Nations, United Nations Office at Vienna, ISBN 13: 9789211422740 (10.IX.3).

UNI 10797:1999. Natural radionuclides in building materials. High resolution gamma-ray spectrometry.

V

Verdoya M., Chiozzi P., De Felice P., Pasquale V., Bochiolo M., Genovesi I., 2009. Natural gamma ray spectrometry as a tool for radiation dose and radon hazard modelling. *Appl Radiat Isot* 67, 964–5.

W

Wackernagel H., 2003. *Multivariate Geostatistics: An Introduction With Applications*, Springer-Verlag, Berlin, Germany, 3rd E.d.

Wilkening M., 1990. Radon in the environment. In: *Studies in Environmental Science*. Elsevier, Amsterdam, Vol. 40, 137.

X

Xu W., Tran T., Srivastava R., Journel A., 1992. Integrating seismic data in reservoir modeling: The collocated cokriging alternative, in: SPE Annual Technical Conference and Exhibition, Society of Petroleum Engineers Inc., Washington, D.C.

Z

Zhiyanski M., Bech J., Sokolovska M., Lucot E., Bech J., Badot P.M., 2008. Cs-137 distribution in forest floor and surface soil layers from two mountainous regions in Bulgaria. *J Geochem Explor* 96, 256-11.